



universität
wien

DISSERTATION

Titel der Dissertation

Diagrammatic techniques for extended systems:
MP2 and CCSD

angestrebter akademischer Grad

Doktor der Naturwissenschaften (Dr. rer. nat.)

Verfasser:	Mag. rer. nat. Andreas Grüneis
Matrikel-Nummer:	0255939
Dissertationsgebiet:	Physik
Betreuer:	Univ.-Prof. Dipl.-Ing. Dr. Georg Kresse

Wien, am 18. Jänner 2011

Acknowledgements

I thank Georg Kresse and Martijn Marsman whose supervision has been invaluable during the years of my diploma and doctoral thesis. Next come my colleagues Judith, Joachim, Roman, Laurids, Ronald, and Florian, whose insights and discussions have been very helpful. Finally, I would like to give my most heart-felt thanks to my parents who have always supported me during the years of my education.

Abstract

This thesis is devoted to the implementation and assessment of three wave function based methods for solid state systems under periodic boundary conditions: (i) Second-order Møller-Plesset perturbation theory (MP2), (ii) Random phase approximation plus second-order screened exchange (RPA+SOSEX), and (iii) Coupled-cluster singles and doubles (CCSD).

The first part briefly reviews the employed theoretical and computational methods. The implemented expressions of the Hartree-Fock, MP2, RPA+SOSEX and CCSD theories are derived. Natural orbitals are introduced and approximated at the level of MP2. Moreover, we explain the evaluation of the required quantities in the framework of the projector-augmented wave (PAW) method as implemented in the Vienna *ab-initio* simulation package (VASP).

The second part summarizes the results that have been obtained at the different levels of theory. Structural properties, atomization energies and quasi-particle band gaps have been calculated using HF and MP2 for archetypical semiconductors and insulators. It is shown that MP2 tends to overcorrelate strongly screening materials and undercorrelate weakly screening materials. This leads to an over- and underestimation of lattice constants for weakly- and strongly screening materials, respectively. The RPA+SOSEX method was employed for the evaluation of total correlation energies of atoms, atomization energies of small molecules, as well as lattice constants and atomization energies of a series of semiconductors and insulators. We show that the introduction of second-order screened exchange lifts some deficiencies of the RPA, such as the underbinding of molecules and solids, and the overestimation of the total correlation energies. Finally, using CCSD and MP2 natural orbitals our CCSD implementation was tested for the LiH molecule as well as solid. Our results agree very well with results that have been obtained using quantum chemical codes.

Zusammenfassung

Diese Doktorarbeit befasst sich mit der Implementierung und Evaluierung von drei wellenfunktionsbasierten Methoden für Festkörper unter periodischen Randbedingungen: (i) Zweite Ordnung Møller-Plesset Störungstheorie (MP2), (ii) *Random phase approximation plus second-order screened exchange* (RPA+SOSEX), und (iii) *Coupled-cluster singles and doubles* (CCSD).

Der erste Teil erklärt die verwendeten theoretischen sowie computerorientierten Methoden. Die implementierten Ausdrücke der Hartree-Fock, MP2, RPA+SOSEX und CCSD Theorien werden teilweise abgeleitet. *Natural orbitals* werden eingeführt und auf der Ebene von MP2 approximiert. Ausserdem wird die Berechnung der benötigten Ausdrücke im Rahmen der *projector-augmented wave* (PAW) Methode, welche im *Vienna ab-initio simulation package* (VASP) implementiert ist, erörtert.

Der zweite Teil beinhaltet die numerischen Ergebnisse der verschiedenen Methoden und deren Interpretation. Gitterkonstanten, Bulkmoduli, Atomisierungsenergien und Quasiteilchen Bandlücken wurden mit Hilfe von HF und MP2 für eine Serie von Halbleitern und Isolatoren berechnet. Wir zeigen dass MP2 stark abschirmende Materialien überkorreliert und schwach abschirmende Materialien unterkorreliert. Dies führt zu einer Über- bzw. Unterschätzung von Gitterkonstanten für schwach bzw. stark abschirmende Materialien. RPA+SOSEX wurde verwendet um totale Korrelationsenergien von Atomen, Atomisierungsenergien von kleinen Molekülen, sowie Gitterkonstanten und Atomisierungsenergien von Halbleitern und Isolatoren zu berechnen. Es wird gezeigt dass die Berücksichtigung von SOSEX mehrere Probleme der RPA löst. Insbesondere korrigiert SOSEX die Tendenz der RPA zur Unterschätzung von Bindungsenergien und Überschätzung von totalen Korrelationsenergien. Schlussendlich wird die CCSD Implementierung mit Hilfe von *MP2 natural orbitals* für das LiH Molekül und den LiH Festkörper getestet. Die CCSD Ergebnisse stimmen gut mit quantenchemischen Berechnungen überein.

Contents

1	Introduction	1
I	Theory	3
2	The many-particle Schrödinger equation	5
2.1	Born-Oppenheimer approximation	5
2.2	The electronic Schrödinger equation	6
3	Density functional theory	7
3.1	Theorems by Hohenberg and Kohn	7
3.2	The LDA and GGA functionals	9
4	Hartree-Fock theory	11
5	Correlation in wave function based methods	15
5.1	Second-order Møller-Plesset perturbation theory	16
5.2	Coupled-Cluster singles and doubles theory	21
5.2.1	Unrestricted CCSD amplitude equations	24
5.2.2	Restricted CCSD amplitude equations	26
5.3	Notes on CCSD and MP2	29
5.3.1	MP2 and CCSD energies are not variational	30
5.4	The correlation energy in the random phase approximation	31
5.4.1	The adiabatic-connection fluctuation dissipation theorem	31
5.4.2	ACFDT-RPA from time-dependent density functional theory	35
5.4.3	The RPA in coupled-cluster theory	38

5.5	Beyond RPA: Second-order screened exchange	40
5.6	The direct MP2 correlation energy	43
5.7	Solving the amplitude equations	45
6	Natural orbitals	47
7	Quasiparticles in the MP2 and <i>GW</i> approximation	51
8	The PAW Method	57
8.1	The charge density	58
8.2	The total energy in the PAW method	59
8.3	Electron repulsion integrals in the PAW method	60
II	Results	65
9	Second-order Møller-Plesset perturbation theory	67
9.1	Basis set convergence and the LiH test	67
9.1.1	The Li atom and LiH molecule	68
9.1.2	Bulk LiH	71
9.1.3	Conclusions and Summary	79
9.2	Structural and energetic properties	81
9.2.1	Computational Details	81
9.2.2	Structural properties	84
9.2.3	Atomization energies	93
9.2.4	Band gaps	93
9.2.5	Metallic sodium	96
9.2.6	Conclusions and Summary	97
10	Second-order screened exchange	101
10.1	Computational details	102
10.2	Closed-shell atoms	103
10.3	Solids and molecules	105
10.4	The G2-1 test set	108
10.5	Conclusions and Summary	109

11 Natural orbitals and CCSD	111
11.1 Computational details	112
11.2 Li atom and LiH bulk using natural orbitals	113
11.3 The H ₂ and LiH test using CCSD and natural orbitals	116
11.4 Conclusions and Summary	119
12 Conclusions and Summary	121
A Slater-Condon rules	123
B Direct contributions to the MP2 QP energy	125
C Implementation of MP2 in VASP	129
D Implementation of RPA+SOSEX in VASP	131
Curriculum vitae	141
Publications List	143

Chapter 1

Introduction

Computational materials science and quantum chemistry aim at a realistic description of matter at the level of quantum mechanics. Since the solution of the full Schrödinger equation is impossible for anything but the smallest systems, approximate methods are required that ideally achieve two goals: (*i*) high accuracy, or at least a well controlled error, and (*ii*) low computational demands. Unfortunately, the scaling of the computational effort with respect to the system size is almost always less favourable for more accurate methods. However, with the increase in available computer power during the last decades, highly accurate methods become tractable and hence attract increased attention. In the field of computational quantum chemistry a systematic hierarchy of highly accurate methods for the description of the ground state energy of a many-electron system is well established. This hierarchy starts from the one-electron Hartree-Fock (HF) approximation that neglects electron correlation and ends with the *exact* non-relativistic full configuration interaction (full CI) method. In between HF and full CI, two distinct series of approximations exist: (*i*) The Møller-Plesset perturbation theory attempts to construct a converging series ($\{\text{MP1, MP2, .., MP}_\infty\}$) of approximations to the exact full CI limit. Although the series is expected to converge for simple semiconductors and insulators, metallic systems will always yield a diverging correlation energy at any order n . (*ii*) Coupled-cluster theory constructs a series of approximations ($\{\text{CCS, CCSD, .., CCSDT..}N\}$) that will at N -th order always recover the full CI limit, where N is the number of electrons. The complexity along these series of approximations, however, increases significantly and more accurate methods tend to scale quite unfavorably with respect to increasing system

size. As such, these correlated wave function methods (MP2, CCSD) have not yet been applied to extended systems. The present work is devoted to the implementation and evaluation of

- second-order Møller-Plesset perturbation theory (MP2)
- coupled-cluster singles and doubles (CCSD) theory, as well as
- an approximation to CCSD termed RPA+SOSEX

for solid state systems. The corresponding methods were coded and implemented in the Vienna ab-initio simulation package (VASP). The present thesis is organized as follows: In the first part, a brief review of the employed theoretical and computational methods is given. The second part presents results obtained using MP2, RPA+SOSEX and CCSD for periodic systems as well as molecules.

Part I
Theory

Chapter 2

The many-particle Schrödinger equation

The basic problem in theoretical condensed matter physics and quantum chemistry is to solve the many-particle Schrödinger equation, which can be written as

$$H\Psi(\mathbf{R}_1, \dots, \mathbf{R}_M, \mathbf{r}_1, \dots, \mathbf{r}_N) = i\hbar \frac{\partial}{\partial t} \Psi(\mathbf{R}_1, \dots, \mathbf{R}_M, \mathbf{r}_1, \dots, \mathbf{r}_N) \quad (2.1)$$

Here \mathbf{R}_i and \mathbf{r}_j denote the positions of the M nuclei and N electrons, respectively. Any direct analytical or numerical approach to solve this equation for anything but the smallest systems fails. Nevertheless it is possible to construct approximations to Eq. (2.1), that are applicable to a large number of problems in solid state physics and quantum chemistry.

2.1 Born-Oppenheimer approximation

Since the mass of the nuclei is much larger than the mass of the electron ($m_{\text{nucleus}} \gg m_{\text{electron}}$) one can assume that the electrons are always in the electronic ground state and adiabatic equilibrium with respect to the atomic positions. This allows to decouple the electronic and nuclear part of the wave function and yields

$$\Psi(\mathbf{R}_1, \dots, \mathbf{R}_M, \mathbf{r}_1, \dots, \mathbf{r}_N) = \Psi(\mathbf{r}_1, \dots, \mathbf{r}_N | \mathbf{R}_1, \dots, \mathbf{R}_M) \Phi(\mathbf{R}_1, \dots, \mathbf{R}_M) \quad (2.2)$$

where $\Psi(\mathbf{r}_1, \dots, \mathbf{r}_N | \mathbf{R}_1, \dots, \mathbf{R}_M)$ and $\Phi(\mathbf{R}_1, \dots, \mathbf{R}_M)$ are the electronic and nuclear wave functions, respectively. $\Psi(\mathbf{r}_1, \dots, \mathbf{r}_N | \mathbf{R}_1, \dots, \mathbf{R}_M)$ depends only parametrically

cally on \mathbf{R}_i . Furthermore the ions can be described as classical particles due to their large mass. Hence the total energy of a system reads

$$E^{\text{tot}}(\mathbf{R}_1, \dots, \mathbf{R}_M, \dot{\mathbf{R}}_1, \dots, \dot{\mathbf{R}}_M) = T(\dot{\mathbf{R}}_1, \dots, \dot{\mathbf{R}}_M) + E^{\text{nuc-nuc}}(\mathbf{R}_1, \dots, \mathbf{R}_M) + \langle \Psi(\mathbf{r}_1, \dots, \mathbf{r}_N | \mathbf{R}_1, \dots, \mathbf{R}_M) | H^{\text{el}} | \Psi(\mathbf{r}_1, \dots, \mathbf{r}_N | \mathbf{R}_1, \dots, \mathbf{R}_M) \rangle. \quad (2.3)$$

The first two terms denote the nuclear kinetic energy and the nucleus-nucleus Coulomb interaction whereas the last term is the electronic Schrödinger equation.

2.2 The electronic Schrödinger equation

Solving the electronic Schrödinger equation

$$H^{\text{el}} | \Psi(\mathbf{r}_1, \dots, \mathbf{r}_N | \mathbf{R}_1, \dots, \mathbf{R}_M) \rangle = E | \Psi(\mathbf{r}_1, \dots, \mathbf{r}_N | \mathbf{R}_1, \dots, \mathbf{R}_M) \rangle, \quad (2.4)$$

constitutes the main problem in the field of solid state physics and quantum chemistry. The electronic Hamiltonian, H^{el} , is given by

$$H^{\text{el}} = - \sum_{i=1}^N \frac{\hbar^2}{2m_e} \Delta_{\mathbf{r}_i} - \sum_{i=1}^N V_N(\mathbf{r}_i) + \sum_{i=1}^N \sum_{j>i}^N \frac{e^2}{|\mathbf{r}_i - \mathbf{r}_j|}, \quad (2.5)$$

where the first and second term are *one-electron operators* and correspond to the kinetic energy operator and the attractive nuclear potential, respectively. The attractive nuclear potential is defined as

$$V_N(\mathbf{r}) = e^2 \sum_{a=1}^M \frac{Z_a}{|\mathbf{R}_a - \mathbf{r}|}, \quad (2.6)$$

where Z_a is the atomic number of the a -th nucleus at position \mathbf{R}_a . The Born-Oppenheimer approximation allowed for reducing the dependence of Ψ on \mathbf{R}_a to this parametric form. The last term in Eq. (2.5) is a *two-electron operator* and accounts for the electron-electron Coulomb interaction. Note that the many-electron wave function, $\Psi(\mathbf{r}_1, \dots, \mathbf{r}_N)$, is a function of $3N$ coordinates, where N is the number of electrons. Any approach to solve Eq. (2.4) directly is limited to a few electrons because of the high dimensionality of $\Psi(\mathbf{r}_1, \dots, \mathbf{r}_N)$. Therefore all methods that are applicable to a reasonable system size either do not require the explicit knowledge of Ψ or find a reduced rank representation of the many-electron wave function Ψ .

Chapter 3

Density functional theory

Density functional theory is a method that solves the electronic Schrödinger equation [Eq. (2.4)] exactly without requiring the explicit knowledge of the complete many-electron wave function Ψ .

3.1 Theorems by Hohenberg and Kohn

In 1964 Hohenberg and Kohn formulated two theorems that form the basis of density functional theory (DFT) [1].

1. Every observable of a stationary quantum mechanical system is uniquely determined *only by its ground state density* n . Therefore the energy of a system can be written as a functional E of the density.

$$E[n] = \langle \Psi | H | \Psi \rangle$$

2. The exact ground state density is the one that minimizes $E[n]$:

$$E[n] = \min_{\Psi|n} \langle \Psi | H | \Psi \rangle,$$

where $\min_{\Psi|n}$ denotes a minimization with respect to the wave function Ψ that is consistent with the density n .

Kohn and Sham suggested to split up the functional $E[n]$ into several contributions, which can be written in the following form [2]:

$$E[n] = T_n[n] + E_{nn}[n] + E_{ne}[n] + E_{ee}[n] + E_{xc}[n]. \quad (3.1)$$

Here $E_{nn}[n]$, $E_{ne}[n]$ and $E_{ee}[n]$ denote the nucleus-nucleus, the nucleus-electron and the electron-electron Coulomb energies. $T_n[n]$ is the kinetic energy of non-interacting electrons. These terms can be calculated explicitly. The last term in Eq. (3.1), $E_{xc}[n]$, is the exchange-correlation energy. It is implicitly defined through Eq. (3.1), as the difference between the many-body ground state energy, $E[n]$, and the first four terms on the right-hand side. An explicit expression for $E_{xc}[n]$ is not known.

Due to its complexity the correlation energy term and, sometimes, the exchange energy term, are approximated. This is commonly done by introducing functionals $E_{xc}[n]$ that are exact for the homogeneous electron gas. Such functionals have been proposed in various forms like LDA (local density approximation) or GGA (generalized gradient approximation) and fulfill certain sumrules for the exchange and correlation hole, as well as asymptotically known limits.

In Kohn-Sham density functional theory, the density of an N -electron system is calculated as the sum over the densities of N one-electron orbitals,

$$n(\mathbf{r}) = \sum_{i=1}^N \psi_i^*(\mathbf{r})\psi_i(\mathbf{r}) \quad (3.2)$$

The one-electron orbitals, $\psi_i(\mathbf{r})$, are the solutions of the Kohn-Sham equations,

$$\left(-\frac{\hbar^2}{2m}\Delta_{\mathbf{r}} - V_N(\mathbf{r}) + V_H(\mathbf{r}) + v_{xc}(\mathbf{r}) \right) \psi_i(\mathbf{r}) = \epsilon_i \psi_i(\mathbf{r}), \quad (3.3)$$

where V_N is the external attractive potential of the nuclei as defined in Eq. (2.6) and the Hartree potential, V_H , reads

$$V_H(\mathbf{r}) = e^2 \int d^3\mathbf{r}' \frac{n(\mathbf{r}')}{|\mathbf{r} - \mathbf{r}'|}. \quad (3.4)$$

The exchange and correlation potential, v_{xc} , is given by

$$v_{xc}(\mathbf{r}) = \frac{\delta E_{xc}[n(\mathbf{r})]}{\delta n(\mathbf{r})}. \quad (3.5)$$

The one-electron wave functions in Eq. (3.3) are subject to the orthonormality constraint

$$\int d^3\mathbf{r}' \psi_i^*(\mathbf{r}') \psi_j(\mathbf{r}') = \delta_{ij}. \quad (3.6)$$

3.2 The LDA and GGA functionals

The simplest form to approximate E_{xc} is the local density approximation (LDA),

$$E_{xc}^{LDA}[n(\mathbf{r})] = \int \epsilon_{xc}(n(\mathbf{r})) n(\mathbf{r}) d^3\mathbf{r}, \quad (3.7)$$

where $\epsilon_{xc}(n(\mathbf{r}))$ is the exchange-correlation energy density of the homogeneous electron gas. $\epsilon_{xc}(n(\mathbf{r}))$ is known from Monte Carlo simulations [3]. Strictly speaking it is not correct to assume that $\epsilon_{xc}(n(\mathbf{r}))$ depends only on the local density in solids. Nevertheless the results are often in good agreement with experiment, especially for metals. The LDA fails if the gradient of the density becomes large.

A better approximation to E_{xc} can be obtained by the additional inclusion of a dependence on the local gradient of the density [4],

$$E_{xc}^{GGA}[n(\mathbf{r})] = \int f_{xc}(n(\mathbf{r}), |\nabla n(\mathbf{r})|) n(\mathbf{r}) d^3\mathbf{r}. \quad (3.8)$$

This is commonly known as the generalized gradient approximation (GGA). Like $\epsilon_{xc}(n(\mathbf{r}))$, $f_{xc}(n(\mathbf{r}), |\nabla n(\mathbf{r})|)$ has to be parametrized by an analytical function to perform practical calculations. How the construction of such functionals is done in detail is beyond the scope of this chapter. Presently the most common and most universal (or best balanced) functional is the one of Perdew, Burke and Ernzerhof in Ref. [5]. This functional will be referred to as PBE-functional in the following chapters.

Chapter 4

Hartree-Fock theory

In contrast to DFT, which in principle allows to determine the exact ground state density but not the many-electron wave function, Hartree-Fock (HF) theory [6, 7] *tries to approximate the “true” many-electron wave function*. The HF ansatz for the N -electron wave function reads

$$\Psi^{\text{HF}}(\mathbf{r}_1, \dots, \mathbf{r}_N) = \frac{1}{\sqrt{N!}} \left| \begin{pmatrix} \psi_1(\mathbf{r}_1) & \dots & \psi_N(\mathbf{r}_1) \\ \dots & \dots & \dots \\ \psi_1(\mathbf{r}_N) & \dots & \psi_N(\mathbf{r}_N) \end{pmatrix} \right|. \quad (4.1)$$

$\Psi^{\text{HF}}(\mathbf{r}_1, \dots, \mathbf{r}_N)$ corresponds to a Slater determinant that is constructed from a set of orthonormal one-electron orbitals (spin-orbitals) $\psi_i(\mathbf{r})$ [8]. By construction, Ψ^{HF} is antisymmetric under exchange of two coordinates or orbitals, as required for a fermionic wave function. The HF approximation neglects electronic “correlation” completely, which is in fact defined as the difference between the HF energy and the true many-body ground state energy. We will come back to this point later.

Inserting Ψ^{HF} as ansatz into Eq. (2.4) yields the electronic energy expression in the Hartree-Fock approximation

$$E^{\text{HF}} = \langle \Psi^{\text{HF}}(\mathbf{r}_1, \dots, \mathbf{r}_N) | H^{\text{el}} | \Psi^{\text{HF}}(\mathbf{r}_1, \dots, \mathbf{r}_N) \rangle. \quad (4.2)$$

By the application of Slater-Condon rules (see Appendix A) we can express Eq. (4.2) in terms of spin-orbitals, $\psi_i(\mathbf{r})$, to read

$$E^{\text{HF}} = \sum_{i=1}^N \int d\mathbf{r} \psi_i^*(\mathbf{r}) \left[-\frac{\hbar^2}{2m} \Delta_{\mathbf{r}} - V_N(\mathbf{r}) \right] \psi_i(\mathbf{r}) + \frac{1}{2} \sum_{m=1}^N \sum_{n=1}^N \langle \psi_m \psi_n | | \psi_m \psi_n \rangle. \quad (4.3)$$

The first term in the above equation accounts for the kinetic energy of the electrons. V_N denotes the external attractive nuclear potential as defined in Eq. (2.6). $\langle \psi_m \psi_n | | \psi_m \psi_n \rangle$ are antisymmetrized electron repulsion (or two-electron-four-orbital) integrals that are defined as

$$\langle \psi_m \psi_n | | \psi_m \psi_n \rangle = e^2 \int \int d\mathbf{r}_1 d\mathbf{r}_2 \left(\frac{\psi_m^*(\mathbf{r}_1) \psi_n^*(\mathbf{r}_2) \psi_m(\mathbf{r}_1) \psi_n(\mathbf{r}_2)}{|\mathbf{r}_1 - \mathbf{r}_2|} - \frac{\psi_m^*(\mathbf{r}_1) \psi_n^*(\mathbf{r}_2) \psi_n(\mathbf{r}_1) \psi_m(\mathbf{r}_2)}{|\mathbf{r}_1 - \mathbf{r}_2|} \right). \quad (4.4)$$

Equations (3.4) and (4.4) allow for rearranging the last term on the right-hand side of Eq. (4.3) as

$$\begin{aligned} \frac{1}{2} \sum_{m=1}^N \sum_{n=1}^N \langle \psi_m \psi_n | | \psi_m \psi_n \rangle &= \frac{1}{2} \sum_{m=1}^N \int d\mathbf{r}_1 \psi_m^*(\mathbf{r}_1) V_H(\mathbf{r}_1) \psi_m(\mathbf{r}_1) \\ &\quad + \frac{1}{2} \sum_{m=1}^N \int d\mathbf{r}_1 \int d\mathbf{r}_2 \psi_m^*(\mathbf{r}_1) V_X(\mathbf{r}_1, \mathbf{r}_2) \psi_m(\mathbf{r}_2), \end{aligned} \quad (4.5)$$

where

$$V_X(\mathbf{r}_1, \mathbf{r}_2) = -e^2 \sum_{n=1}^N \frac{\psi_n^*(\mathbf{r}_1) \psi_n(\mathbf{r}_2)}{|\mathbf{r}_1 - \mathbf{r}_2|}. \quad (4.6)$$

V_H and V_X are the Hartree and exchange potential, respectively. At this point we emphasize three aspects of V_X in the HF approximation (i) it is *non-local*, (ii) it is a direct consequence of the antisymmetry of the wave function and (iii) it cures the “unphysical” self-interaction of an electron that feels its own Hartree potential exactly.

In principle, DFT accounts for the effects of V_X as well, but in practice no density functional approximation to V_X is exact for anything but the homogeneous electron gas.

According to the variational principle, the Hartree-Fock energy is an upper bound of the exact energy [9]. Therefore the “best” Hartree-Fock spin-orbitals $\psi_i(\mathbf{r})$ are those which minimize the Hartree-Fock energy, E^{HF} . By varying the orbitals until the energy is a minimum one obtains the so-called Hartree-Fock integro-differential equation (Euler equation)

$$\left[-\frac{\hbar^2}{2m} \Delta_{\mathbf{r}} - V_N(\mathbf{r}) \right] \psi_i(\mathbf{r}) + V_H(\mathbf{r}) \psi_i(\mathbf{r}) + \int d\mathbf{r}' V_X(\mathbf{r}, \mathbf{r}') \psi_i(\mathbf{r}') = \epsilon_i \psi_i(\mathbf{r}), \quad (4.7)$$

where the orbitals are subject to the constraint to remain orthonormal

$$\int d\mathbf{r} \psi_i(\mathbf{r})^* \psi_j(\mathbf{r}) = \delta_{ij}. \quad (4.8)$$

Solving Eq. (4.7) self-consistently yields the Hartree-Fock spin-orbitals, ψ_i , and the corresponding orbital eigenenergies, ϵ_i . The N orbitals $\{\psi_1, \psi_2, \dots, \psi_N\}$ with the the lowest eigenenergies $\{\epsilon_1, \epsilon_2, \dots, \epsilon_N\}$ are called *occupied orbitals*. All orbitals with higher eigenenergies are referred to as *unoccupied* or *virtual orbitals*.

Equation (4.7) can be written in terms of the Fock operator, \hat{f}_i , to read as

$$\hat{f}_i \psi_i(\mathbf{r}) = \epsilon_i \psi_i(\mathbf{r}), \quad (4.9)$$

where \hat{f}_i operates on the i -th orbital and is implicitly defined through Eq. (4.7). *Canonical orbitals* diagonalize the matrix elements of the Fock operator

$$f_i^j = \langle \psi_j | \hat{f}_i | \psi_i \rangle = \delta_{ij} \epsilon_i. \quad (4.10)$$

$|\Psi^{\text{HF}}\rangle$ is the *exact solution* to the so-called *Hartree-Fock Hamiltonian*, $H^{(0)}$, that is constructed from the sum of one-electron Fock operators [9]

$$H^{(0)} |\Psi^{\text{HF}}\rangle = \sum_{i=1}^N \hat{f}_i |\Psi^{\text{HF}}\rangle = E^{(0)} |\Psi^{\text{HF}}\rangle, \quad (4.11)$$

where

$$E^{(0)} = \sum_i^{\text{occ.}} \epsilon_i. \quad (4.12)$$

N.B. the Hartree-Fock energy, E^{HF} , is *not* the sum of the occupied one-electron eigenvalues

$$E^{\text{HF}} \neq \sum_i^{\text{occ.}} \epsilon_i, \quad (4.13)$$

but

$$E^{\text{HF}} = \sum_i^{\text{occ.}} \epsilon_i - \frac{1}{2} \sum_{jk}^{\text{occ.}} \langle jk || jk \rangle. \quad (4.14)$$

Chapter 5

Correlation in wave function based methods

The correlation energy, E_C , is defined as the difference between the exact electronic ground state energy, E_{GS} , and the Hartree-Fock energy, E_{HF} ,

$$E_C = E_{GS} - E_{HF}. \quad (5.1)$$

We know from the variational principle that $E_{HF} \geq E_{GS}$. Therefore, the correlation energy, E_C , must be zero or negative. Correlation lowers the energy compared to HF by allowing the electrons to remain spatially separated, a requirement imposed by the repulsive electron-electron Coulomb kernel. In fact, the Coulomb kernel, $\frac{1}{|\mathbf{r}_i - \mathbf{r}_j|}$, exhibits singularities at the collision points between two electrons, $\mathbf{r}_{ij} = |\mathbf{r}_i - \mathbf{r}_j| = 0$, implying that the Coulomb repulsion at the collision points becomes infinite. To compensate for the infinite Coulomb potential, the wave function is discontinuous at the collision points and thereby develops an infinitely large kinetic energy density. This leads to the so-called Kato cusp condition for the exact many-electron wave function that reads [10]

$$\left. \frac{\partial \left(\frac{\Psi(\mathbf{r}_{ij})}{\Psi(0)} \right)}{\partial \mathbf{r}_{ij}} \right|_{\mathbf{r}_{ij}=0} = const. \quad (5.2)$$

A single Slater determinant (as it is used in HF) does not have enough variational freedom to describe such a discontinuity. To this end, so-called *excited* Slater determinants are added to the Hartree-Fock determinant as Ansatz for the many-electron wave function. Excited Slater determinants, $\Psi_{ij\dots m}^{ab\dots e}$, correspond to Hartree-Fock determinants in which one, two, ..., N occupied orbitals

$\psi_i, \psi_j, \dots, \psi_m$ are replaced by *virtual* orbitals $\psi_a, \psi_b, \dots, \psi_e$, respectively. Electron creation, p_a^\dagger , and annihilation, p_i , operators are used to construct excited determinants by acting on a reference state $|\Psi^{\text{HF}}\rangle$,

$$|\Psi_i^a\rangle = p_a^\dagger p_i |\Psi^{\text{HF}}\rangle \quad (5.3)$$

$$|\Psi_{ij}^{ab}\rangle = p_a^\dagger p_b^\dagger p_i p_j |\Psi^{\text{HF}}\rangle \quad (5.4)$$

....

These singly, doubly, ..., N -tuply excited determinants form a complete orthogonal basis for the many-electron wave function:

$$\begin{aligned} \langle \Psi_{ij..m}^{ab..e} | \Psi_{i'j'..m'}^{a'b'..e'} \rangle &= \delta_{i,i'} \delta_{j,j'} \dots \delta_{m,m'} \delta_{a,a'} \delta_{b,b'} \dots \delta_{e,e'}, \text{ and} \\ \langle \Psi^{\text{HF}} | \Psi_{i..m}^{a..e} \rangle &= 0. \end{aligned} \quad (5.5)$$

We note that, all excited Slater determinants are eigenfunctions of $H^{(0)}$ as defined in Eq. (4.11)

$$H^{(0)} |\Psi_{ij}^{ab}\rangle = E_{ij}^{ab} |\Psi_{ij}^{ab}\rangle, \quad (5.6)$$

where

$$E_{ij}^{ab} = \left(\sum_k^{\text{occ.}} \epsilon_k \right) - \epsilon_i - \epsilon_j + \epsilon_a + \epsilon_b. \quad (5.7)$$

This applies to any excited determinant, not just doubles, as exemplified in the equations above.

5.1 Second-order Møller-Plesset perturbation theory

Chr. Møller and M. S. Plesset derived in 1934 an expression for the ground state energy from Rayleigh-Schrödinger perturbation theory [11]. In their derivation the unperturbed Hamiltonian is chosen such that the Hartree-Fock energy appears as the zero-order energy and the first-order contribution vanishes. The second-order contribution to the energy is referred to as MP2 correlation energy in the following. These days, the MP2 method is one of several *post-Hartree-Fock* methods frequently used in the field of quantum chemistry. One reason for the popularity of the MP2 method is its ability to capture Van der Waals interactions that are not accounted for by the HF approximation.

Moreover relative energies as well as bond-lengths are significantly improved compared to HF, in particular for elements in the main group. Furthermore the inclusion of higher orders of the perturbation series allows for systematic studies, where MP2 constitutes only the second step after a HF calculation. In the following, we will derive the MP2 energy in a slightly different manner than outlined in Ref. [11], which, however, yields the same result [9]. We choose the unperturbed Hamiltonian, $H^{(0)}$, to be the *Hartree-Fock Hamiltonian* [see Eq. (4.11)]. Hence the unperturbed ($\lambda = 0$) and fully perturbed ($\lambda = 1$) Hamiltonian read

$$\bar{H} = H^{(0)} + \lambda(H - H^{(0)}), \text{ where} \quad (5.8)$$

H denotes the electronic Hamiltonian [see Eq. (2.5)]. $(H - H^{(0)})$ is also referred to as *fluctuation potential*.

From perturbation theory we know that

$$\begin{aligned} (H^{(0)} + \lambda[H - H^{(0)}])(\Psi^{(0)} + \lambda\Psi^{(1)} + \lambda^2\Psi^{(2)} \dots) &= (E^{(0)} + \lambda E^{(1)} + \lambda^2 E^{(2)} \dots) \\ &\times (\Psi^{(0)} + \lambda\Psi^{(1)} + \lambda^2\Psi^{(2)} + \dots). \end{aligned} \quad (5.9)$$

The essential assumption of perturbation theory is that the fluctuation potential corresponds to a small perturbation to $H^{(0)}$, such that Eq. (5.9) converges rapidly with respect to orders of λ . In Eq. (5.9), $E^{(0)}$ and $\Psi^{(0)}$ are the lowest eigenvalue and the corresponding eigenfunction of the unperturbed Hamiltonian, $H^{(0)}$ [see Eq. (4.11)], respectively. We know from Eq. (4.12) and Eq. (4.11) that

$$E^{(0)} = \sum_i^{\text{occ.}} \epsilon_i \quad (5.10)$$

and

$$\Psi^{(0)} = \Psi^{\text{HF}}. \quad (5.11)$$

$\Psi^{(1)}$ is expanded into a basis of excited Hartree-Fock determinants,

$$|\Psi^{(1)}\rangle = e^{\mathbf{T}_2} |\Psi^{\text{HF}}\rangle, \quad (5.12)$$

where

$$e^{\mathbf{T}_2} = 1 + \mathbf{T}_2 + \frac{1}{2!} \mathbf{T}_2^2 + \frac{1}{3!} \mathbf{T}_2^3 + \dots = \sum_{k=0}^{\infty} \frac{1}{k!} \mathbf{T}_2^k. \quad (5.13)$$

\mathbf{T}_2 is a double excitation operator that creates excited Slater determinants with coefficients t_{ij}^{ab} :

$$\mathbf{T}_2|\Psi^{\text{HF}}\rangle = \sum_{i<j}^{\text{occ.}} \sum_{a<b}^{\text{unocc.}} t_{ij}^{ab} p_a^\dagger p_b^\dagger p_i p_j |\Psi^{\text{HF}}\rangle = \sum_{i<j}^{\text{occ.}} \sum_{a<b}^{\text{unocc.}} t_{ij}^{ab} |\Psi_{ij}^{ab}\rangle. \quad (5.14)$$

Up to N -tuply excited determinants are included in $\Psi^{(1)}$ that are constructed from products of double-excitation operators e.g.

$$\mathbf{T}_2 \mathbf{T}_2 |\Psi^{\text{HF}}\rangle = \sum_{i<j<k<l}^{\text{occ.}} \sum_{a<b<c<d}^{\text{unocc.}} t_{ij}^{ab} t_{kl}^{cd} |\Psi_{ijkl}^{abcd}\rangle, \quad (5.15)$$

...

where N is the number of electrons. The MP2 energy is defined as the sum of $E^{(i)}$ truncated at second-order

$$E^{\text{MP2}} = E^{(0)} + E^{(1)} + E^{(2)}. \quad (5.16)$$

Inserting the Ansatz for $\Psi^{(1)}$ from Eq. (5.12) into Eq. (5.9) yields

$$\begin{aligned} & (H^{(0)} + \lambda(H - H^{(0)}))(|\Psi^{\text{HF}}\rangle + \lambda|e^{\mathbf{T}_2}\Psi^{\text{HF}}\rangle + \lambda^2\Psi^{(2)} + \dots) = \\ & [E^{(0)} + \lambda E^{(1)} + \lambda^2 E^{(2)} + \dots] (|\Psi^{\text{HF}}\rangle + \lambda|e^{\mathbf{T}_2}\Psi^{\text{HF}}\rangle + \lambda^2\Psi^{(2)} + \dots). \end{aligned} \quad (5.17)$$

Collating all terms from Eq. (5.17) linear and quadratic in λ results in

$$H^{(0)}|e^{\mathbf{T}_2}\Psi^{\text{HF}}\rangle + (H - H^{(0)})|\Psi^{\text{HF}}\rangle = E^{(0)}|e^{\mathbf{T}_2}\Psi^{\text{HF}}\rangle + E^{(1)}|\Psi^{\text{HF}}\rangle \quad (5.18)$$

and

$$H^{(0)}|\Psi^{(2)}\rangle + (H - H^{(0)})|e^{\mathbf{T}_2}\Psi^{\text{HF}}\rangle = E^{(0)}|\Psi^{(2)}\rangle + E^{(1)}|e^{\mathbf{T}_2}\Psi^{\text{HF}}\rangle + E^{(2)}|\Psi^{\text{HF}}\rangle, \quad (5.19)$$

respectively.

Multiplying Eq. (5.18) from the left with $\langle\Psi_{ij}^{ab}|$ yields

$$\begin{aligned} & \underbrace{\langle\Psi_{ij}^{ab}|H^{(0)}|e^{\mathbf{T}_2}\Psi^{\text{HF}}\rangle}_{=E_{ij}^{ab}t_{ij}^{ab}} + \underbrace{\langle\Psi_{ij}^{ab}|(H - H^{(0)})|\Psi^{\text{HF}}\rangle}_{=\langle\Psi_{ij}^{ab}|H|\Psi^{\text{HF}}\rangle} = \\ & \underbrace{\langle\Psi_{ij}^{ab}|E^{(0)}|e^{\mathbf{T}_2}\Psi^{\text{HF}}\rangle}_{=E^{(0)}t_{ij}^{ab}} + \underbrace{\langle\Psi_{ij}^{ab}|E^{(1)}|\Psi^{\text{HF}}\rangle}_{=0}. \end{aligned} \quad (5.20)$$

In the above equation the last term on the right-hand side vanishes due to the orthogonality of the Slater determinants. It follows from Eqs. (5.7) and (5.10) that

$$E_{ij}^{ab} - E^{(0)} = \epsilon_a + \epsilon_b - \epsilon_i - \epsilon_j. \quad (5.21)$$

Solving Eq. (5.20) for t_{ij}^{ab} and inserting Eq. (5.21) yields the coefficients of $\Psi^{(1)}$

$$t_{ij}^{ab} = -\frac{\langle \Psi_{ij}^{ab} | H | \Psi^{\text{HF}} \rangle}{\epsilon_a + \epsilon_b - \epsilon_i - \epsilon_j}. \quad (5.22)$$

Employing Slater-Condon rules (see Appendix A) allows to express $\langle \Psi_{ij}^{ab} | H | \Psi^{\text{HF}} \rangle$ in terms of one-electron orbitals

$$\langle \Psi_{ij}^{ab} | H | \Psi^{\text{HF}} \rangle = \langle ab || ij \rangle = e^2 \int d\mathbf{r}_1 \int d\mathbf{r}_2 \left[\frac{\psi_a^*(\mathbf{r}_1) \psi_b^*(\mathbf{r}_2) \psi_i(\mathbf{r}_1) \psi_j(\mathbf{r}_2)}{|\mathbf{r}_1 - \mathbf{r}_2|} - \frac{\psi_b^*(\mathbf{r}_1) \psi_a^*(\mathbf{r}_2) \psi_i(\mathbf{r}_1) \psi_j(\mathbf{r}_2)}{|\mathbf{r}_1 - \mathbf{r}_2|} \right]. \quad (5.23)$$

In passing we note that the coefficients, t_{ij}^{ab} , fulfill the following permutation symmetries

$$t_{ij}^{ab} = t_{ji}^{ba} = -t_{ji}^{ab} = -t_{ij}^{ba}. \quad (5.24)$$

E^{MP2} can be calculated by multiplying Eq. (5.19) from the left with $\langle \Psi^{\text{HF}} |$, which yields

$$\underbrace{\langle \Psi^{\text{HF}} | H^{(0)} | \Psi^{(2)} \rangle}_{=\langle \Psi^{\text{HF}} | E^{(0)} | \Psi^{(2)} \rangle} + \underbrace{\langle \Psi^{\text{HF}} | (H - H^{(0)}) | e^{\mathbf{T}_2} \Psi^{\text{HF}} \rangle}_{=\langle \Psi^{\text{HF}} | H | e^{\mathbf{T}_2} \Psi^{\text{HF}} \rangle - E^{(0)}} = \langle \Psi^{\text{HF}} | E^{(0)} | \Psi^{(2)} \rangle + \underbrace{\langle \Psi^{\text{HF}} | E^{(1)} | e^{\mathbf{T}_2} \Psi^{\text{HF}} \rangle}_{=E^{(1)}} + \underbrace{\langle \Psi^{\text{HF}} | E^{(2)} | \Psi^{\text{HF}} \rangle}_{=E^{(2)}}. \quad (5.25)$$

From Eq. (5.25) it follows that

$$\langle \Psi^{\text{HF}} | H | e^{\mathbf{T}_2} \Psi^{\text{HF}} \rangle = E^{(0)} + E^{(1)} + E^{(2)}. \quad (5.26)$$

Rearranging the above expression and inserting Eq. (5.16) yields

$$E^{\text{MP2}} = \langle \Psi^{\text{HF}} | H | e^{\mathbf{T}_2} \Psi^{\text{HF}} \rangle = \langle \Psi^{\text{HF}} | H | \Psi^{\text{HF}} \rangle + E_C^{\text{MP2}}, \quad (5.27)$$

where

$$E_C^{\text{MP2}} = \langle \Psi^{\text{HF}} | H | \sum_{k=1}^{\infty} \frac{1}{k!} \mathbf{T}_2^k | \Psi^{\text{HF}} \rangle. \quad (5.28)$$

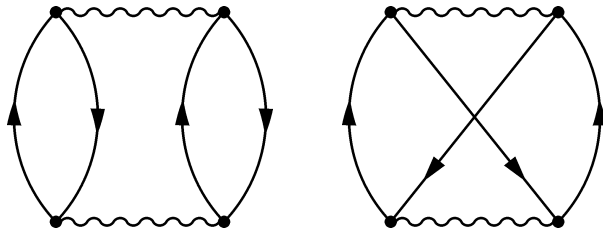


Figure 5.1: MP2 direct (left) and exchange-like (right) term.

Hence, we find that the MP2 energy is the sum of the Hartree-Fock energy plus the MP2 correlation energy, E_C^{MP2} . Employing Slater-Condon rules (see Appendix A) allows to express Eq. (5.28) in terms of spin-orbitals to read

$$E_C^{\text{MP2}} = \frac{1}{4} \sum_{ij}^{\text{occ.}} \sum_{ab}^{\text{unocc.}} t_{ij}^{ab} \langle ij || ab \rangle. \quad (5.29)$$

Inserting Eq. (5.22) into Eq. (5.29) yields the final MP2 correlation energy expression

$$E_C^{\text{MP2}} = \frac{1}{4} \sum_{ij}^{\text{occ.}} \sum_{ab}^{\text{unocc.}} \frac{|\langle ij || ab \rangle|^2}{\epsilon_i + \epsilon_j - \epsilon_a - \epsilon_b}. \quad (5.30)$$

One comment is in place here: In deriving Eqs. (5.30) and (5.22), we have assumed canonical orbitals, which ensures that all contributions from single-excitations vanish because of the *Brillouin theorem*, which reads [9]

$$\langle \Psi_i^a | H | \Psi^{\text{HF}} \rangle = f_i^a = 0. \quad (5.31)$$

Equation (5.30) can easily be generalized to non-spin-polarized systems where it reads

$$E_C^{\text{MP2}} = \sum_{ij}^{\text{occ.}} \sum_{ab}^{\text{unocc.}} \frac{\langle ij | ab \rangle (2\langle ab | ij \rangle - \langle ba | ij \rangle)}{\epsilon_i + \epsilon_j - \epsilon_a - \epsilon_b}. \quad (5.32)$$

In the above equation, i, j and a, b denote occupied and unoccupied spatial orbitals, respectively.

In the field of quantum chemistry, Goldstone diagrams are used to express algebraic expressions such as Eq. (5.32) [9]. Figure 5.1 shows the Goldstone

diagrams corresponding to Eq. (5.32). The direct and exchange-like diagrams correspond to

$$E_C^{dMP2} = \sum_{ij}^{\text{occ.}} \sum_{ab}^{\text{unocc.}} \frac{2|\langle ij|ab\rangle|^2}{\epsilon_i + \epsilon_j - \epsilon_a - \epsilon_b}, \quad (5.33)$$

and

$$E_C^{SOX} = - \sum_{ij}^{\text{occ.}} \sum_{ab}^{\text{unocc.}} \frac{\langle ij|ab\rangle \langle ba|ij\rangle}{\epsilon_i + \epsilon_j - \epsilon_a - \epsilon_b}, \quad (5.34)$$

respectively. The exchange-like term is also referred to as second-order exchange.

Our MP2 implementation in VASP scales as $\mathcal{O}(N^5)$, where N is a measure of the system size. For further details on the implementation of the MP2 method in VASP the reader is referred to Sec. 8.3 and Appendix C. In section 5.6 we outline an alternative way to evaluate Eq. (5.33) that exhibits a more favorable scaling of the computational effort with respect to the system size [i.e. $\mathcal{O}(N^4)$].

5.2 Coupled-Cluster singles and doubles theory

The coupled-cluster method was initially proposed by Fritz Coester and Hermann Kümmel for applications in the field of nuclear physics [13, 14]. In 1966, Jiří Čížek reformulated the method for electron correlation in atoms and molecules [15], where it became a standard for quantum chemical calculations on systems that do not exhibit strong static correlation [16, 17, 18, 19]. The Ansatz for the coupled-cluster wave function is, like in MP2, an exponential Ansatz that reads

$$|\Psi^{\text{CC}}\rangle = e^{\mathbf{T}}|\Psi^{\text{HF}}\rangle, \quad (5.35)$$

where

$$e^{\mathbf{T}} = 1 + \mathbf{T} + \frac{1}{2!}\mathbf{T}^2 + \frac{1}{3!}\mathbf{T}^3 + \dots = \sum_{k=0}^{\infty} \frac{1}{k!}\mathbf{T}^k. \quad (5.36)$$

However, in coupled-cluster singles and doubles (CCSD) theory the excitation operator \mathbf{T} is a sum of single- as well as double-excitation operators.

$$\mathbf{T} = \mathbf{T}_1 + \mathbf{T}_2, \text{ where} \quad (5.37)$$

$$\mathbf{T}_1|\Psi^{\text{HF}}\rangle = \sum_i^{\text{occ.}} \sum_a^{\text{unocc.}} t_i^a |\Psi_i^a\rangle, \quad (5.38)$$

$$\mathbf{T}_2|\Psi^{\text{HF}}\rangle = \sum_{i<j}^{\text{occ.}} \sum_{a<b}^{\text{unocc.}} t_{ij}^{ab} |\Psi_{ij}^{ab}\rangle. \quad (5.39)$$

The sets $\{t_i^a\}$ and $\{t_{ij}^{ab}\}$ are the coefficients of the CCSD wave function and are also referred to as single and double amplitudes, respectively. Higher orders of coupled-cluster theories, such as CCSDT., are obtained by including higher orders of excitation operators in \mathbf{T} ($=\mathbf{T}_1 + \mathbf{T}_2 + \mathbf{T}_3 + \dots$).

Up to N -tuply excited determinants are included in the CCSD wave function that are constructed from products of single- and double-excitation operators e.g.

$$\mathbf{T}_1\mathbf{T}_2|\Psi^{\text{HF}}\rangle = \sum_{i<j<k}^{\text{occ.}} \sum_{a<b<c}^{\text{unocc.}} t_i^a t_{jk}^{bc} |\Psi_{ijk}^{abc}\rangle, \quad (5.40)$$

$$\mathbf{T}_2\mathbf{T}_2|\Psi^{\text{HF}}\rangle = \sum_{i<j<k<l}^{\text{occ.}} \sum_{a<b<c<d}^{\text{unocc.}} t_{ij}^{ab} t_{kl}^{cd} |\Psi_{ijkl}^{abcd}\rangle. \quad (5.41)$$

...

Inserting Eq. (5.35) into the Schrödinger equation yields

$$H|e^{\mathbf{T}}\Psi^{\text{HF}}\rangle = E^{\text{CCSD}}|e^{\mathbf{T}}\Psi^{\text{HF}}\rangle. \quad (5.42)$$

Multiplying Eq. (5.42) from the left with $\langle\Psi^{\text{HF}}|$ gives

$$\langle\Psi^{\text{HF}}|H|e^{\mathbf{T}}\Psi^{\text{HF}}\rangle = E^{\text{CCSD}}\langle\Psi^{\text{HF}}|e^{\mathbf{T}}\Psi^{\text{HF}}\rangle, \quad (5.43)$$

which can be rearranged as the sum of the Hartree-Fock energy, E^{HF} , and the CCSD correlation energy, E_C^{CCSD} :

$$E^{\text{CCSD}} = E^{\text{HF}} + E_C^{\text{CCSD}}, \quad (5.44)$$

where

$$E_C^{\text{CCSD}} = \langle\Psi^{\text{HF}}|H|\sum_{k=1}^{\infty} \frac{1}{k!} \mathbf{T}^k \Psi^{\text{HF}}\rangle. \quad (5.45)$$

Employing Slater-Condon rules (see Appendix A) to express the correlation energy in terms of electron repulsion integrals and amplitudes yields

$$E_C^{\text{CCSD}} = \sum_{ij}^{\text{occ.}} \sum_{ab}^{\text{unocc.}} \left(\frac{1}{2} t_i^a t_j^b + \frac{1}{4} t_{ij}^{ab} \right) \langle ij || ab \rangle. \quad (5.46)$$

Only squared single amplitudes and double amplitudes occur in the expression of the CCSD correlation energy. Higher excitations do not contribute to the correlation energy directly because the electronic Hamiltonian contains at most two-electron operators (*i.e.* the electron-electron Coulomb interaction). Equation (5.46) holds for canonical orbitals only because of the Brillouin theorem ($\langle \Psi_i^a | H | \Psi^{\text{HF}} \rangle = 0$) [9]. In coupled-cluster theory the coefficients of the CCSD wave function t_i^a and t_{ij}^{ab} are calculated from the amplitude equations. Multiplication of Eq. (5.42) from the left with singly- and doubly- excited Slater determinants yields the single and double amplitude equations, respectively

$$\langle \Psi_i^a | H | e^{\mathbf{T}} \Psi^{\text{HF}} \rangle = \langle \Psi_i^a | E^{\text{CCSD}} | e^{\mathbf{T}} \Psi^{\text{HF}} \rangle \quad (5.47)$$

$$\langle \Psi_{ij}^{ab} | H | e^{\mathbf{T}} \Psi^{\text{HF}} \rangle = \langle \Psi_{ij}^{ab} | E^{\text{CCSD}} | e^{\mathbf{T}} \Psi^{\text{HF}} \rangle. \quad (5.48)$$

The above set of equations are the so-called *general CCSD equations*. In some of the first computer implementations of the CCSD method, Eqs. (5.47) and (5.48) served as amplitude equations [17].

An explicit dependence of the amplitudes on the CCSD energy emerges from the terms on the right-hand sides in Eqs. (5.47) and (5.48), which makes it inconvenient for implementations. With some mathematical foresight, one finds that it is more efficient to multiply Eq. (5.42) from the left with $\langle \Psi_i^a | e^{-\mathbf{T}}$ and $\langle \Psi_{ij}^{ab} | e^{-\mathbf{T}}$, respectively:

$$\langle \Psi_i^a | e^{-\mathbf{T}} H e^{\mathbf{T}} | \Psi^{\text{HF}} \rangle = \langle \Psi_i^a | e^{-\mathbf{T}} E^{\text{CCSD}} e^{\mathbf{T}} | \Psi^{\text{HF}} \rangle, \quad (5.49)$$

$$\langle \Psi_{ij}^{ab} | e^{-\mathbf{T}} H e^{\mathbf{T}} | \Psi^{\text{HF}} \rangle = \langle \Psi_{ij}^{ab} | e^{-\mathbf{T}} E^{\text{CCSD}} e^{\mathbf{T}} | \Psi^{\text{HF}} \rangle. \quad (5.50)$$

Like $e^{\mathbf{T}}$ is an excitation operator working on the function on the right, $e^{-\mathbf{T}}$ is a de-excitation operator working on the function on the left [9]. The right-hand sides of Eqs. (5.49) and (5.50) vanish due to the orthogonality of the Slater determinantal basis. Hence, the single and double amplitude equations read

$$\langle \Psi_i^a | e^{-\mathbf{T}} H e^{\mathbf{T}} | \Psi^{\text{HF}} \rangle = 0 \quad \text{and} \quad (5.51)$$

$$\langle \Psi_{ij}^{ab} | e^{-\mathbf{T}} H e^{\mathbf{T}} | \Psi^{\text{HF}} \rangle = 0, \quad (5.52)$$

respectively. The sets of single and double amplitudes $\{t_i^a\}$ and $\{t_{ij}^{ab}\}$ that solve Eqs. (5.51) and (5.52) are used to calculate the energy in Eq. (5.46). Expressing Eqs. (5.51) and (5.52) in terms of one-electron orbitals in order to obtain a

set of equations that are suitable for an implementation on the computer, is not straightforward. The derivation quickly turns into a formidable task because of the large number of terms involved. Therefore computer programs for an automated derivation of the amplitude equations have been implemented [20]. The implementation by S. Hirata in Ref. [20] relies on a second-quantized representation of the respective many-body theory. Since it would be beyond the scope of this work to explain the automated derivation, we restrict ourselves to giving the expressions of the amplitude equations that have been implemented in VASP.

5.2.1 Unrestricted CCSD amplitude equations

The following amplitude equations for spin-polarized reference determinants have been implemented in VASP. They were derived by a program of S. Hirata in Ref. [20]. In the following i, j, k, l, m, n, o and a, b, c, d, e, f, g, h denote occupied and unoccupied spin-orbitals, respectively. The single and double amplitude equations read

$$\begin{aligned}
0 = & f_i^a - \sum_k f_i^k t_k^a + \sum_b f_b^a t_i^b - \sum_{lb} t_l^b \langle la || ib \rangle + \sum_{kc} f_c^k t_{ki}^{ca} \frac{1}{2} \sum_{lmb} t_{lm}^{ba} \langle lm || ib \rangle \\
& \frac{1}{2} \sum_{mbc} t_{mi}^{bc} \langle ma || bc \rangle - \sum_{lb} t_i^b t_l^a f_b^l - \sum_{kmc} t_k^a t_m^c \langle km || ic \rangle \\
& - \sum_{mbc} t_i^b t_m^c \langle ma || bc \rangle - \frac{1}{2} \sum_{lmbe} t_{lm}^{ba} t_i^e \langle lm || be \rangle - \frac{1}{2} \sum_{mnbc} t_{mi}^{bc} t_n^a \langle mn || bc \rangle \\
& + \sum_{lnbd} t_{li}^{ba} t_n^d \langle ln || bd \rangle - \sum_{lnbd} t_i^b t_l^a t_n^d \langle ln || bd \rangle
\end{aligned} \tag{5.53}$$

and

$$\begin{aligned}
0 = & \langle ab || ij \rangle - \sum_m t_m^a \langle mb || ij \rangle + P(abij \rightarrow baij) \sum_m t_m^a \langle mb || ij \rangle \\
& + [1 - P(abji \rightarrow abij)] \sum_e t_j^e \langle ab || ie \rangle - [1 - P(abij \rightarrow abji)] \sum_m f_i^m t_{mj}^{ab} \\
& - [1 - P(baij \rightarrow abij)] \sum_e f_e^b t_{ij}^{ea} + \frac{1}{2} \sum_{mn} t_{mn}^{ab} \langle mn || ij \rangle \\
& + [1 - P(abji \rightarrow baji) - P(abji \rightarrow abij) + P(abji \rightarrow baij)] \sum_{ne} t_{nj}^{ea} \langle nb || ie \rangle \\
& + \frac{1}{2} \sum_{ef} t_{ij}^{ef} \langle ab || ef \rangle + \sum_{mn} t_m^a t_n^b \langle mn || ij \rangle
\end{aligned}$$

$$\begin{aligned}
& - [1 - P(abji \rightarrow baji) - P(abji \rightarrow abij) + P(abji \rightarrow baij)] \sum_{ne} t_j^e t_n^a \langle nb || ie \rangle \\
& + \sum_{ef} t_i^e t_j^f \langle ab || ef \rangle - [1 - P(abji \rightarrow abij)] \sum_{mf} f_f^m t_{mj}^{ab} t_i^f \\
& + [1 - P(abij \rightarrow baij)] \sum_{mf} f_f^m t_{ij}^{fa} t_m^b + \left[\frac{1}{2} - \frac{1}{2} P(abji \rightarrow abij) \right] \sum_{mng} t_{mn}^{ab} t_j^g \langle mn || ig \rangle \\
& - [1 - P(abji \rightarrow baji) - P(abji \rightarrow abij) + P(abji \rightarrow baij)] \sum_{noe} t_{nj}^{ea} t_o^b \langle no || ie \rangle \\
& - [1 - P(abji \rightarrow abij)] \sum_{mof} t_{mj}^{ab} t_o^f \langle mo || if \rangle \\
& - [1 - P(abji \rightarrow baji) - P(abji \rightarrow abij) + P(abji \rightarrow baij)] \sum_{neg} t_{nj}^{ea} t_i^g \langle nb || eg \rangle \\
& - \left[\frac{1}{2} - \frac{1}{2} P(abij \rightarrow baij) \right] \sum_{oef} t_{ij}^{ef} t_o^a \langle ob || ef \rangle + [1 - P(abij \rightarrow baij)] \sum_{oef} t_{ij}^{ea} t_o^f \langle ob || ef \rangle \\
& + \left[\frac{1}{2} - \frac{1}{2} P(baij \rightarrow abij) \right] \sum_{opef} t_{ij}^{eb} t_{op}^{fa} \langle op || ef \rangle \\
& + \frac{1}{4} \sum_{opef} t_{ij}^{ef} t_{op}^{ab} \langle op || ef \rangle - \left[\frac{1}{2} - \frac{1}{2} P(abij \rightarrow abji) \right] \sum_{pfg} t_{mi}^{ab} t_{pj}^{fg} \langle mp || fg \rangle \\
& - [1 - P(baij \rightarrow abij)] \sum_{npeg} t_{ni}^{eb} t_{pj}^{ga} \langle np || eg \rangle + [1 - P(abji \rightarrow abij)] \sum_{noe} t_j^e t_n^a t_o^b \langle no || ie \rangle \\
& - [1 - P(abij \rightarrow baij)] \sum_{oef} t_i^e t_j^f t_o^a \langle ob || ef \rangle + \frac{1}{2} \sum_{opef} t_i^e t_j^f t_{op}^{ab} \langle op || ef \rangle \\
& + [1 - P(baij \rightarrow abij) - P(baij \rightarrow baji) + P(baij \rightarrow abji)] \sum_{npeg} t_i^e t_n^b t_{pj}^{ga} \langle np || eg \rangle \\
& + [1 - P(abij \rightarrow abji)] \sum_{opef} t_i^e t_o^f t_{pj}^{ab} \langle op || ef \rangle + \frac{1}{2} \sum_{mng} t_m^a t_n^b t_{ij}^{gh} \langle mn || gh \rangle \\
& - [1 - P(baij \rightarrow abij)] \sum_{mofh} t_m^b t_o^f t_{ij}^{ha} \langle mo || fh \rangle + \sum_{opef} t_i^e t_j^f t_o^a t_p^b \langle op || ef \rangle,
\end{aligned} \tag{5.54}$$

respectively. The Fock matrix elements f_y^x are defined by Eq. (4.10) and become diagonal in the case of canonical orbitals. In the above equation the permutation operator $P(baij \rightarrow abji)$ is defined as

$$P(wxyz \rightarrow w'x'y'z') \{ \dots \}_{xy}^{wz} = \{ \dots \}_{xy}^{wz} + \{ \dots \}_{x'y'}^{w'z'}. \tag{5.55}$$

Clearly a manual implementation of Eqs. (5.53) and (5.54) is very complicated and error-prone. Therefore a metaprogram was developed for an automated implementation in VASP. Although the automated implementation is not very efficient, it allows for the calculation of single atoms and small molecules using an unrestricted (spin-polarized) Hartree-Fock reference determinant.

Note that Eq. (5.54) contains up to four nested summations. As such, the evaluation of the computationally most demanding terms is carried out by looping over eight indices (including the indices i, j, a and b of the amplitudes) and requires a computational effort that scales as $\mathcal{O}(N^8)$, where N is a measure of the system size. However, it is straight-forward to reduce the scaling of the computational effort to $\mathcal{O}(N^6)$ by introducing intermediate quantities. As an example we reduce the scaling of the computational effort of the following term in Eq. (5.54) from $\mathcal{O}(N^8)$ to $\mathcal{O}(N^6)$:

$$\underbrace{\sum_{opef} t_i^e t_j^f t_{op}^{ab} \langle op || ef \rangle}_{\mathcal{O}(N^8)} = \sum_{op} \underbrace{t_{op}^{ab} \chi_{op}^{ij}}_{\mathcal{O}(N^6)}, \text{ where} \quad (5.56)$$

$$\chi_{op}^{ij} = \underbrace{\sum_{ef} t_i^e t_j^f \langle op || ef \rangle}_{\mathcal{O}(N^5)}. \quad (5.57)$$

Hence we find that the right-hand side of Eq. (5.56) can be evaluated at a computational effort that scales as $\mathcal{O}(N^6)$ only. The “price” one has to pay for reducing the computational cost is evidently the storage of the intermediate quantity χ_{op}^{ij} .

5.2.2 Restricted CCSD amplitude equations

In the case of restricted (non-spin-polarized) reference determinants, the CCSD amplitude equations can be greatly simplified by defining *spin-free* amplitudes and determinants. In the following i, j, k, l, m, n, o and a, b, c, d, e, f, g, h denote occupied and unoccupied spatial orbitals, respectively. The CCSD spin-free single- and double-excitation operators are defined by

$$\mathbf{T}_1 = \sum_i^{\text{occ.}} \sum_a^{\text{unocc.}} t_i^a (p_{a\uparrow}^\dagger p_{i\uparrow} + p_{a\downarrow}^\dagger p_{i\downarrow}) \quad (5.58)$$

and

$$\begin{aligned}
\mathbf{T}_2 = & \left(\frac{1}{2!}\right)^2 \sum_{ij}^{\text{occ.}} \sum_{ab}^{\text{unocc.}} (t_{ij}^{ab} - t_{ij}^{ba}) (p_{a\uparrow}^\dagger p_{i\uparrow} p_{b\uparrow}^\dagger p_{j\uparrow} + p_{a\downarrow}^\dagger p_{i\downarrow} p_{b\downarrow}^\dagger p_{j\downarrow}) \\
& + \left(\frac{1}{2!}\right)^2 \sum_{ij}^{\text{occ.}} \sum_{ab}^{\text{unocc.}} t_{ij}^{ab} (p_{a\uparrow}^\dagger p_{i\downarrow} p_{b\uparrow}^\dagger p_{j\downarrow} + p_{a\downarrow}^\dagger p_{i\uparrow} p_{b\downarrow}^\dagger p_{j\uparrow}) \\
& - \left(\frac{1}{2!}\right)^2 \sum_{ij}^{\text{occ.}} \sum_{ab}^{\text{unocc.}} t_{ij}^{ba} (p_{a\uparrow}^\dagger p_{i\downarrow} p_{b\downarrow}^\dagger p_{j\uparrow} + p_{a\downarrow}^\dagger p_{i\uparrow} p_{b\uparrow}^\dagger p_{j\downarrow}) \quad (5.59)
\end{aligned}$$

respectively [19]. The operator $p_{a\uparrow}^\dagger$ ($p_{i\uparrow}$) creates (annihilates) an electron in orbital a with spin eigenfunction \uparrow . Note that as a consequence of Eq. (5.59) we find that

$$t_{ij}^{ab} \neq -t_{ij}^{ba}. \quad (5.60)$$

Inserting Eqs. (5.58) and (5.59) into Eq. (5.51) yields the single amplitude equations [19]:

$$\begin{aligned}
0 = & f_i^a - 2 \sum_{kc} f_c^k t_k^a t_i^c + \sum_c \kappa_c^a t_i^c - \sum_k \kappa_i^k t_k^a + \sum_{kc} \sum_{k_k} \kappa_c^k (2t_{ki}^{ca} - t_{ik}^{ca}) + \sum_{kc} \kappa_c^k t_i^c t_k^a \\
& + \sum_{kc} \sum_{k_k} w_{ic}^{ak} t_k^c + \sum_{kcd} \sum_{k_k k_c} w_{cd}^{ak} t_{ik}^{cd} + \sum_{kcd} \sum_{k_k} w_{cd}^{ak} t_i^c t_k^d \\
& - \sum_{klc} \sum_{k_k k_l} w_{ic}^{kl} t_{kl}^{ac} - \sum_{klc} \sum_{k_l} w_{ic}^{kl} t_k^a t_l^c. \quad (5.61)
\end{aligned}$$

In the above equation, w_{ic}^{ak} are antisymmetrized two-electron-four-orbital integrals that are given by

$$w_{ic}^{ak} = \langle ak || ic \rangle. \quad (5.62)$$

The double amplitudes equations are obtained from inserting Eqs. (5.58) and (5.59) into Eq. (5.52) [21, 19]:

$$\begin{aligned}
0 = & v_{ab}^{ij*} + \sum_{kl} \sum_{k_k} k_k \chi_{ij}^{kl} t_{kl}^{ab} + \sum_{kl} \chi_{ij}^{kl} t_k^a t_l^b + \sum_{cd} \sum_{k_c} \chi_{cd}^{ab} t_{ij}^{cd} + \sum_{cd} \chi_{cd}^{ab} t_i^c t_j^d + P \sum_c \lambda_c^a t_{ij}^{cb} \\
& - P \sum_k \lambda_i^k t_{kj}^{ab} + P \sum_c \left(v_{ic}^{ab} - \sum_k v_{ic}^{kb} t_k^a \right) t_j^c - P \sum_k \left(v_{ij}^{ak} + \sum_c v_{ic}^{ak} t_j^c \right) t_k^b \\
& + P \sum_{kc} \sum_{k_k} (2\chi_{ic}^{ak} - \chi_{ci}^{ak}) t_{kj}^{cb} - P \sum_{kc} \sum_{k_k} \chi_{ic}^{ak} t_{kj}^{bc} - P \sum_{kc} \sum_{k_k} \chi_{ci}^{bk} t_{kj}^{ac}. \quad (5.63)
\end{aligned}$$

In the above equation v_{ab}^{ij} are two-electron-four-orbital integrals that are given by

$$v_{ab}^{ij} = \langle ij|ab \rangle. \quad (5.64)$$

Equations (5.63) and (5.61) contain the following intermediate quantities:

$$\kappa_i^k = f_i^k + \sum_{lcd} \sum_{k_l k_c} w_{cd}^{kl} t_{il}^{cd} + \sum_{lcd} \sum_{k_l} w_{cd}^{kl} t_i^c t_l^d, \quad (5.65)$$

$$\kappa_c^a = f_c^a - \sum_{kld} \sum_{k_k k_l} w_{cd}^{kl} t_{kl}^{ad} - \sum_{kld} \sum_{k_l} w_{cd}^{kl} t_k^a t_l^d, \quad (5.66)$$

$$\kappa_c^k = f_c^k + \sum_{ld} \sum_{k_l} w_{cd}^{kl} t_l^d, \quad (5.67)$$

$$\lambda_i^k = \kappa_i^k + \sum_c f_c^k t_i^c + \sum_{lc} \sum_{k_l} w_{ic}^{kl} t_l^c, \quad (5.68)$$

$$\lambda_c^a = \kappa_c^a + \sum_k f_c^k t_k^a + \sum_{kd} \sum_{k_k} w_{cd}^{ak} t_k^d, \quad (5.69)$$

$$\chi_{ij}^{kl} = v_{ij}^{kl} + \sum_c v_{ic}^{kl} t_j^c + \sum_c v_{cj}^{kl} t_i^c + \sum_{cd} \sum_{k_c} v_{cd}^{kl} t_{ij}^{cd} + \sum_{cd} v_{cd}^{kl} t_i^c t_j^d, \quad (5.70)$$

$$\chi_{cd}^{ab} = v_{cd}^{ab} - \sum_k v_{cd}^{ak} t_k^b - \sum_k v_{cd}^{kb} t_k^a, \quad (5.71)$$

$$\begin{aligned} \chi_{ic}^{ak} = & v_{ic}^{ak} - \sum_l v_{ic}^{lk} t_l^a + \sum_d v_{dc}^{ak} t_i^d - \frac{1}{2} \sum_{ld} \sum_{k_l} v_{dc}^{lk} t_{il}^{da} - \sum_{ld} v_{dc}^{lk} t_i^d t_l^a \\ & + \frac{1}{2} \sum_{ld} \sum_{k_l} w_{dc}^{lk} t_{il}^{ad} \text{ and} \end{aligned} \quad (5.72)$$

$$\chi_{ci}^{ak} = v_{ci}^{ak} - \sum_l v_{ci}^{lk} t_l^a + \sum_d v_{cd}^{ak} t_i^d - \frac{1}{2} \sum_{ld} \sum_{k_l} v_{cd}^{lk} t_{il}^{da} - \sum_{ld} v_{cd}^{lk} t_i^d t_l^a, \quad (5.73)$$

where P is the permutation operator

$$P \{ \dots \}_{ij}^{ab} = \{ \dots \}_{ij}^{ab} + \{ \dots \}_{ji}^{ba}. \quad (5.74)$$

As already outlined in Sec. 5.2.1 the intermediate quantities are introduced to reduce the scaling of the computational effort in the amplitude equations to $\mathcal{O}(N^6)$. Since all algebraic operations in the above equations correspond to matrix-matrix multiplications, these equations were implemented in VASP using BLAS libraries. Furthermore the intermediate quantities as well as amplitudes are distributed according to efficient parallelization strategies.

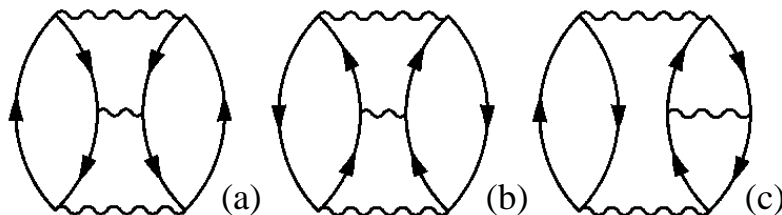


Figure 5.2: Diagrams containing (a) particle-particle, (b) hole-hole and (c) particle-hole interactions. The wiggly line represents the unscreened Coulomb interaction.

5.3 Notes on CCSD and MP2

The solution of the amplitude equations [see Eqs. (5.53), (5.54), (5.61) and (5.63)] leads to the inclusion of infinitely many Goldstone diagrams of a certain type in the CCSD correlation energy. This is in contrast to N th-order perturbation theory, which only includes diagrams up to order N . Moreover CCSD is exact to third-order. As such, we can put HF, MP2 and CCSD in a hierarchy of methods with increasing accuracy that reads

$$\text{HF} < \text{MP2} < \text{CCSD}. \quad (5.75)$$

The type of diagrams that are included in MP2 and CCSD enables us to make a statement about their accuracy for weakly/strongly polarizable systems. Particle-particle and hole-hole ladder diagrams, are claimed to be relevant for weakly polarizable systems [22]. On the other hand, for strongly polarizable solids, higher order diagrams, specifically, the summation of all bubble diagrams, as included in the random phase approximation (we will come back to that later), are important. MP2 neglects particle-particle, particle-hole and hole-hole ladder diagrams. Moreover MP2 includes only a second-order bubble-diagram, which is also referred to as direct MP2 term (see Fig. 5.1). As such MP2 is expected to be accurate only for systems with an intermediate polarizability. We note that MP2 even diverges for three dimensional metallic systems (i.e. systems with infinite polarizability) [12].

CCSD contains particle-particle, particle-hole, hole-hole ladder (see Fig. 5.2) as well as infinitely many bubble (or ring) diagrams. As such the accuracy of CCSD should depend only little on the polarizability of the system. Moreover we stress that CCSD is exact for any two-electron system.

5.3.1 MP2 and CCSD energies are not variational

It is important to note that in contrast to HF, MP2 and CCSD are not variational methods. There is no guarantee that the resulting total energy is an upper bound of the exact energy, E_{exact} . The electronic energy in MP2 and CCSD is given by

$$E = \langle \Psi^{\text{HF}} | H | e^{\mathbf{T}} \Psi^{\text{HF}} \rangle, \quad (5.76)$$

where

$$\mathbf{T} = \begin{cases} \mathbf{T}_2 & \text{in MP2} \\ \mathbf{T}_1 + \mathbf{T}_2 & \text{in CCSD.} \end{cases} \quad (5.77)$$

An expansion of $|\Psi^{\text{HF}}\rangle$ and $|e^{\mathbf{T}}\Psi^{\text{HF}}\rangle$ over a set of eigenfunctions of H reads

$$|\Psi^{\text{HF}}\rangle = \sum_i c_i |\Psi_i\rangle \quad (5.78)$$

$$|e^{\mathbf{T}}\Psi^{\text{HF}}\rangle = \sum_j d_j |\Psi_j\rangle. \quad (5.79)$$

Inserting Eqs. (5.78) and (5.79) into Eq. (5.76) yields

$$\begin{aligned} E &= \sum_{ij} c_i^* d_j \langle \Psi_i | H | \Psi_j \rangle \\ &= \sum_i c_i^* d_i \epsilon_i. \end{aligned} \quad (5.80)$$

Note that $c_i \neq d_i$, because $|\Psi^{\text{HF}}\rangle \neq |e^{\mathbf{T}}\Psi^{\text{HF}}\rangle$. Subtracting E_{exact} from both sides of Eq. (5.80) yields

$$E - E_{\text{exact}} = \sum_i c_i^* d_i \epsilon_i - E_{\text{exact}}. \quad (5.81)$$

Since E_{exact} corresponds to the ground state energy of H , all eigenvalues, ϵ_i , of H fulfill

$$\epsilon_i \geq E_{\text{exact}}. \quad (5.82)$$

Since $c_i^* d_i$ can be negative, $(E - E_{\text{exact}})$ might be negative as well. Hence, the total MP2 and CCSD energies can be lower than E_{exact} .

5.4 The correlation energy in the random phase approximation

The random phase approximation (RPA) to the correlation energy dates back to the late fifties and was introduced in solid state physics by Nozières and Pines [23]. A particular promising feature of the RPA is that all bonding situations are described reasonably well: ionic, covalent, metallic, and even van der Waals bonding [24]. This stands in contrast to perturbation theory, such as Møller-Plesset perturbation theory (MP_n), which diverges to any order n in metallic systems. In fact, one motivation for introducing the RPA was that the resummation of certain diagrams removes the divergence of the perturbation series.

For the calculation of total energies, the RPA was largely disregarded, and instead the focus has been on Kohn-Sham methods [2], which are computationally less complex. However, the standstill in the development of new functionals and the tremendous advances in computer power have recently brought the RPA back to general attention. This revival was first realized in *GW* quasiparticle methods [25], which usually implicitly rely on the RPA [26, 27], but total energies moved into focus only shortly afterwards [28, 29].

The RPA correlation energy can be derived in different ways, for instance from many-electron Green's function theory [30], or using the adiabatic-connection fluctuation-dissipation theorem (ACFDT) [31, 32], or from coupled-cluster theory [33, 34]. In the following sections, we derive the RPA correlation energy from the ACFDT and outline its connection to Casida's equation and coupled-cluster theory.

5.4.1 The adiabatic-connection fluctuation dissipation theorem

Sections 5.1 and 5.2 discussed correlated methods that use an explicit ansatz for the many-electron wave function and are based on perturbation- and coupled-cluster theory, respectively. The adiabatic-connection fluctuation dissipation theorem (ACFDT) provides an alternative method to calculate the correlation energy without the knowledge of the many-electron wave function. The ACFDT yields in principle an exact expression for the Hartree-exchange-

correlation energy ($E_{ee} + E_{Hxc}$) [see Eq. (3.1)]. The derivation of the Hartree-exchange-correlation energy expression in the ACFDT along the lines of Ref. [36] is briefly sketched below.

The adiabatic-connection

In the adiabatic connection one considers a Hamiltonian with a coupling constant α that gradually increases the electron-electron Coulomb interaction, \hat{V}_{ee} , from 0 (KS system) to 1 (fully-interacting system):

$$\hat{H}(\alpha) = \hat{T} + \hat{V}(\alpha) + \alpha\hat{V}_{ee}. \quad (5.83)$$

\hat{T} and $\hat{V}(\alpha)$ denote the kinetic energy operator and the KS potential, respectively. $\hat{V}(\alpha)$ is chosen such that the ground state density and energy of the α -interacting system are equal to the exact many-body density and energy (i.e. the fully-interacting system).

The exact energy, E , for $\alpha = 1$ and $\alpha = 0$ is given by

$$E = \langle \Psi(1) | \hat{H}(1) | \Psi(1) \rangle = \langle \Psi(1) | \hat{T} + \hat{V}_{ee} + \hat{V}(1) | \Psi(1) \rangle = \langle \Psi(1) | \hat{T} + \hat{V}_{ee} | \Psi(1) \rangle + E_{\text{ext}} \quad (5.84)$$

and

$$E = \langle \Psi(0) | \hat{H}(0) | \Psi(0) \rangle = \langle \Psi(0) | \hat{T} + \hat{V}(0) | \Psi(0) \rangle = T_n + E_{\text{H}} + E_{\text{ext}} + E_{xc}, \quad (5.85)$$

respectively. In the above equation E_{H} and T_n refer to the Hartree- and kinetic energy of the KS system, respectively. E_{ext} corresponds to the nuclear-nuclear and nuclear-electron interaction energy. By virtue of Eqs. (5.84) and (5.85), one finds that (see Ref. [36] for details)

$$\begin{aligned} E_{\text{H}} + E_{xc} &= E - E_{\text{ext}} - T_n \\ &= \langle \Psi(1) | \hat{H}(1) | \Psi(1) \rangle - \langle \Psi(1) | \hat{V}(1) | \Psi(1) \rangle - \langle \Psi(0) | \hat{H}(0) | \Psi(0) \rangle + \langle \Psi(0) | \hat{V}(0) | \Psi(0) \rangle \\ &= \int_0^1 d\alpha \frac{d}{d\alpha} \left(\langle \Psi(\alpha) | \hat{H}(\alpha) | \Psi(\alpha) \rangle - \langle \Psi(\alpha) | \hat{V}(\alpha) | \Psi(\alpha) \rangle \right). \end{aligned} \quad (5.86)$$

The Hellmann-Feynman theorem allows to rearrange the above equation to read

$$E_{\text{H}} + E_{xc} = \int_0^1 d\alpha \langle \Psi(\alpha) | \hat{V}_{ee} | \Psi(\alpha) \rangle, \quad (5.87)$$

i.e. there is no reference to the kinetic energy operator anymore.

The fluctuation dissipation theorem

Since \hat{V}_{ee} in Eq. (5.87) is a two-electron operator, $E_H + E_{xc}$ can be calculated from the pair-probability density. As such, Eq. (5.87) becomes

$$E_H + E_{xc} = \int_0^1 d\alpha \langle \Psi(\alpha) | \hat{V}_{ee} | \Psi(\alpha) \rangle = \int_0^1 d\alpha \frac{e^2}{2} \int d^3\mathbf{r} \int d^3\mathbf{r}' \frac{n^{2,\alpha}(\mathbf{r}, \mathbf{r}')}{|\mathbf{r} - \mathbf{r}'|}. \quad (5.88)$$

Furthermore the following relation holds for the pair-probability density [37]

$$n^{2,\alpha}(\mathbf{r}, \mathbf{r}') = \langle \Psi(\alpha) | \delta\hat{n}(\mathbf{r})\delta\hat{n}(\mathbf{r}') | \Psi(\alpha) \rangle + n(\mathbf{r})n(\mathbf{r}') + \delta(\mathbf{r} - \mathbf{r}')n(\mathbf{r}), \quad (5.89)$$

where $\delta\hat{n}(\mathbf{r})$ corresponds to the density fluctuation operator, defined as

$$\delta\hat{n}(\mathbf{r}) = \hat{n}(\mathbf{r}) - n(\mathbf{r}) = \sum_{i=1}^N \delta(\mathbf{r} - \mathbf{r}_i) - n(\mathbf{r}). \quad (5.90)$$

The fluctuation-dissipation theorem, first derived in Ref. [38], allows to relate the density fluctuation operator to the density-density response function, χ_α , according to [39, 32, 37]

$$- \int_0^\infty \frac{d\omega}{\pi} \chi_\alpha(\mathbf{r}, \mathbf{r}'; i\omega) = n^{2,\alpha}(\mathbf{r}, \mathbf{r}') - n(\mathbf{r})n(\mathbf{r}') + \delta(\mathbf{r} - \mathbf{r}')n(\mathbf{r}). \quad (5.91)$$

Solving the above equation for $n^{2,\alpha}(\mathbf{r}, \mathbf{r}')$ and inserting the result into Eq. (5.88) yields

$$E_H + E_{xc} = E_H - \frac{e^2}{2} \int_0^1 d\alpha \int d\omega \int \int d^3\mathbf{r} d^3\mathbf{r}' \left(\frac{1}{\pi} \frac{\chi_\alpha(\mathbf{r}, \mathbf{r}'; i\omega)}{|\mathbf{r} - \mathbf{r}'|} + \frac{\delta(\mathbf{r} - \mathbf{r}')n(\mathbf{r})}{|\mathbf{r} - \mathbf{r}'|} \right). \quad (5.92)$$

In the above equation, χ_α denotes the density-density response function (or particle polarizability) of the system with interaction strength α and is given by the Dyson-like equation [40]

$$\chi_\alpha = \chi_0(\mathbf{r}, \mathbf{r}', \omega) + \int d\mathbf{r}'' \int d\mathbf{r}''' \chi_0(\mathbf{r}, \mathbf{r}'', \omega) [\alpha\nu(\mathbf{r}'', \mathbf{r}''') + f_{xc}^\alpha(\mathbf{r}'', \mathbf{r}''', \omega)] \chi_\alpha(\mathbf{r}''', \mathbf{r}', \omega), \quad (5.93)$$

where χ_0 is the response function of the reference (KS) system [40]

$$\chi_0(\mathbf{r}, \mathbf{r}', \omega) = - \sum_i^{\text{occ.}} \sum_a^{\text{unocc.}} 2 \left(\frac{\psi_a^*(\mathbf{r}')\psi_i(\mathbf{r}')\psi_i^*(\mathbf{r})\psi_a(\mathbf{r})}{\epsilon_a - \epsilon_i - \omega - i\eta} + \frac{\psi_i^*(\mathbf{r}')\psi_a(\mathbf{r}')\psi_a^*(\mathbf{r})\psi_i(\mathbf{r})}{\epsilon_a - \epsilon_i + \omega + i\eta} \right). \quad (5.94)$$

In the above, $i\eta$ introduces an infinitesimal shift along the imaginary axis and ν denotes the Coulomb kernel $\frac{e^2}{|\mathbf{r}-\mathbf{r}'|}$. Equation (5.93) is a Dyson-like equation that links the response function of the α -interacting system, χ_α to the response function of the KS system, χ_0 . ψ_n and ϵ_n denote Kohn-Sham orbitals and orbitalenergies, respectively. f_{xc}^α is the exchange-correlation kernel of the system with interaction strength α .

We now return to Eq. (5.92). It is shown in Ref. [36] that the last term on the right-hand side of Eq. (5.92) can be expressed by the exchange energy, E_X , and χ_0 such that

$$E_H + E_{xc} = E_H + E_X + E_C^{\text{ACFDT}}, \quad (5.95)$$

where

$$E_X = -\frac{e^2}{2} \int d^3\mathbf{r} \int d^3\mathbf{r}' \frac{|\sum_i^{\text{occ.}} \psi_i^*(\mathbf{r})\psi_i(\mathbf{r}')|}{|\mathbf{r}-\mathbf{r}'|} \text{ and} \quad (5.96)$$

$$E_C^{\text{ACFDT}} = \frac{1}{2} \int_0^1 d\alpha \int_0^\infty \frac{d\omega}{\pi} \int d\mathbf{x}_1 d\mathbf{x}_2 \frac{\chi_\alpha(\mathbf{x}_1, \mathbf{x}_2, \omega) - \chi_0(\mathbf{x}_1, \mathbf{x}_2, \omega)}{|\mathbf{x}_1 - \mathbf{x}_2|}. \quad (5.97)$$

The remarkable result of the ACFDT is that the correlation energy can be expressed only by the response function of the KS and α -interacting system. At this point we emphasize an important aspect of the ACFDT: the exchange energy is evaluated *using KS orbitals* and, as such, differs from the self-consistent Hartree-Fock exchange energy. In the field of quantum chemistry, however, the correlation energy is defined as the difference between the self-consistent Hartree-Fock energy and the exact ground state energy. As a consequence, the correlation energy in the ACFDT differs from the definition of the correlation energy in the field of quantum chemistry.

Equations (5.95), (5.94) and (5.93) allow to determine $(E_X + E_C^{\text{ACFDT}})$ exactly in principle. However, the exact form of f_{xc}^α is not known. As such, we have to rely on approximations for f_{xc}^α and χ_α .

In the random phase approximation (RPA), the exchange-correlation kernel f_{xc}^α in Eq. (5.93) is simply neglected. Therefore the response function in the RPA reads

$$\chi_\alpha^{\text{RPA}}(\mathbf{r}, \mathbf{r}', \omega) = \chi_0(\mathbf{r}, \mathbf{r}', \omega) + \alpha \int d\mathbf{r}'' \int d\mathbf{r}''' \chi_0(\mathbf{r}, \mathbf{r}'', \omega) \nu(\mathbf{r}'', \mathbf{r}''') \chi_\alpha^{\text{RPA}}(\mathbf{r}''', \mathbf{r}', \omega). \quad (5.98)$$

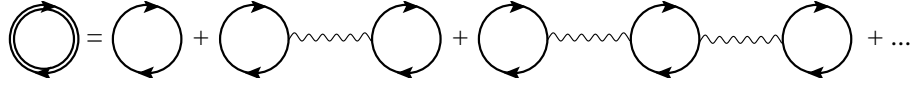


Figure 5.3: The bubble diagrams on the right-hand side correspond to χ_0 . The dressed bubble diagram on the left-hand side denotes χ_α^{RPA} . Wiggly lines represent the unscreened Coulomb interaction ν .

It is known from *GW*-RPA calculations that from a practical point of view the RPA is well justified and yields reasonably accurate polarizabilities compared to experiment if *Kohn-Sham eigenvalues and orbitals* are used in Eq. (5.94). [41]

In passing we note that the above Eq. (5.98) can also be arranged to read

$$\chi_\alpha^{\text{RPA}^{-1}}(\omega) = \chi_0^{-1}(\omega) - \alpha\nu. \quad (5.99)$$

Equation (5.99) is also referred to as an inverse Dyson-like equation.

Equation (5.98) can be solved recursively by inserting the expression from the left-hand side into the right-hand side yielding

$$\chi_\alpha^{\text{RPA}} = \chi_0 + \alpha\chi_0\nu\chi_0 + \alpha^2\chi_0\nu\chi_0\nu\chi_0 + \dots \quad (5.100)$$

The above equation corresponds, in a diagrammatic language, to a resummation of infinitely many so-called bubble diagrams [see Fig. 5.3].

Inserting Eqs. (5.94) and (5.98) into Eq. (5.97) allows for integrating over the coupling constant α analytically [see Eq. (3.34) in Ref. [36]] and yields a closed expression for the RPA correlation energy that reads

$$E_c^{\text{RPA}} = \int_0^\infty \frac{d\omega}{2\pi} \text{Tr} \{ \ln(1 + \chi_0\nu) - \chi_0\nu \}. \quad (5.101)$$

5.4.2 ACFDT-RPA from time-dependent density functional theory

In this section an alternative approach to calculate E_c^{RPA} will be outlined. In Eqs. (5.97) and (5.101), an integration over ω is carried out explicitly. One might replace the integration by a summation over the residues at the poles of χ . The independent particle response function, χ_0 , [defined in Eq. (5.94)] exhibits poles in ω at the single-particle excitation energies ($\epsilon_a - \epsilon_i$). The poles

of χ_α need to be determined. To calculate the poles of χ_α^{RPA} , we introduce the density matrix response function [42]

$$\Xi_\alpha(\mathbf{r}_1, \mathbf{r}'_1, \mathbf{r}_2, \mathbf{r}'_2, \omega) = -\langle(\mathbf{r}_1 \mathbf{r}'_1)|(\Lambda_\alpha - \omega \Delta)^{-1}|(\mathbf{r}_2 \mathbf{r}'_2)\rangle, \quad (5.102)$$

where

$$\Delta = \begin{pmatrix} 1 & 0 \\ 0 & -1 \end{pmatrix} \text{ and } \Lambda_\alpha = \begin{pmatrix} A^\alpha & B^\alpha \\ B^{\alpha*} & A^{\alpha*} \end{pmatrix}. \quad (5.103)$$

A^α and B^α are in the RPA given by

$$A_{(ia,jb)}^\alpha = \delta_{ij} \delta_{ab} (\epsilon_a - \epsilon_i) + \alpha \langle ij|ab \rangle \quad (5.104)$$

$$B_{(ia,jb)}^\alpha = \alpha \langle ij|ab \rangle. \quad (5.105)$$

In the above equations i, j and a, b refer to occupied and unoccupied spin-orbitals, respectively. The density matrix response function $(\Lambda_\alpha - \omega \Delta)^{-1}$ is given in an orbital basis and split into a resonant and anti resonant part (first and second line of Δ). The resonant and anti resonant parts exhibit poles at positive and negative frequencies ω , respectively loosely corresponding to the first and second term in Eq. (5.94), respectively. Ξ_α is defined such that the diagonal elements in real space correspond to the (independent) particle polarizability [42]

$$\chi_\alpha^{\text{RPA}}(\mathbf{r}_1, \mathbf{r}_2, \omega) = -\langle(\mathbf{r}_1 \mathbf{r}_1)|(\Lambda_\alpha - \omega \Delta)^{-1}|(\mathbf{r}_2 \mathbf{r}_2)\rangle. \quad (5.106)$$

The projection from orbital into real space ($\langle(\mathbf{r}_1 \mathbf{r}_1)|$ and $|(\mathbf{r}_2 \mathbf{r}_2)\rangle$) contains the summation of the resonant and anti resonant part. As such we find for $\Xi_{\alpha=0}$

$$\begin{aligned} -\langle(\mathbf{r}_1 \mathbf{r}_1)|(\Lambda_0 - \omega \Delta)^{-1}|(\mathbf{r}_2 \mathbf{r}_2)\rangle &= \sum_{ij} \sum_{ab} \psi_i^*(\mathbf{r}_1) \psi_a(\mathbf{r}_1) (A^0 - \omega)_{(ia,jb)}^{-1} \psi_j(\mathbf{r}_2) \psi_b^*(\mathbf{r}_2) \\ &\quad + \sum_{ij} \sum_{ab} \psi_i^*(\mathbf{r}_1) \psi_a(\mathbf{r}_1) (A^0 + \omega)_{(ia,jb)}^{-1} \psi_j(\mathbf{r}_2) \psi_b^*(\mathbf{r}_2) \end{aligned} \quad (5.107)$$

$$= \chi_0(\mathbf{r}_1, \mathbf{r}_2, \omega). \text{ since} \quad (5.108)$$

$$(A^0 - \omega)_{(ia,jb)}^{-1} = \delta_{ij} \delta_{ab} \frac{1}{\epsilon_a - \epsilon_i - \omega}. \quad (5.109)$$

5.4 The correlation energy in the random phase approximation 37

Replacing $\chi_\alpha^{\text{RPA}^{-1}} \rightarrow -(\Lambda_\alpha - \omega\Delta)$ and $\alpha\nu \rightarrow \begin{pmatrix} B^\alpha & B^\alpha \\ B^{\alpha*} & B^{\alpha*} \end{pmatrix}$, the inverse Dyson-like equation (5.99) in the orbital basis becomes

$$\underbrace{- \left[\begin{pmatrix} A^{\alpha=0} & 0 \\ 0 & A^{\alpha=0} \end{pmatrix} - \omega \begin{pmatrix} 1 & 0 \\ 0 & -1 \end{pmatrix} \right]}_{\chi_0^{-1}(\omega)} - \underbrace{\begin{pmatrix} B^\alpha & B^\alpha \\ B^{\alpha*} & B^{\alpha*} \end{pmatrix}}_{\alpha\nu} = \underbrace{-(\Lambda_\alpha - \omega\Delta)}_{\chi_\alpha^{\text{RPA}^{-1}}(\omega)} \quad (5.110)$$

Subtracting $\omega\Delta$ from both sides of the above equation gives

$$\begin{pmatrix} A^{\alpha=0} & 0 \\ 0 & A^{\alpha=0*} \end{pmatrix} + \begin{pmatrix} B^\alpha & B^\alpha \\ B^{\alpha*} & B^{\alpha*} \end{pmatrix} = \begin{pmatrix} A^\alpha & B^\alpha \\ B^{\alpha*} & A^{\alpha*} \end{pmatrix} = \Lambda_\alpha \quad (5.111)$$

Replacing Λ_α in the above equation by its spectral representation with eigenvectors $|X_i^\alpha, Y_i^\alpha\rangle$ that are orthonormalized according to [42]

$$\langle X_n^\alpha, Y_n^\alpha | \Delta | X_n^\alpha, Y_n^\alpha \rangle = 1, \quad (5.112)$$

yields

$$\begin{pmatrix} A^\alpha & B^\alpha \\ B^{\alpha*} & A^{\alpha*} \end{pmatrix} = \sum_i \omega_i \Delta |X_i^\alpha, Y_i^\alpha\rangle \langle X_i^\alpha, Y_i^\alpha | \Delta. \quad (5.113)$$

Multiplication from right with $|X_n^\alpha, Y_n^\alpha\rangle$ yields the so-called Casida equation [43]

$$\begin{pmatrix} A^\alpha & B^\alpha \\ B^{\alpha*} & A^{\alpha*} \end{pmatrix} \begin{pmatrix} X_n^\alpha \\ Y_n^\alpha \end{pmatrix} = \omega_n^\alpha \begin{pmatrix} 1 & 0 \\ 0 & -1 \end{pmatrix} \begin{pmatrix} X_n^\alpha \\ Y_n^\alpha \end{pmatrix}, \quad (5.114)$$

where n labels the eigenstates and poles of the response function and corresponds to the number of product states (*ia*). ω_n^α corresponds to the poles of χ_α^{RPA} . Equation (5.114) generalizes the Dyson-like equation and is widely used in time-dependent Hartree-Fock (TDHF) and time-dependent density functional theory (TDDFT) to calculate excitation energies and transition properties [44]. The eigenvectors $|X_n^\alpha, Y_n^\alpha\rangle$ and the corresponding eigenvalues ω_n^α fulfill Eq. (5.114) and allow to rewrite the response function in its spectral representation [44]

$$\chi_\alpha^{\text{RPA}}(\mathbf{r}_1, \mathbf{r}_2, \omega) = - \sum_n \left(\frac{\rho_n^\alpha(\mathbf{r}_1) \rho_n^{\alpha*}(\mathbf{r}_2)}{\omega_n^\alpha - \omega - i\eta} + \frac{\rho_n^\alpha(\mathbf{r}_1) \rho_n^{\alpha*}(\mathbf{r}_2)}{\omega_n^\alpha + \omega + i\eta} \right), \quad (5.115)$$

where

$$\rho_n^\alpha(\mathbf{r}) = \sum_{jb} (X_{n,jb}^\alpha + Y_{n,jb}^\alpha) \psi_j^*(\mathbf{r}) \psi_b(\mathbf{r}). \quad (5.116)$$

Inserting Eq. (5.115) into Eq. (5.97) yields the RPA correlation energy *without frequency integration*: [44]

$$E_C^{\text{RPA}} = \frac{1}{2} \int_0^\infty d\alpha \sum_n \iint d\mathbf{r}_1 d\mathbf{r}_2 \frac{\rho_n^\alpha(\mathbf{r}_1) \rho_n^{\alpha*}(\mathbf{r}_2) - \rho_n^{\alpha=0}(\mathbf{r}_1) \rho_n^{\alpha=0*}(\mathbf{r}_2)}{|\mathbf{r}_1 - \mathbf{r}_2|}. \quad (5.117)$$

In the following we will carry out the α integration in Eq. (5.117) analytically along the lines of Ref. [44]. Furche showed in Ref. [44] that

$$\frac{d\omega_n^\alpha}{d\alpha} = \langle X_n^\alpha, Y_n^\alpha | \frac{d\Lambda_\alpha}{d\alpha} | X_n^\alpha, Y_n^\alpha \rangle. \quad (5.118)$$

By virtue of Eq. (5.111), we find that

$$\frac{d\Lambda_\alpha}{d\alpha} = \begin{pmatrix} C & C \\ C^* & C^* \end{pmatrix}, \quad (5.119)$$

where $C = \langle ij|ab \rangle$. Thus,

$$\frac{d\omega_n^\alpha}{d\alpha} = \sum_{ij} \sum_{ab} (X_n^\alpha + Y_n^\alpha)_{ia}^* \langle ij|ab \rangle (X_n^\alpha + Y_n^\alpha)_{jb} = \iint d\mathbf{r}_1 d\mathbf{r}_2 \frac{\rho_n^\alpha(\mathbf{r}_1) \rho_n^{\alpha*}(\mathbf{r}_2)}{|\mathbf{r}_1 - \mathbf{r}_2|}. \quad (5.120)$$

Inserting the above equation into Eq. (5.117) allows to integrate over α and yields [44]

$$E_C^{\text{RPA}} = \frac{1}{2} \int d\alpha \sum_n \left(\frac{d\omega_n^\alpha}{d\alpha} - \frac{d\omega_n^\alpha}{d\alpha} \Big|_{\alpha=0} \right) = \frac{1}{2} \sum_n (\omega_n - \omega_n^D), \quad (5.121)$$

where ω_n corresponds to the poles of $\chi_{\alpha=1}^{\text{RPA}}$ and ω_n^D is the sum of zero- and first-order RPA excitation energies given by [44]

$$\omega_n^D = \epsilon_a - \epsilon_i + \iint d\mathbf{x}_1 d\mathbf{x}_2 \frac{\rho_n^{\alpha=0}(\mathbf{x}_1) \rho_n^{\alpha=0}(\mathbf{x}_2)}{|\mathbf{x}_1 - \mathbf{x}_2|} = \epsilon_a - \epsilon_i + \langle ii|aa \rangle. \quad (5.122)$$

5.4.3 The RPA in coupled-cluster theory

The results of the previous section allow to outline the connection between the Casida equation and coupled-cluster doubles theory in the RPA (as discussed in Ref. [34]). Casida's equation [see Eq. (5.114)] might be multiplied from the left by Δ to read

$$\begin{pmatrix} A & B \\ -B^* & -A^* \end{pmatrix} \begin{pmatrix} X \\ Y \end{pmatrix} = \omega^{\alpha=1} \begin{pmatrix} X \\ Y \end{pmatrix}. \quad (5.123)$$

5.4 The correlation energy in the random phase approximation 39

Multiplying the above equation [see Eq. (5.114)] for $\alpha = 1$ on the right by X^{-1} gives

$$\begin{pmatrix} A & B \\ -B^* & -A^* \end{pmatrix} \begin{pmatrix} 1 \\ T \end{pmatrix} = \omega^{\alpha=1} \begin{pmatrix} 1 \\ T \end{pmatrix}, \quad (5.124)$$

where $T = YX^{-1}$. Multiplying Eq. (5.124) on the left by $\begin{pmatrix} T & -1 \end{pmatrix}$ yields

$$\begin{pmatrix} T & -1 \end{pmatrix} \begin{pmatrix} A & B \\ -B^* & -A^* \end{pmatrix} \begin{pmatrix} 1 \\ T \end{pmatrix} = \begin{pmatrix} T & -1 \end{pmatrix} \omega^{\alpha=1} \begin{pmatrix} 1 \\ T \end{pmatrix}. \quad (5.125)$$

Carrying out the matrix multiplications in the above equation leads to

$$B^* + A^*T + TA + TBT = 0. \quad (5.126)$$

This is the quadratic Riccati equation, which is equivalent to the original matrix diagonalization problem stated in Eq. (5.114). The remarkable point is that this equation has only half of the dimension of the original eigenvalue problem, but since the equation is non-linear (quadratic) its solution can be only determined by iteration. Furthermore, it is not obvious how to calculate X and Y from T , but remarkably the correlation energy can be readily calculated, as demonstrated below. Inserting Eqs. (5.104) and (5.105) into Eq. (5.126) yields

$$\begin{aligned} 0 &= \langle ab|ij \rangle + t_{ij}^{ab}(\epsilon_a + \epsilon_b - \epsilon_i - \epsilon_j) \\ &\quad + \sum_k^{\text{occ.}} \sum_c^{\text{unocc.}} (\langle ic|ak \rangle t_{kj}^{cb} + t_{ik}^{ac} \langle cj|kb \rangle) \\ &\quad + \sum_{kl}^{\text{occ.}} \sum_{cd}^{\text{unocc.}} t_{ik}^{ac} \langle kl|cd \rangle t_{lj}^{db}. \end{aligned} \quad (5.127)$$

The above equation is in fact a simplified version of the coupled-cluster amplitude equations that are given in Sec. 5.2. As such, we find that the eigenvectors X and Y of Casida's equation allow to calculate amplitudes T ($= YX^{-1}$) that are solutions of the coupled-cluster doubles amplitude equations in the random phase approximation. In a full CCD calculation, the amplitude equations are significantly more complicated involving, e.g. particle-particle diagrams, hole-hole and particle-hole ladder diagrams [see Fig. 5.2, respectively].

In coupled-cluster doubles theory the correlation energy is calculated from the amplitudes as

$$E_C^{\text{CCD}} = \sum_{ijab} \frac{1}{2} \langle ij||ab \rangle t_{ij}^{ab}, \quad (5.128)$$

Replacing $\langle ij||ab \rangle$ by $\langle ij|ab \rangle$ yields

$$\sum_{ijab} \frac{1}{2} \langle ij|ab \rangle t_{ij}^{ab} = \frac{1}{2} \text{Tr}(BT). \quad (5.129)$$

From the first line in Eq. (5.124) we know that

$$\text{Tr}(BT) = \text{Tr}(\omega - A). \quad (5.130)$$

Inserting Eq. (5.130) into the right-hand side of Eq. (5.129) yields

$$\sum_{ijab} \frac{1}{2} \langle ij|ab \rangle t_{ij}^{ab} = \frac{1}{2} \text{Tr}(BT) = \frac{1}{2} \text{Tr}(\omega - A) = \frac{1}{2} \sum_n (\omega_n - \epsilon_a + \epsilon_i - \langle ii|aa \rangle). \quad (5.131)$$

As such, the expression for the ACFDT-RPA correlation energy corresponds to the coupled-cluster doubles energy expression for $\langle ij||ab \rangle \rightarrow \langle ij|ab \rangle$ with amplitudes that were calculated from a simplified version of the amplitude equations [see Eq. (5.127)].

The RPA is only correct to first-order perturbation theory, but like CCSD performs a resummation of diagrams of a certain type (bubble diagrams) to infinite order.

5.5 Beyond RPA: Second-order screened exchange

The RPA accounts for the direct correlation from symmetric Coulomb terms (“Hartree-like”) only. As a result, one finds that the correlation energy of a one-electron system is not vanishing in the RPA. Instead the RPA yields (for a one-electron system with an occupied orbital i)

$$E_C^{\text{RPA}} = \sum_{ab} \frac{1}{2} \langle ii|ab \rangle t_{ii}^{ab} \neq 0. \quad (5.132)$$

This error is also referred to as *self-correlation*. MP2 and CCD do not suffer from self-correlation errors for one-electron systems due to the inclusion of exchange-like terms in the energy expression [see Eq. (5.34)]. The exchange-like term cancels exactly with the direct term for one-electron systems:

$$\sum_{ab} \frac{1}{2} \langle ii||ab \rangle t_{ii}^{ab} = \sum_{ab} \frac{1}{2} \underbrace{(\langle ii||ab \rangle - \langle ii|ba \rangle)}_{=0} t_{ii}^{ab}. \quad (5.133)$$

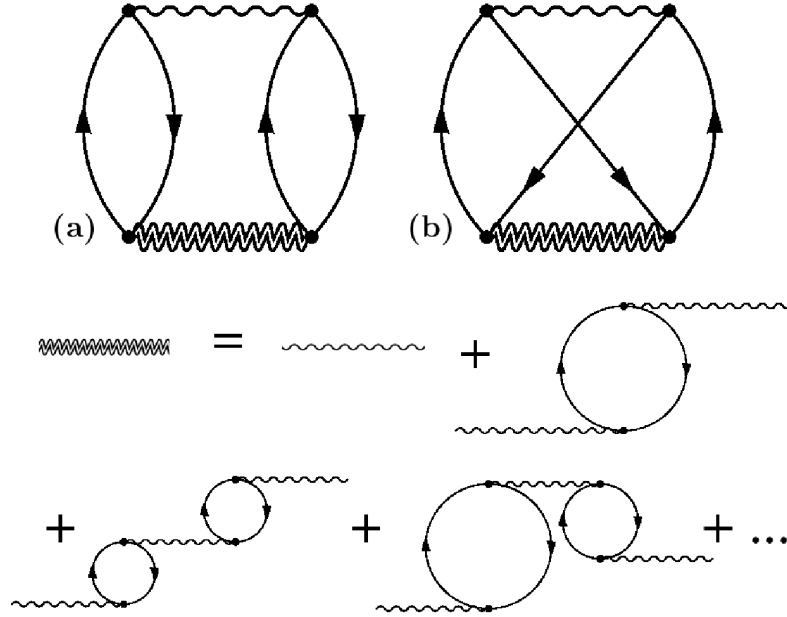


Figure 5.4: Diagrams corresponding to (a) direct-RPA correlation and (b) second-order screened exchange (SOSEX). The wiggly and double wiggly line represent the unscreened and screened Coulomb interaction, respectively.

We now define the RPA+second-order screened exchange (SOSEX) correlation energy as (see Fig. 5.4)

$$E_C^{\text{RPA+SOSEX}} = \sum_{ijab} \frac{1}{2} \langle ij|ab \rangle t_{ij}^{ab} - \sum_{ijab} \frac{1}{2} \langle ij|ba \rangle t_{ij}^{ab}, \quad (5.134)$$

i.e. suggest to use the “original” CCD correlation energy as defined in Eq. (5.128). The first term in Eq. (5.134) corresponds to the RPA correlation energy. The exchange-like second term in Eq. (5.134) is related to the anti-symmetry of the many-electron wave function and approximately accounts for correlation from the “exchange” (SOSEX). We want to improve upon the RPA [see Fig. 5.4(a)] by including an exchange-like correlation term that is fully compatible with the direct Coulomb correlation accounted for by the RPA, where compatibility here implies that for one-electron systems, the self-correlation error exactly vanishes. Furthermore, RPA+SOSEX is correct to second order (equivalent to MP2), whereas RPA is only correct to first order.

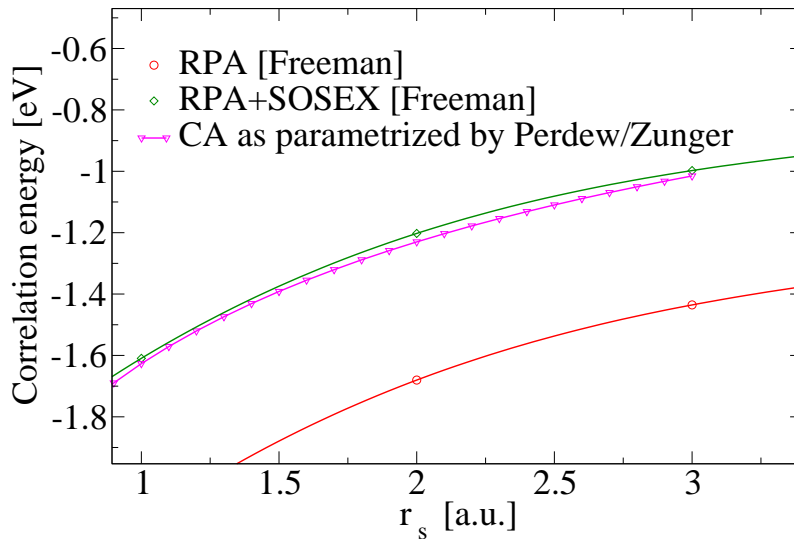


Figure 5.5: RPA, RPA+SOSEX and exact correlation energies of the homogeneous electron gas as a function of the Wigner Seitz radius, r_s . The exact values correspond to quantum Monte Carlo results as parameterized by Perdew and Zunger [3]

In a full CCD calculation, the total energy expression in Eq. (5.134) remains unchanged, but the evaluation of the amplitudes is significantly more complicated involving, e.g. particle-particle diagrams, hole-hole and particle-hole ladder diagrams [see Fig. 5.2, respectively]. Furthermore, usually also singly excited determinants, in which one occupied orbital is replaced by a virtual orbital, are included (CCSD). Our assumption is twofold. (i) First, we assume that the contributions from the singles in the total energy expression are small such that one can neglect them. (ii) Second, we assume that the amplitudes t_{ij}^{ab} evaluated using Kohn-Sham orbitals and the direct-ring approximation [Eq. (5.127)], resemble in some way the amplitudes of CCSD using HF orbitals. These conjectures imply that the Coulomb *and exchange-like correlation terms* in Eq. (5.134) should give a good estimate for the total correlation energy. This approximation to the correlation energy is in no way new and has been suggested by Monkhorst [47] and Freeman [33] in the late seventies, but largely disregarded or forgotten afterwards. Freeman evaluated the correlation energy of the homogeneous electron gas (HEG) using the

RPA and RPA+SOSEX on top of KS orbitals and eigenvalues before the exact quantum Monte Carlo results by Ceperley and Alder were published in Ref. [3]. Figure 5.5 shows that the RPA+SOSEX correlation energies for the HEG agree very well with the exact Monte Carlo results, whereas the RPA exhibits a strong overestimation of the correlation energy that is attributed to self-correlation.

We note that it is difficult to motivate the RPA+SOSEX approximation in the framework of ACFDT, where SOSEX would have to correspond to an approximation of f_{xc}^α , but in Green's function theory, this particular subset of diagrams is equivalent to vertex corrections in the self-energy only, disregarding vertex corrections in the polarizability (i.e. electrostatic particle-hole interactions) [48].

The computational effort of our RPA+SOSEX implementation scales as $\mathcal{O}(N^5)$, where N is a measure of the system size. This is achieved by the introduction of intermediate quantities in Eq. (5.127). For further details on the implementation of the RPA+SOSEX method in VASP and the intermediate quantities, the reader is referred to Sec. 8.3 and Appendix D.

5.6 The direct MP2 correlation energy

In this section, we outline a scheme to evaluate the “direct” contributions in second-order Møller-Plesset perturbation theory using the response function. In the ACFDT we may write the following expression for the correlation energy (see Eq. (5.97)),

$$E_c = - \int_0^1 d\alpha \int_0^\infty \frac{d\omega}{2\pi} \text{Tr}\{\nu[\chi^\alpha(i\omega) - \chi^0(i\omega)]\}. \quad (5.135)$$

Evaluating the above in reciprocal space, the trace is defined as

$$\text{Tr}\{AB\} := \sum_{\mathbf{G}\mathbf{G}'} A_{\mathbf{G}\mathbf{G}'}(\mathbf{q}) B_{\mathbf{G}'\mathbf{G}}. \quad (5.136)$$

The summation over \mathbf{G} and \mathbf{G}' includes all reciprocal lattice vectors with $|\mathbf{G}|^2$ and $|\mathbf{G}'|^2$, below a kinetic energy cutoff E_χ [see remarks following Eqs. (8.37) and (8.38)].

The Coulomb kernel ν in reciprocal space is given by $\nu_{\mathbf{G}\mathbf{G}'} = 4\pi e^2 \delta_{\mathbf{G}\mathbf{G}'} / |\mathbf{G}|^2$ and the independent-particle response function at imaginary frequencies $\chi^0(i\omega)$

by [compare Eq. (5.94)]

$$\chi_{\mathbf{G}\mathbf{G}'}^0(i\omega) = - \sum_i^{\text{occ.}} \sum_a^{\text{unocc.}} 2 \left(\frac{\langle \psi_a | e^{i(\mathbf{G})\cdot\mathbf{r}} | \psi_i \rangle \langle \psi_i | e^{-i(\mathbf{G}')\cdot\mathbf{r}'} | \psi_a \rangle}{\epsilon_a - \epsilon_i - i\omega} + \frac{\langle \psi_i | e^{i(\mathbf{G})\cdot\mathbf{r}} | \psi_a \rangle \langle \psi_a | e^{-i(\mathbf{G}')\cdot\mathbf{r}'} | \psi_i \rangle}{\epsilon_a - \epsilon_i + i\omega} \right). \quad (5.137)$$

where the sum over i and a may be restricted to run over occupied and virtual orbitals, respectively.

Expanding the interacting response function χ^α up to first order in α (or equivalently, up to second order in χ^0) one obtains [compare Eq. (5.100)]

$$\chi^\alpha(i\omega) = \chi^0(i\omega) + \chi^0(i\omega)\alpha\nu\chi^0(i\omega), \quad (5.138)$$

and

$$E_c = -\frac{1}{2} \int_0^\infty \frac{d\omega}{2\pi} \sum_{\mathbf{G}} \frac{4\pi e^2}{|\mathbf{G}|^2} \times \sum_{\mathbf{G}'} \chi_{\mathbf{G}\mathbf{G}'}^0(i\omega) \frac{4\pi e^2}{|\mathbf{G}'|^2} \chi_{\mathbf{G}'\mathbf{G}}^0(i\omega). \quad (5.139)$$

Inserting Eq. (5.137) into the above we obtain

$$E_c = - \sum_{ij}^{\text{occ}} \sum_{ab}^{\text{unocc.}} \frac{2}{\pi} \int_0^\infty \frac{(\epsilon_a - \epsilon_i)}{(\epsilon_a - \epsilon_i)^2 + \omega^2} \frac{(\epsilon_b - \epsilon_j)}{(\epsilon_b - \epsilon_j)^2 + \omega^2} d\omega \times 2 \left[\left(\frac{4\pi e^2}{\Omega} \sum_{\mathbf{G}} \frac{\langle \psi_a | e^{i(\mathbf{G})\cdot\mathbf{r}} | \psi_i \rangle \langle \psi_j | e^{-i(\mathbf{G})\cdot\mathbf{r}'} | \psi_b \rangle}{|\mathbf{G}|^2} \right) \times c.c. \right] \quad (5.140)$$

which yields

$$E_c = - \sum_{ij}^{\text{occ}} \sum_{ab}^{\text{unocc.}} \frac{2|\langle ij|ab\rangle|^2}{\epsilon_a + \epsilon_b - \epsilon_i - \epsilon_j}. \quad (5.141)$$

As mentioned in Sec. 5.1 this is commonly called the “direct” contribution to the MP2 correlation energy [compare Eq. (5.33)]. From the above it is clear that this contribution may be written as

$$D = -\frac{1}{2} \int_0^\infty \frac{d\omega}{2\pi} \text{Tr}\{\nu\chi^0(i\omega)\nu\chi^0(i\omega)\}. \quad (5.142)$$

This expression may be conveniently evaluated as follows. First one constructs the Hermitian matrix:

$$S(i\omega)_{\mathbf{G}\mathbf{G}'} = \nu_{\mathbf{G}\mathbf{G}}^{1/2} \chi_{\mathbf{G}\mathbf{G}'}^0(i\omega) \nu_{\mathbf{G}'\mathbf{G}'}^{1/2}. \quad (5.143)$$

This may be diagonalized with respect to \mathbf{G} and \mathbf{G}' , to yield a set of $N_{\mathbf{G}}$ real eigenvalues $\{\lambda(i\omega)\}$, where $N_{\mathbf{G}}$ is the number of plane waves in the basis set expansion of the response functions. The trace in Eq. (5.142) may then be evaluated as

$$\text{Tr}\{\nu\chi^0(i\omega)\nu\chi^0(i\omega)\} = \sum_n \lambda(i\omega)_n^2. \quad (5.144)$$

The evaluation of the direct MP2 term as outlined above exhibits a computational effort that scales as $\mathcal{O}(N^4)$ only [compared to $\mathcal{O}(N^5)$ for the evaluation of Eq. (5.33)]. The $\mathcal{O}(N^4)$ scaling results from the calculation of $\chi^0(i\omega)$ in Eq. (5.137) and constitutes the computational bottleneck.

5.7 Solving the amplitude equations

The amplitude equations (5.53), (5.54), (5.61),(5.63) and (5.127) can be generalized to read as a quadratic system of equations. In the following we briefly sketch the algorithm that we use for solving the double amplitude equations. The single amplitude equations are solved analogue. For the sake of brevity we write the double amplitude equations as

$$0 = \mathbf{A} + \mathbf{B}\mathbf{T}_2 + \mathcal{O}(\mathbf{T}) + \mathcal{O}(\mathbf{T}^2). \quad (5.145)$$

In the above equation \mathbf{T}_2 denotes t_{ij}^{ab} and \mathbf{T} depends only on $(t_i^a t_j^b)$ and t_{ij}^{ab} . The exact forms of $\mathcal{O}(\mathbf{T})$ and $\mathcal{O}(\mathbf{T}^2)$ are not of importance for the following discussion. Note that the matrix \mathbf{B} is of the size $(N_u^2 N_o^2) \times (N_u^2 N_o^2)$. N_u and N_o are the number of unoccupied and occupied orbitals, respectively. This makes a direct storage and inversion of \mathbf{B} impossible for larger systems. In practice, one attempts to solve Eq. (5.145) by means of the Jacobi method. Equation (5.145) can be written as

$$0 = \mathbf{A} + (\mathbf{B}' - \mathbf{D})\mathbf{T}_2 + \mathcal{O}(\mathbf{T}) + \mathcal{O}(\mathbf{T}^2), \quad (5.146)$$

where

$$\mathbf{B} = \mathbf{B}' - \mathbf{D}, \quad (5.147)$$

and \mathbf{D} is diagonal. Rearranging Eq. (5.146) yields

$$\mathbf{D}\mathbf{T}_2 = \mathbf{A} + \mathbf{B}'\mathbf{T}_2 + \mathcal{O}(\mathbf{T}) + \mathcal{O}(\mathbf{T}^2). \quad (5.148)$$

Since \mathbf{D} is a diagonal matrix it is straightforward to calculate its inverse and multiply Eq. (5.148) from the left with \mathbf{D}^{-1} ,

$$\mathbf{T}_2 = \mathbf{D}^{-1} [\mathbf{A} + \mathbf{B}'\mathbf{T}_2 + \mathcal{O}(\mathbf{T}) + \mathcal{O}(\mathbf{T}^2)]. \quad (5.149)$$

The Jacobi method is an iterative technique that solves Eq. (5.149) by obtaining a new value for \mathbf{T}_2 from the left-hand side, using a previous value for \mathbf{T}_2 on the right-hand side:

$$\mathbf{T}_2^{(n+1)} = \mathbf{D}^{-1} [\mathbf{A} + \mathbf{B}'\mathbf{T}_2^{(n)} + \mathcal{O}(\mathbf{T}^{(n)}) + \mathcal{O}((\mathbf{T}^{(n)})^2)]. \quad (5.150)$$

In our implementation of the CCSD method, the starting guess for $\mathbf{T}_2 = \mathbf{T}_2^{(0)}$ equals zero. Moreover, we choose \mathbf{D} to be the diagonal Fock matrix. As a result, we get in the first iteration

$$\mathbf{T}_2^{(1)} = \mathbf{D}^{-1}\mathbf{A}, \quad (5.151)$$

which equals the MP2 amplitudes in Eq. (5.22) [as one finds after careful inspection of Eq. (5.54)]. The advantage of the Jacobi method is that at most two sets of amplitudes $\mathbf{T}_2^{(n+1)}$ and $\mathbf{T}_2^{(n)}$ (i.e. the new and the previous set) need to be stored at the same time. All other quantities can be calculated on the fly.

Equation (5.150) produces a series of amplitudes $\{\mathbf{T}_2^{(1)}, \mathbf{T}_2^{(2)}, \mathbf{T}_2^{(3)}, \dots, \mathbf{T}_2^{(n)}\}$ that converges if

$$\rho(\mathbf{D}^{-1}\mathbf{B}') < 1. \quad (5.152)$$

In the above equation ρ is the spectral radius of the matrix $\mathbf{D}^{-1}\mathbf{B}'$. The neglect of quadratic terms in Eq. (5.150) is, in general, well justified because they are small and changes the conditioning of the matrix $\mathbf{D}^{-1}\mathbf{B}'$ only little. Convergence difficulties are in practice only observed for systems with a small gap, and strong multireference character (i.e. systems where the Hartree-Fock determinant is not dominant in the configuration space).

Chapter 6

Natural orbitals

Up to this point we have discussed several methods that allow for the treatment of correlation effects at different levels of theory. All wave function based methods, require an unoccupied orbital space that is either calculated from Hartree-Fock or density functional theory. In practice, one observes that the correlation energy converges very slowly with respect to the number of unoccupied HF or DFT orbitals. Therefore the number of unoccupied orbitals is usually orders of magnitude larger than the number of occupied orbitals. The contribution of the unoccupied orbitals to the computational effort in MP2, RPA, RPA+SOSEX and CCSD scales as $\mathcal{O}(N_u^2)$, $\mathcal{O}(N_u^2)$, $\mathcal{O}(N_u^2)$ and $\mathcal{O}(N_u^4)$ (in our implementations), respectively, where N_u is the number of unoccupied orbitals. As such, the highest potential to reduce the computational effort lies in a reduction of the number of unoccupied orbitals. The question arises, whether it is possible to construct a different unoccupied orbital space in which the correlation energy converges more rapidly with respect to the unoccupied orbitals? In fact, it is known that natural orbitals form a one-electron basis for which the expansion in excited Slater determinants converges more rapidly [49]. Natural orbitals are defined as the eigenfunctions of the one-electron reduced density matrix. The one-electron reduced density matrix, γ , is given by

$$\gamma(\mathbf{r}_1, \mathbf{r}'_1) = \int d\mathbf{r}_2 d\mathbf{r}_3 \dots d\mathbf{r}_N \Psi(\mathbf{r}_1, \mathbf{r}_2, \dots, \mathbf{r}_N) \Psi^*(\mathbf{r}'_1, \mathbf{r}_2, \dots, \mathbf{r}_N). \quad (6.1)$$

Insertion of the definition for Ψ^{HF} from Eq. (4.1) into Eq. (6.1) yields the reduced density matrix in the HF approximation,

$$\gamma^{\text{HF}}(\mathbf{r}_1, \mathbf{r}'_1) = \sum_i^{\text{occ.}} \psi_i(\mathbf{r}_1) \psi_i^*(\mathbf{r}'_1), \quad (6.2)$$

which can be transformed into the HF orbital basis, where it becomes a diagonal matrix in the occupied-occupied orbital (i, j) block and zero otherwise [9]

$$\gamma_{ij}^{\text{HF}} = \begin{cases} \delta_{ij} & \text{if } i, j \in \text{occupied} \\ 0 & \text{otherwise} \end{cases}.$$

In general if $|\Psi\rangle$ is not $|\Psi^{\text{HF}}\rangle$, but a linear combination of several determinants, γ is not diagonal. Insertion of $e^{\mathbf{T}_2}|\Psi^{\text{HF}}\rangle$ into Eq. (6.1) yields

$$\gamma^{\mathbf{T}_2}(\mathbf{r}_1, \mathbf{r}'_1) = \int d\mathbf{r}_2 d\mathbf{r}_3 \dots d\mathbf{r}_N (\Psi^{\text{HF}} + \sum_{kl}^{\text{occ. unocc.}} t_{kl}^{ab} \Psi_{kl}^{ab}) (\Psi^{\text{HF}} + \sum_{k'l'}^{\text{occ. unocc.}} t_{k'l'}^{a'b'} \Psi_{k'l'}^{a'b'})^*, \quad (6.3)$$

where we have neglected all quadruply or higher excited determinants. The indices k, l and a, b denote occupied and unoccupied one-electron spin-orbitals, respectively. Carrying out the integrations in Equation (6.3) yields

$$\gamma^{\mathbf{T}_2}(\mathbf{r}_1, \mathbf{r}'_1) = \sum_i^{\text{occ.}} \psi_i(\mathbf{r}_1) \psi_i^*(\mathbf{r}'_1) + \frac{1}{2} \sum_{kl}^{\text{occ. unocc.}} \sum_{cab} t_{kl}^{ac} t_{kl}^{bc*} \psi_a(\mathbf{r}_1) \psi_b^*(\mathbf{r}'_1). \quad (6.4)$$

Transforming the density matrix from Eq. (6.4) into the HF orbital basis yields

$$\gamma_{ab}^{\mathbf{T}_2} = \begin{cases} \gamma_{ab}^{\text{HF}} & \text{if } a \text{ or } b \in \text{occupied} \\ \frac{1}{2} \sum_{kl}^{\text{occ. unocc.}} \sum_c t_{kl}^{ac} t_{kl}^{bc*} & \text{if } a \text{ and } b \in \text{unoccupied.} \end{cases} \quad (6.5)$$

Note that $\gamma_{ab}^{\mathbf{T}_2}$ is non-diagonal in the virtual-virtual orbital block. Eigenvectors and eigenvalues of $\gamma_{ab}^{\mathbf{T}_2}$ are called natural orbitals and occupation numbers, respectively. The occupation numbers lie between 0 and 1 and imply that the corresponding natural orbital occurs in no or all configurations (excited Slater determinants), respectively [49]. An N -electron system is therefore determined by a *single Slater determinant, if exactly N natural orbitals are fully occupied.*

Now we are faced with the difficulty of how to exploit natural orbitals in actual calculations: To evaluate Eq. (6.5) we need to know the amplitudes

t_{ij}^{ab} , for which we would have to carry out the correlated calculation. Fortunately it turns out that natural orbitals, calculated at the level of MP2 (i.e. employing t_{ij}^{ab} 's from Eq. (5.22)) are already a good approximation to the exact natural orbitals. The MP2 natural orbitals may then be used in more sophisticated methods such as CCSD, where a faster convergence with respect to the employed one-electron orbital basis allows for a significant reduction in the computational cost.

Inserting Eq. (5.22) into Eq. (6.5) yields the second-order one-electron reduced density matrix at the level of MP2:

$$\gamma_{ab}^{\text{MP2}} = \begin{cases} \gamma_{ab}^{\text{HF}} & \text{if } a \text{ or } b \in \text{occupied} \\ \frac{1}{2} \sum_{ij}^{\text{occ.}} \sum_c^{\text{unocc.}} \frac{\langle cb||ij \rangle \langle ij||ca \rangle}{\Delta_{ij}^{cb} \Delta_{ij}^{ca}} & \text{if } a \text{ and } b \in \text{unoccupied,} \end{cases} \quad (6.6)$$

where

$$\Delta_{ij}^{cb} = \epsilon_c + \epsilon_b - \epsilon_i - \epsilon_j. \quad (6.7)$$

The ϵ_n correspond to one-electron Hartree-Fock eigenvalues. Note that the evaluation of Eq. (6.6) scales as $\mathcal{O}(N^5)$ for atoms and molecules, where N is a measure of the system size. In Ref. [50], Aquilante et. al. propose to approximate the virtual-virtual block of the density matrix by

$$\sum_{ci} \frac{\langle cb||ii \rangle \langle ii||ca \rangle}{\Delta_{ii}^{cb} \Delta_{ii}^{ca}}. \quad (6.8)$$

This *approximate MP2 density matrix* may be constructed with a computational effort that scales as $\mathcal{O}(N^4)$ only.

Chapter 7

Quasiparticles in the MP2 and *GW* approximation

In order to calculate band gaps (as measured in Photoemission spectroscopy) in the MP2 approximation, it is common practice to define the QP energies for the valence state, $\tilde{\epsilon}_v^{\text{MP2}}$, and conduction band state, $\tilde{\epsilon}_c^{\text{MP2}}$, according to Koopman's theorem as MP2 total energy differences of the $(N + 1)$, (N) and $(N - 1)$ electron systems [52]:

$$\tilde{\epsilon}_v^{\text{MP2}} = E_C^N - E_C^{N-1} \quad (7.1)$$

$$\tilde{\epsilon}_c^{\text{MP2}} = E_C^{N+1} - E_C^N. \quad (7.2)$$

Equations (7.1) and (7.2) constitute corrections to the HF orbital energies defined in Eq. (4.7).

Inserting the expression for the MP2 correlation energies from Eq. (5.32) into the equations above yields the following expressions for the MP2 QP energies of the valence ($\tilde{\epsilon}_v^{\text{MP2}}$) and conduction band ($\tilde{\epsilon}_c^{\text{MP2}}$):

$$\begin{aligned} \tilde{\epsilon}_v^{\text{MP2}}(\omega) = & \sum_{i,a,b} \frac{\langle iv|ab\rangle (2\langle iv|ab\rangle - \langle iv|ba\rangle)^*}{\epsilon_i^{\text{HF}} + \omega - \epsilon_a^{\text{HF}} - \epsilon_b^{\text{HF}}} \\ & - \sum_{i,j,a} \frac{\langle ij|av\rangle (2\langle ij|av\rangle - \langle ij|va\rangle)^*}{\epsilon_i^{\text{HF}} + \epsilon_j^{\text{HF}} - \epsilon_a^{\text{HF}} - \omega} \end{aligned} \quad (7.3)$$

$$\begin{aligned} \tilde{\epsilon}_c^{\text{MP2}}(\omega) = & \sum_{i,a,b} \frac{\langle ic|ab\rangle (2\langle ic|ab\rangle - \langle ic|ba\rangle)^*}{\epsilon_i^{\text{HF}} + \omega - \epsilon_a^{\text{HF}} - \epsilon_b^{\text{HF}}} \\ & - \sum_{i,j,a} \frac{\langle ij|ac\rangle (2\langle ij|ac\rangle - \langle ij|ca\rangle)^*}{\epsilon_i^{\text{HF}} + \epsilon_j^{\text{HF}} - \epsilon_a^{\text{HF}} - \omega} \end{aligned} \quad (7.4)$$

These are evaluated for $\omega = \epsilon_v^{\text{HF}}$ and $\omega = \epsilon_c^{\text{HF}}$, respectively. Note that Eqs. (7.3) and (7.4) include direct as well as exchange-like terms. The exchange-like term in the MP2 QP energy corrects for the self-screening and self-correlation error in the direct term [48], which includes an unphysical contribution: the particle or hole state is involved in the screening of its own charge density, and thus experiences its own correlation potential. We note in passing that self-screening and self-correlation are interchangeable terms in second-order theory.

Equations (7.3) and (7.4) represent a first approximation to the self-consistent MP2 QP energies. In a self-consistent scheme all one-electron energies ϵ^{HF} on the right-hand side of Eqs. (7.3) and (7.4), respectively, would be replaced by the corresponding MP2 QP energies. Accordingly Eqs. (7.3) and (7.4) become nonlinear equations, requiring a rather time consuming iterative solution and an update of all orbital energies. It is also not guaranteed that such an iterative solution will yield an improved description of the QP energies.

Here we apply a limited self-consistent scheme, in which the one-electron energy of the considered orbital only ($\omega = \epsilon_v^{\text{HF}} \rightarrow \omega = \epsilon_v^{\text{MP2}}$ or $\omega = \epsilon_c^{\text{HF}} \rightarrow \omega = \epsilon_c^{\text{MP2}}$) is updated on the right-hand side. As such, the quasiparticle energy equation reads

$$\epsilon_n^{\text{MP2}} = \epsilon_n^{\text{HF}} + \tilde{\epsilon}_n^{\text{MP2}}(\epsilon_n^{\text{MP2}}) \quad (7.5)$$

Expanding $\tilde{\epsilon}_n^{\text{MP2}}(\epsilon_n^{\text{MP2}})$ in the above equation around ϵ_n^{HF} yields

$$\epsilon_n^{\text{MP2}} = \epsilon_n^{\text{HF}} + \tilde{\epsilon}_n^{\text{MP2}}(\epsilon_n^{\text{HF}}) + \left. \frac{\partial \tilde{\epsilon}_n^{\text{MP2}}(\omega)}{\partial \omega} \right|_{\epsilon_n^{\text{HF}}} (\epsilon_n^{\text{MP2}} - \epsilon_n^{\text{HF}}) + \left. \frac{\partial^2 \tilde{\epsilon}_n^{\text{MP2}}(\omega)}{\partial \omega^2} \right|_{\epsilon_n^{\text{HF}}} (\epsilon_n^{\text{MP2}} - \epsilon_n^{\text{HF}})^2 + \dots \quad (7.6)$$

Truncating the Taylor expansion at linear terms in $(\epsilon_n^{\text{MP2}} - \epsilon_n^{\text{HF}})$ gives

$$\epsilon_n^{\text{MP2}} = \epsilon_n^{\text{HF}} + \tilde{\epsilon}_n^{\text{MP2}}(\epsilon_n^{\text{HF}}) + \left. \frac{\partial \tilde{\epsilon}_n^{\text{MP2}}(\omega)}{\partial \omega} \right|_{\epsilon_n^{\text{HF}}} (\epsilon_n^{\text{MP2}} - \epsilon_n^{\text{HF}}). \quad (7.7)$$

Solving the above equation for ϵ_n^{MP2} yields

$$\epsilon_n^{\text{MP2}} = \epsilon_n^{\text{HF}} + \tilde{\epsilon}_n^{\text{MP2}}(\epsilon_n^{\text{HF}}) Z_n^{\text{MP2}}. \quad (7.8)$$

The normalization factor Z_n^{MP2} is defined as,

$$Z_n^{\text{MP2}} = \left(1 - \frac{\partial \tilde{\epsilon}_n^{\text{MP2}}(\omega)}{\partial \omega} \Big|_{\epsilon_n^{\text{HF}}} \right)^{-1}, \quad (7.9)$$

and is proportional to the norm of the QP peak. This approach is inspired by the QP equation discussed below, and it is compatible to the approach usually taken in the solid state community to solve the QP equations in Hedin's GW method [25, 53].

Strictly speaking, Koopman's theorem is a rather *ad hoc* approach to derive equations for the QP energies. The appropriate theoretical framework is the solution of the QP equation

$$(T + V_H + \Sigma(\epsilon)) \phi = \epsilon \phi, \quad (7.10)$$

where T is the kinetic energy operator, V_H the Hartree potential, and Σ the self-energy operator. The latter is energy dependent and non-local (i.e. depends on two coordinates). The QP equation has a discrete set of solutions $\{\epsilon_n, \phi_n\}$, where the orbitals ϕ_n are commonly referred to as Dyson orbitals or Lehmann amplitudes. Closed exact expressions for the self-energy operator $\Sigma(\epsilon)$ are not known. Two commonly used methods to construct approximations to the self-energy are the *GW* method of Hedin [25], applied in the solid state community [53], and the ADC (algebraic diagrammatic construction) method of Schirmer, Cederbaum and Walter [54], often used by quantum chemists.

In all practical applications the *GW* expressions are subject to further approximations. For solid state systems the simplest and computationally most convenient approximation is to evaluate *GW* within the random phase approximation (RPA). It can be derived from Hedin's set of equations by neglecting vertex corrections [25]. This yields a simple closed expression for the self-energy Σ_{GW} , which reads [53]:

$$\Sigma_{GW}(\mathbf{r}, \mathbf{r}', \omega) = \frac{i}{2\pi} \int_{-\infty}^{\infty} d\omega' W(\mathbf{r}, \mathbf{r}', \omega') G(\mathbf{r}', \mathbf{r}, \omega + \omega') \quad (7.11)$$

$$G(\mathbf{r}', \mathbf{r}, \omega) = \sum_{n'} \frac{\psi_{n'}(\mathbf{r}) \psi_{n'}^*(\mathbf{r}')}{\omega - \epsilon_{n'} + i\eta \text{sgn}(\epsilon_{n'} - \mu)} \quad (7.12)$$

$$W(\mathbf{r}, \mathbf{r}', \omega) = \nu(\mathbf{r}, \mathbf{r}') + \int d\mathbf{r}'' \int d\mathbf{r}''' \nu(\mathbf{r}, \mathbf{r}'') \chi(\mathbf{r}'', \mathbf{r}''', \omega) \nu(\mathbf{r}''', \mathbf{r}') \quad (7.13)$$

$$\chi(\mathbf{r}, \mathbf{r}', \omega) = \chi_0(\mathbf{r}, \mathbf{r}', \omega) + \int d\mathbf{r}'' \int d\mathbf{r}''' \chi_0(\mathbf{r}, \mathbf{r}'', \omega) \nu(\mathbf{r}'', \mathbf{r}''') \chi(\mathbf{r}''', \mathbf{r}', \omega) \quad (7.14)$$

54 Chapter 7. Quasiparticles in the MP2 and GW approximation

Here χ is the polarizability of the interacting many-electron system calculated in the random phase approximation. χ_0 and ν are the independent particle polarizability and the bare Coulomb kernel given by

$$\chi_0(\mathbf{r}, \mathbf{r}', \omega) = - \sum_i^{\text{occ.}} \sum_a^{\text{unocc.}} 2 \left(\frac{\psi_a^*(\mathbf{r}') \psi_i(\mathbf{r}') \psi_i^*(\mathbf{r}) \psi_a(\mathbf{r})}{\epsilon_a - \epsilon_i - \omega - i\eta} + \frac{\psi_i^*(\mathbf{r}') \psi_a(\mathbf{r}') \psi_a^*(\mathbf{r}) \psi_i(\mathbf{r})}{\epsilon_a - \epsilon_i + \omega + i\eta} \right) \quad (7.15)$$

and

$$\nu(\mathbf{r}, \mathbf{r}') = \frac{e^2}{|\mathbf{r} - \mathbf{r}'|}, \quad (7.16)$$

respectively. In practical GW-RPA calculations, $\{\epsilon_i, \psi_i\}$ and $\{\epsilon_a, \psi_a\}$ commonly refer to occupied and unoccupied Kohn-Sham orbital energies (or orbitals), respectively. We note that the RPA equations specified here neglect all ladder diagrams, as is usually done in the solid state community (direct RPA).

A crude approximation to Eq. (7.14) is the termination of the Dyson-like equation at the lowest order:

$$\chi(\omega) = \chi_0(\omega), \quad (7.17)$$

i.e., $W = \nu + \nu\chi_0\nu$. In appendix B we show that this allows to recover the direct terms in the MP2 QP energies given in Eq. (7.3). This has one important implication: MP2 can be only reliable *if the polarizability of the system is small*, as higher order terms are not accounted for. We will illustrate this in Sec. 9.2.4.

We now return to the previous QP equation (7.3), to illustrate the implication of an update of $\omega = \epsilon_v^{\text{HF}}$ and $\omega = \epsilon_c^{\text{HF}}$ on the right-hand side of Eq. (7.3). If we assume that the Dyson orbitals are well approximated by the HF orbitals $\phi_n = \psi_n^{\text{HF}}$, one can, multiplying the QP equation (7.10) from the left with $\psi_n^{\text{HF}*}$ and integrating over space, obtain:

$$\langle \psi_n^{\text{HF}} | T + V_H + \Sigma^{\text{MP2}}(\epsilon_n) | \psi_n^{\text{HF}} \rangle = \epsilon_n \langle \psi_n^{\text{HF}} | \psi_n^{\text{HF}} \rangle. \quad (7.18)$$

Linearization of the self-energy around ϵ_n^{HF} and solving for ϵ_n yields Eq. (7.8) (compare Ref. [41]). This implies that updating the orbital energy of the considered orbital is consistent with a self-consistent solution of the QP equation,

with the self-energy operator calculated non-self-consistently at the MP2 level. Exactly the same is usually done in GW calculations for solids, but there the self-energy is approximated at the RPA level instead of the MP2 level, and the orbitals are from Kohn-Sham instead of HF calculations. Both approximations are expected to work in a certain regime: (i) for weakly polarizable atoms, molecules and solids, HF+MP2 should be a good approximation, since higher order effects are small, whereas (ii) the RPA is justified if the effect of exchange-like diagrams is small, which is expected to be the case for densely packed strongly polarizable solids.

We finally note that a similar analogy between RPA and MP2 has already been discussed for the correlation energies in section 5.6.

Chapter 8

The PAW Method

The projector augmented wave (PAW) method was introduced by Blöchl [55]. Its close relationship to the ultrasoft pseudopotentials method of Vanderbilt [56] was shown by Kresse and Joubert [57]. This section provides a short introduction to this topic.

Under periodic boundary conditions the mutually orthogonal DFT or HF one-electron (canonical) orbitals are Bloch functions, i.e.,

$$\langle \mathbf{r} + \mathbf{R} | \psi_a \rangle = \langle \mathbf{r} | \psi_a \rangle e^{i\mathbf{k}_a \cdot \mathbf{R}} \quad (8.1)$$

for all lattice vectors \mathbf{R} . The index a , labeling the one-electron orbitals ψ , is understood to be shorthand for the band index n_a and the Bloch wave vector \mathbf{k}_a (i.e., $a \equiv n_a \mathbf{k}_a$). The wave vector is conventionally chosen to lie within the first Brillouin zone. In the PAW method, the one-electron wave functions ψ_a are derived from the pseudo-wave-functions $\tilde{\psi}_a$ by means of a linear transformation

$$|\psi_a\rangle = |\tilde{\psi}_a\rangle + \sum_i (|\phi_i\rangle - |\tilde{\phi}_i\rangle) \langle \tilde{p}_i | \tilde{\psi}_a \rangle. \quad (8.2)$$

The pseudo wave functions $\tilde{\psi}_a$ are the variational quantities of the PAW-method and are expanded in reciprocal space using plane waves,

$$\langle \mathbf{r} | \tilde{\psi}_a \rangle = \frac{1}{\sqrt{\Omega}} \sum_{\mathbf{G}} C_{a\mathbf{G}} e^{i(\mathbf{k}_a + \mathbf{G}) \cdot \mathbf{r}}. \quad (8.3)$$

In Eq. (8.2), the index i is a shorthand for the atomic site \mathbf{R}_i , the angular momentum quantum numbers l_i and m_i , and an additional index ϵ_i denoting

the linearization energy [57]. The all-electron partial waves ϕ_i are the solution to the radial Schrödinger equation for the non-spin-polarized reference atom at specific energies ϵ_i and specific angular momenta l_i . The pseudo-partial waves, $\tilde{\phi}_i$, are equivalent to the all-electron partial waves outside a core radius r_c and match continuously onto ϕ_i inside the core radius. The partial waves ϕ_i and $\tilde{\phi}_i$ are represented on radial logarithmic grids. The projector functions \tilde{p}_i are constructed in such a way that they are dual to the pseudo partial waves, i.e.,

$$\langle \tilde{p}_i | \tilde{\phi}_j \rangle = \delta_{ij}. \quad (8.4)$$

8.1 The charge density

It can be shown [57] from Eq. (8.2) that the electronic charge density in the PAW method may be written as

$$n(\mathbf{r}) = \tilde{n}(\mathbf{r}) + n^1(\mathbf{r}) - \tilde{n}^1(\mathbf{r}), \quad (8.5)$$

where $\tilde{n}(\mathbf{r})$, $n^1(\mathbf{r})$, and $\tilde{n}^1(\mathbf{r})$ are defined as,

$$\tilde{n}(\mathbf{r}) = \sum_n f_n \langle \tilde{\psi}_n | \mathbf{r} \rangle \langle \mathbf{r} | \tilde{\psi}_n \rangle, \quad (8.6)$$

$$\tilde{n}^1(\mathbf{r}) = \sum_{i,j} \rho_{ij} \langle \tilde{\phi}_i | \mathbf{r} \rangle \langle \mathbf{r} | \tilde{\phi}_j \rangle, \quad (8.7)$$

$$n^1(\mathbf{r}) = \sum_{i,j} \rho_{ij} \langle \phi_i | \mathbf{r} \rangle \langle \mathbf{r} | \phi_j \rangle, \quad (8.8)$$

with

$$\rho_{ij} = \sum_n f_n \langle \tilde{\psi}_n | \tilde{p}_i \rangle \langle \tilde{p}_j | \tilde{\psi}_n \rangle \delta_{\tau_i \tau_j}. \quad (8.9)$$

$\delta_{\tau_i \tau_j}$ is one if i and j refer to the same atomic site. The f_n denote the occupancies of the n -th one-electron state. The ρ_{ij} can be regarded as the one-electron reduced density matrix at each atomic site.

Typically, the summation over n in Eqs. (8.6) and (8.9) is restricted to include only the chemically relevant valence states. The charge density corresponding to the (tightly bound) core electrons is kept frozen (frozen core approximation). The total charge density is then given by

$$n = (\tilde{n} + \tilde{n}_{Zc}) - (\tilde{n}^1 + \tilde{n}_{Zc}^1) + (n^1 + n_{Zc}), \quad (8.10)$$

where $n_{Zc} = n_Z + n_c$. n_Z and n_c denote the nuclear and core electronic charge densities, respectively. The pseudized core density \tilde{n}_{Zc} is a charge distribution that is equivalent to n_{Zc} beyond the core radius r_c and has the same moment as n_{Zc} inside r_c

$$\int_{\Omega_r} n_{Zc}(\mathbf{r}) d^3\mathbf{r} = \int_{\Omega_r} \tilde{n}_{Zc}(\mathbf{r}) d^3\mathbf{r}, \quad (8.11)$$

where \int_{Ω_r} stands for the integration on the radial logarithmic grid.

In order to ensure a correct and efficient treatment of the long-range electrostatic interactions the total charge density is rewritten as

$$n = (\tilde{n} + \tilde{n}_{Zc} + \hat{n}) - (\tilde{n}^1 + \tilde{n}_{Zc} + \hat{n}) + (n^1 + n_{Zc}) \quad (8.12)$$

where \hat{n} is a compensating charge density that is chosen such that $\tilde{n}^1 + \hat{n}$ has exactly the same multipole moments as n^1 [see Eq. (27) in Ref. [57]].

8.2 The total energy in the PAW method

Within the PAW method the total energy can be written as [57]

$$E = \tilde{E} + E^1 - \tilde{E}^1. \quad (8.13)$$

Here the last two terms are evaluated on atom-centered radial logarithmic grids whereas the first term is calculated on a regular grid.

This separation is very efficient from a computational point of view and can be performed for any observable that corresponds to a semilocal operator.

The three contributions to Eq. (8.13) are given by

$$\begin{aligned} \tilde{E} = & \sum_n f_n \left\langle \tilde{\psi}_n \left| -\frac{1}{2}\Delta \right| \tilde{\psi}_n \right\rangle + E_{xc}[\tilde{n} + \hat{n} + \tilde{n}_c] \\ & + E_H[\tilde{n} + \hat{n}] + \int_{\Omega_R} v_H[\tilde{n}_{Zc}] [\tilde{n}(r) + \hat{n}(r)] dr + U(R, Z_{ion}) \end{aligned} \quad (8.14)$$

$$\begin{aligned} \tilde{E}^1 = & \sum_{i,j} \rho_{ij} \left\langle \tilde{\phi}_i \left| -\frac{1}{2}\Delta \right| \tilde{\phi}_j \right\rangle + \overline{E_{xc}[\tilde{n}^1 + \hat{n} + \tilde{n}_c]} \\ & + \overline{E_H[\tilde{n}^1 + \hat{n}]} + \int_{\Omega_R} v_H[\tilde{n}_{Zc}] [\tilde{n}^1(r) + \hat{n}(r)] dr \end{aligned} \quad (8.15)$$

$$\begin{aligned} E^1 = & \sum_{i,j} \rho_{ij} \left\langle \phi_i \left| -\frac{1}{2}\Delta \right| \phi_j \right\rangle + \overline{E_{xc}[\tilde{n}^1 + n_c]} \\ & + \overline{E_H[n^1]} + \int_{\Omega_R} v_H[n_{Zc}] n^1(r) dr \end{aligned} \quad (8.16)$$

where

$$v_H[n](r) = \int \frac{n(r')}{|r - r'|} dr' E_H[n] = \frac{1}{2} \int dr \int dr' \frac{n(r)n(r')}{|r - r'|}, \quad (8.17)$$

and \tilde{n}_c is a partial electronic core charge density (see Sec. II C of Ref. [57]). In equations (8.15) and (8.16) the overline denotes that these terms are evaluated on the radial grid.

Equations (8.14), (8.15) and (8.16) hold for the total energy in DFT. To obtain the Hartree-Fock energy, we replace E_{xc} by the Fock-exchange energy, E_X , where

$$E_X = -\frac{1}{2} \sum_{m=1}^N \sum_{n=1}^N \langle \psi_m \psi_n | \psi_n \psi_m \rangle f_n f_m. \quad (8.18)$$

The evaluation of the electron repulsion integrals $\langle \psi_m \psi_n | \psi_n \psi_m \rangle$ will be outlined in the following section.

8.3 Electron repulsion integrals in the PAW method

In this section, we will derive the PAW expressions for the electron repulsion (or two-electron-four-orbital) integrals

$$V_{ij}^{ab} = \langle ij | ab \rangle = e^2 \int \frac{\langle \psi_i | \mathbf{r} \rangle \langle \mathbf{r} | \psi_a \rangle \langle \psi_j | \mathbf{r}' \rangle \langle \mathbf{r}' | \psi_b \rangle}{|\mathbf{r} - \mathbf{r}'|} d\mathbf{r}' d\mathbf{r}. \quad (8.19)$$

From the definition in Eq. (8.1) it is straightforward to show that the two-electron-four-orbital integrals, V_{ij}^{ab} , are non-zero only if the crystal momentum is conserved, i.e.,

$$\mathbf{k}_b = \mathbf{k}_i + \mathbf{k}_j - \mathbf{k}_a - \mathbf{K}, \quad (8.20)$$

where \mathbf{K} is any reciprocal lattice vector that takes \mathbf{k}_b into the first Brillouin zone. Since, the electron repulsion integrals are closely related to the expressions for the HF exchange integrals within the PAW framework, we adopt a similar notation as in Ref. [58].

In the PAW method, the overlap charge density that arises from two orbitals i and a

$$n_{ia}(\mathbf{r}) = \langle \psi_i | \mathbf{r} \rangle \langle \mathbf{r} | \psi_a \rangle \quad (8.21)$$

may be written as

$$n_{ia}(\mathbf{r}) = [\tilde{n}_{ia}(\mathbf{r}) + \hat{n}_{ia}(\mathbf{r})] - [\tilde{n}_{ia}^1(\mathbf{r}) + \hat{n}_{ia}^1(\mathbf{r})] + n_{ia}^1(\mathbf{r}) \quad (8.22)$$

where

$$\tilde{n}_{ia}(\mathbf{r}) = \langle \tilde{\psi}_i | \mathbf{r} \rangle \langle \mathbf{r} | \tilde{\psi}_a \rangle \quad (8.23)$$

is the PS overlap charge density expanded in the plane wave basis set, and

$$\tilde{n}_{ia}^1(\mathbf{r}) = \sum_{\mu\nu} \langle \tilde{\phi}_\mu | \mathbf{r} \rangle \langle \mathbf{r} | \tilde{\phi}_\nu \rangle \langle \tilde{\psi}_i | \tilde{p}_\mu \rangle \langle \tilde{p}_\nu | \tilde{\psi}_a \rangle \delta_{\tau_\mu \tau_\nu} \quad (8.24)$$

$$n_{ia}^1(\mathbf{r}) = \sum_{\mu\nu} \langle \phi_\mu | \mathbf{r} \rangle \langle \mathbf{r} | \phi_\nu \rangle \langle \psi_i | \tilde{p}_\mu \rangle \langle \tilde{p}_\nu | \psi_a \rangle \delta_{\tau_\mu \tau_\nu}, \quad (8.25)$$

are the PS and AE overlap charge densities expanded in the basis of partial waves in the PAW spheres. $\delta_{\tau_\mu \tau_\nu}$ is one if μ and ν refer to the same atomic site. From hereon, the superscript 1 is used to label *one-center* contributions, quantities that are expressed in terms of partial waves. They are non-zero within the PAW spheres only. The delta functions in Eq. (8.24) and (8.25) express the fact that the one-center expansions are defined to be site diagonal. The so-called compensation charge densities \tilde{n}_{ia}^1 and \hat{n}_{ia} are *both* spatially confined to the PAW spheres, and are chosen in such a way that the sum $\tilde{n}_{ia}^1 + \hat{n}_{ia}^1$ has the same moments as the AE one-center overlap charge density n_{ia}^1 (for a detailed description of the construction scheme see Sec. II B of Ref. [58]).

Introducing the following shorthand

$$\{f\}\{g\} = e^2 \int \frac{f(\mathbf{r})g^*(\mathbf{r}')}{|\mathbf{r} - \mathbf{r}'|} d\mathbf{r}' d\mathbf{r}, \quad (8.26)$$

the two-electron-four-orbital integrals V_{ij}^{ab} of Eq. (8.19), may be rewritten as

$$\{n_{ia}\}\{n_{bj}\} = \{\tilde{n}_{ia} + \hat{n}_{ia}\}\{\tilde{n}_{bj} + \hat{n}_{bj}\} - \{\tilde{n}_{ia}^1 + \hat{n}_{ia}^1\}\{\tilde{n}_{bj}^1 + \hat{n}_{bj}^1\} + \{n_{ia}^1\}\{n_{bj}^1\}, \quad (8.27)$$

i.e., analogous to Eq. (20) of Ref. [58]. It is important to note that the right-hand side of Eq. (8.27) contains integrals over quantities expressed either solely in the plane wave basis (the first term) or solely in the basis of partial waves (the last two terms) [N.B.: the introduction of the compensation charges in Eq. (8.22) enables this separation]. Thus within the PAW formalism the two-electron-four-orbital integrals consist of three separate contributions:

$$V_{ij}^{ab} = \tilde{V}_{ij}^{ab} - {}^1\tilde{V}_{ij}^{ab} + {}^1V_{ij}^{ab} \quad (8.28)$$

with

$$\begin{aligned}\tilde{V}_{ij}^{ab} &= \{\tilde{n}_{ia} + \hat{n}_{ia}\} \{\tilde{n}_{bj} + \hat{n}_{bj}\}, \\ {}^1\tilde{V}_{ij}^{ab} &= \{\tilde{n}_{ia}^1 + \hat{n}_{ia}^1\} \{\tilde{n}_{bj}^1 + \hat{n}_{bj}^1\}, \\ {}^1V_{ij}^{ab} &= \{n_{ia}^1\} \{n_{bj}^1\}.\end{aligned}\quad (8.29)$$

The last term on the right-hand side of Eq. (8.28), the AE one-center contribution to V_{ij}^{ab} , is given by

$${}^1V_{ij}^{ab} = e^2 \sum_{\kappa\lambda\mu\nu} \int \frac{\langle\phi_\kappa|\mathbf{r}\rangle\langle\mathbf{r}|\phi_\lambda\rangle\langle\phi_\mu|\mathbf{r}'\rangle\langle\mathbf{r}'|\phi_\nu\rangle}{|\mathbf{r}-\mathbf{r}'|} d\mathbf{r}' d\mathbf{r} \langle\tilde{\psi}_i|\tilde{p}_\kappa\rangle\langle\tilde{p}_\lambda|\tilde{\psi}_a\rangle\langle\tilde{\psi}_j|\tilde{p}_\mu\rangle\langle\tilde{p}_\nu|\tilde{\psi}_b\rangle, \quad (8.30)$$

where only combinations of $\kappa\lambda\mu\nu$ on the same lattice site, i.e., $\tau_\kappa = \tau_\lambda = \tau_\mu = \tau_\nu$ are understood to contribute to the sum above. Loosely following the derivation in Sec. II D3 of Ref. [58] we rewrite the above as

$${}^1V_{ij}^{ab} = \sum_{\kappa\lambda\mu\nu} \sum_{LM} C_{l_\nu m_\nu l_\mu m_\mu}^{LM} S_{\kappa\lambda\mu\nu}^L C_{l_\kappa m_\kappa l_\lambda m_\lambda}^{LM} \langle\tilde{\psi}_i|\tilde{p}_\kappa\rangle\langle\tilde{p}_\lambda|\tilde{\psi}_a\rangle\langle\tilde{\psi}_j|\tilde{p}_\mu\rangle\langle\tilde{p}_\nu|\tilde{\psi}_b\rangle, \quad (8.31)$$

where we introduced the Clebsch-Gordan coefficients $C_{lm'l'm'}^{LM}$ and the Slater-type integrals

$$S_{\kappa\lambda\mu\nu}^L = \frac{4\pi e^2}{2L+1} \int_0^{r_c} dr u_\kappa(r) u_\lambda(r) \int_0^{r_c} dr' u_\mu(r') u_\nu(r') \begin{pmatrix} r_{\leq}^L \\ r_{>}^{L+1} \end{pmatrix}. \quad (8.32)$$

The function u_i denotes the radial part of the AE partial wave:

$$\phi_i(\mathbf{r}) = \frac{1}{|\mathbf{r}-\tau_i|} u_i(|\mathbf{r}-\tau_i|) Y_{l_i m_i}(\widehat{\mathbf{r}-\tau_i}). \quad (8.33)$$

Completely analogous, the second term on the right-hand side of Eq. (8.28), the PS one-center contribution to V_{ij}^{ab} , may be written as

$${}^1\tilde{V}_{ij}^{ab} = \sum_{\kappa\lambda\mu\nu} \sum_{LM} C_{l_\nu m_\nu l_\mu m_\mu}^{LM} \tilde{S}_{\kappa\lambda\mu\nu}^L C_{l_\kappa m_\kappa l_\lambda m_\lambda}^{LM} \langle\tilde{\psi}_i|\tilde{p}_\kappa\rangle\langle\tilde{p}_\lambda|\tilde{\psi}_a\rangle\langle\tilde{\psi}_j|\tilde{p}_\mu\rangle\langle\tilde{p}_\nu|\tilde{\psi}_b\rangle \quad (8.34)$$

with

$$\begin{aligned}\tilde{S}_{\kappa\lambda\mu\nu}^L &= \frac{4\pi e^2}{2L+1} \int_0^{r_c} dr [\tilde{u}_\kappa(r) \tilde{u}_\lambda(r) + \tilde{q}_{\kappa\lambda}^L g_L(r)] \\ &\quad \times \int_0^{r_c} dr' [\tilde{u}_\mu(r') \tilde{u}_\nu(r') + \tilde{q}_{\mu\nu}^L g_L(r')] \begin{pmatrix} r_{\leq}^L \\ r_{>}^{L+1} \end{pmatrix},\end{aligned}\quad (8.35)$$

where \tilde{u}_i and $\bar{q}_{ij}^L g_L$ denote the radial parts of the PS partial wave $\tilde{\phi}_i$ and the appropriate compensation charge, respectively. The construction scheme for the latter is specified in Sec. II D4 of Ref. [58] and will not be repeated here.

Finally, the first term on the right-hand side of Eq. (8.28), the plane wave contribution to V_{ij}^{ab} , is given by

$$\tilde{V}_{ij}^{ab} = e^2 \int \frac{[\tilde{n}_{ia} + \hat{n}_{ia}](\mathbf{r}) [\tilde{n}_{bj} + \hat{n}_{bj}]^*(\mathbf{r}')}{|\mathbf{r} - \mathbf{r}'|} d\mathbf{r}' d\mathbf{r}. \quad (8.36)$$

Introducing the plane wave expansion of the compensated PS overlap charge density,

$$[\tilde{n}_{ia} + \hat{n}_{ia}](\mathbf{r}) = \sum_{\mathbf{G}} C_{ia\mathbf{G}} e^{i(\mathbf{k}_a - \mathbf{k}_i + \mathbf{G}) \cdot \mathbf{r}}, \quad (8.37)$$

we rewrite Eq. (8.36) as follows

$$\tilde{V}_{ij}^{ab} = \frac{4\pi e^2}{\Omega} \sum_{\mathbf{G}} \frac{C_{ia\mathbf{G}} C_{bj\mathbf{G}-\mathbf{K}}^*}{|\mathbf{k}_a - \mathbf{k}_i + \mathbf{G}|^2}, \quad (8.38)$$

where \mathbf{k}_i is the Bloch wave vector associated with the PS orbital $\tilde{\psi}_i$ [see Eq. (8.3)], and \mathbf{G} and \mathbf{K} are reciprocal lattice vectors. The latter is given by Eq. (8.20). The plane wave expansion of the PS overlap charge densities is usually limited to the components for which $(\hbar^2/2m_e)|\mathbf{k}_a - \mathbf{k}_i + \mathbf{G}|^2$ is below some kinetic energy cutoff E_χ .

The evaluation of the plane wave contributions to the two-electron-four-orbital integrals is complicated by the fact that Eq. (8.38) has an integrable divergence in the long-wavelength limit, i.e., for $\mathbf{G} = \mathbf{k}_i - \mathbf{k}_a$ (and $\mathbf{G} = \mathbf{k}_b - \mathbf{k}_j + \mathbf{K}$). In this case, Eq. (8.38) can be rewritten as

$$\tilde{V}_{ij}^{ab} = \frac{4\pi e^2}{\Omega} \sum_{\mathbf{G}} \frac{C_{n_i\mathbf{k}_a, n_a\mathbf{k}_a, \mathbf{G}} C_{n_b\mathbf{k}_b, n_j\mathbf{k}_b, \mathbf{G}}^*}{|\mathbf{G}|^2}. \quad (8.39)$$

The long-wavelength limit ($\mathbf{G} = \mathbf{0}$) of which is given by (see Sec. II D of Ref. [59]),

$$\begin{aligned} \lim_{\mathbf{q} \rightarrow \mathbf{0}} \frac{C_{n_i\mathbf{k}_a + \mathbf{q}, n_a\mathbf{k}_a, \mathbf{0}} C_{n_b\mathbf{k}_b + \mathbf{q}, n_j\mathbf{k}_b, \mathbf{0}}^*}{|\mathbf{q}|^2} &= \lim_{\mathbf{q} \rightarrow \mathbf{0}} \frac{\langle \psi_{n_i\mathbf{k}_a + \mathbf{q}} | e^{i\mathbf{q} \cdot \mathbf{r}} | \psi_{n_a\mathbf{k}_a} \rangle \langle \psi_{n_j\mathbf{k}_b} | e^{-i\mathbf{q} \cdot \mathbf{r}} | \psi_{n_b\mathbf{k}_b + \mathbf{q}} \rangle}{|\mathbf{q}|^2} \\ &= \hat{\mathbf{q}} \cdot \langle \vec{\beta}_{n_i\mathbf{k}_a} | \tilde{u}_{n_a\mathbf{k}_a} \rangle \langle \tilde{u}_{n_j\mathbf{k}_b} | \vec{\beta}_{n_b\mathbf{k}_b} \rangle \cdot \hat{\mathbf{q}}, \end{aligned} \quad (8.40)$$

where $\vec{\beta}_{n\mathbf{k}}$ is the derivative of the cell periodic part of the wave function $\psi_{n\mathbf{k}}$ with respect to \mathbf{k} given by [59]

$$|\vec{\beta}_{n\mathbf{k}}\rangle = \left(1 + \sum_{ij} |\tilde{p}_{i\mathbf{k}}\rangle Q_{ij} \langle \tilde{p}_{j\mathbf{k}}|\right) |\nabla_{\mathbf{k}} \tilde{u}_{n\mathbf{k}}\rangle + i \left(\sum_{ij} |\tilde{p}_{i\mathbf{k}}\rangle Q_{ij} \langle \tilde{p}_{j\mathbf{k}}|(\mathbf{r} - \mathbf{R}_i)\right) |\tilde{u}_{n\mathbf{k}}\rangle - i \sum_{ij} |\tilde{p}_{i\mathbf{k}}\rangle \vec{\tau}_{ij} \langle \tilde{p}_{j\mathbf{k}}|\tilde{u}_{n\mathbf{k}}\rangle. \quad (8.41)$$

$\tilde{u}_{n\mathbf{k}}$ denotes the cell periodic part of the PS wave function $\tilde{\psi}_{n\mathbf{k}}$.

Part II

Results

Chapter 9

Second-order Møller-Plesset perturbation theory

The wave function based treatment of electronic correlation constitutes a hierarchy of methods that, starting from the one-electron Hartree-Fock approximation, allows one to rigorously and systematically approximate the many-body nature of the true ground state wave function. The simplest form of the wave function based treatment of correlation, is the canonical formulation of second-order Møller-Plesset [11] (MP2) perturbation theory.

In this chapter, we compute the atomization energy of the LiH molecule and the cohesive energy of bulk LiH using the Hartree-Fock and MP2 methods, and demonstrate the accuracy of our approach through a comparison with Gaussian-type-orbital (GTO) calculations for the molecule and the results of Casassa *et al.* [78] and Manby *et al.* [80, 81, 82] for the solid. Moreover we apply our MP2 implementation to a series of archetypical semiconductors and insulators. We calculate lattice constants, bulk moduli, atomization energies and quasiparticle band gaps at the level of HF and MP2 in order to evaluate the accuracy of these methods for solid state systems.

9.1 Basis set convergence and the LiH test

The atomization (cohesive) energy $\mathcal{D}_0(M)$ per unit cell of a molecule (extended system) M , is defined as

$$\mathcal{D}_0(M) = \mathcal{E}_0(M) - \sum_X \mathcal{E}_0(X), \quad (9.1)$$

where $\mathcal{E}_0(M)$ is the total energy per unit cell of M , and the sum is taken over the total energies $\mathcal{E}_0(X)$ of the constituent atoms X in their spin-polarized symmetry-broken ground state (i.e., no fractional occupancies). In this section, we compute the atomization energy of a LiH molecule and the cohesive energy of bulk LiH, at the HF+MP2 level. We demonstrate the accuracy of our canonical MP2 implementation through a comparison with GTO calculations for the molecule, and to the results of local MP2 (CRYSCOR) calculations of Casassa *et al.* [78] and the hierarchical extrapolation scheme of Manby *et al.* [80] for the solid. Furthermore we address two important aspects of HF+MP2 calculations under periodic boundary conditions using a plane wave basis set: (i) the convergence of the MP2 correlation energy with respect to the kinetic energy cutoff, E_χ , imposed on the plane wave basis set expansion of the PS overlap charge densities [see Eq. (8.37)], and (ii) the convergence of the HF and MP2 correlation energies of atoms and molecules with respect to the volume of the supercell.

All calculations in the present work are “all-electron” calculations, in the sense that all electrons of the system are treated as valence electrons, i.e. we do not invoke the *frozen core* approximation. The PAW datasets were constructed with two s and two p partial waves as additional one-center basis functions in the case of H, and three s , three p , and two d partial waves in the case of Li. In all calculations the plane wave basis set expansion of the wave functions was cut off at a kinetic energy of 550 eV.

9.1.1 The Li atom and LiH molecule

The convergence behavior of the MP2 correlation energy with respect to the size of the plane wave basis set expansion of the PS overlap charge densities is illustrated in Fig. 9.1. It shows the dependence of the MP2 correlation energy of a Li atom on the kinetic energy cutoff E_χ applied in Eqs. (8.37) and (8.38) [i.e., the basis set expansion of the overlap charge densities is limited to those plane wave components with $(\hbar^2/2m_e)|\mathbf{k}_a - \mathbf{k}_i - \mathbf{G}|^2 < E_\chi$]. Unfortunately, the convergence of the MP2 correlation energy with respect to E_χ is quite slow. Following the work of Harl *et al.* [45], we assume that for sufficiently high E_χ the MP2 correlation energy behaves as

$$E_c(E_\chi) = E_c(E_\chi \rightarrow \infty) + CE_\chi^{-3/2} \quad (9.2)$$

and extrapolate our data using this functional form to determine the infinite basis set limit $E_c(E_\chi \rightarrow \infty)$. This procedure is indicated by the dotted (blue) lines in Fig. 9.1 and the inset shows the energies $E_c(E_\chi \rightarrow \infty)$. Furthermore, as expected, under periodic boundary conditions the MP2 correlation energy of the Li atom is seen to depend on the size of the supercell, e.g. Figure 9.1 shows the infinite basis set extrapolation of the MP2 correlation energy for a Li atom in a $6 \times 6 \times 6 \text{ \AA}^3$ (circles), $6.5 \times 6.5 \times 6.5 \text{ \AA}^3$ (squares), and $7 \times 7 \times 7 \text{ \AA}^3$ (pluses) supercell. The volume dependence of $E_c(E_\chi \rightarrow \infty)$ for the Li atom is shown in Fig. 9.2. At large volume Ω , the correlation energy should drop off as $1/\Omega^2$, i.e., it should show the volume dependence typical for the van der Waals interaction between the periodically repeated images of the Li atom. This volume dependence is indicated by the dotted (blue) line in Fig. 9.2, and the extrapolation of the MP2 correlation energy of the Li atom to infinite volume is shown in the inset: $E_c(E_\chi \rightarrow \infty, \Omega \rightarrow \infty) = -0.853 \text{ eV}$. Note that to correctly reproduce the $1/\Omega^2$ dependence of the correlation energy on the volume, we had to use a $(2 \times 2 \times 2)$ Γ -centered mesh of k -points, instead of the Γ -only sampling that is usually employed in supercell calculations for atoms and molecules.

To calculate the MP2-correlation contribution to the atomization energy of the LiH molecule, $\Delta E_c = E_c^{\text{LiH}} - E_c^{\text{Li}}$ (note $E_c^{\text{H}} \equiv 0$), we follow a similar procedure; extrapolation of $\Delta E_c(E_\chi, \Omega) = E_c^{\text{LiH}}(E_\chi, \Omega) - E_c^{\text{Li}}(E_\chi, \Omega)$ to the infinite plane wave basis set limit $\Delta E_c(E_\chi \rightarrow \infty, \Omega)$ followed by an extrapolation to infinite supercell volume $\Omega \rightarrow \infty$. This is shown in Figs. 9.3 and 9.4. $\Delta E_c(E_\chi, \Omega)$ converges much more rapidly with respect to E_χ than $E_c(E_\chi, \Omega)$ (compare Figs. 9.1 and 9.3). As depicted in the inset of Fig. 9.4, the extrapolation of the infinite basis set limit of ΔE_c to infinite volume yields, $\Delta E_c(E_\chi \rightarrow \infty, \Omega \rightarrow \infty) = -0.822 \text{ eV}$. This is in excellent agreement with the result obtained from Gaussian-type-orbital (GTO) calculations with GAUSSIAN03 [84], $\Delta E_c(\text{GTO}) = -0.819 \text{ eV}$. The latter was extrapolated to its infinite basis set limit from a series of calculations using Dunning's aug-cc-pCV(D,T,Q)Z and aug-cc-pV(D,T,Q)Z basis sets for Li and H, respectively.

As shown in Fig. 9.5, ΔE_{HF} , the HF contribution to $\mathcal{D}_0(\text{LiH})$ depends on the volume of the supercell as well, and converges with $1/\Omega^2$ towards $\Delta E_{\text{HF}}(\Omega \rightarrow \infty) = -1.084 \text{ eV}$, which is in perfect agreement with the result from the corresponding basis set extrapolated GTO calculations, $\Delta E_{\text{HF}}(\text{GTO}) =$

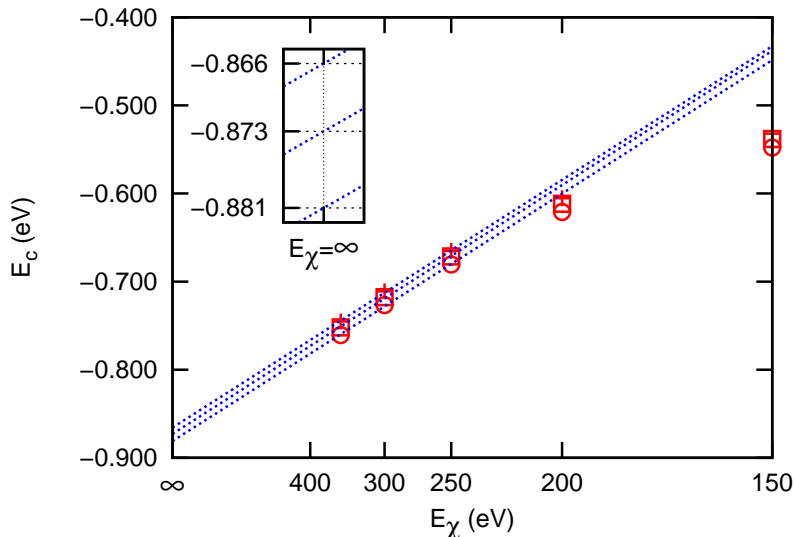


Figure 9.1: Dependence of the MP2 correlation energy E_c of a Li atom on the kinetic energy cutoff E_χ that determines the size of the plane wave basis set expansion of the overlap densities (E_c vs. $E_\chi^{-3/2}$) for three different cubic supercells of increasing size [$6 \times 6 \times 6 \text{ \AA}^3$ (circles), $6.5 \times 6.5 \times 6.5 \text{ \AA}^3$ (squares), and $7 \times 7 \times 7 \text{ \AA}^3$ (plusses)]. The extrapolation $E_\chi \rightarrow \infty$ is indicated by the dotted (blue) lines, and the inset shows $E_c(E_\chi \rightarrow \infty)$.

-1.084 eV . Beware that the convergence behaviour of E_{HF} and ΔE_{HF} with respect to the volume of the supercell depends on the way the long-wavelength limit of the Fock exchange interaction is treated. In the present work we have used the method of Massida *et al.* [85] and not a more efficient method that has recently been proposed by Spencer and Alavi [86]. From the above, the final PAW result for the atomization energy of the LiH molecule reads, $\mathcal{D}_0(\text{LiH}) = \Delta E_{\text{HF}} + \Delta E_c = -1.906 \text{ eV}$ [GTO: $\mathcal{D}_0(\text{LiH}) = -1.903 \text{ eV}$]. To ease comparison, the PAW and GTO results for the atomization energy of the LiH molecule are recapitulated in Tab. 9.1.

One important point to mention is that whereas the PAW and GTO MP2 correlation energy *differences* are in excellent agreement, the absolute MP2 correlation energies are not. The PAW MP2 correlation energies are substantially smaller than their GTO counterparts, e.g. for Li: $E_c(\text{PAW}) = -0.853 \text{ eV}$

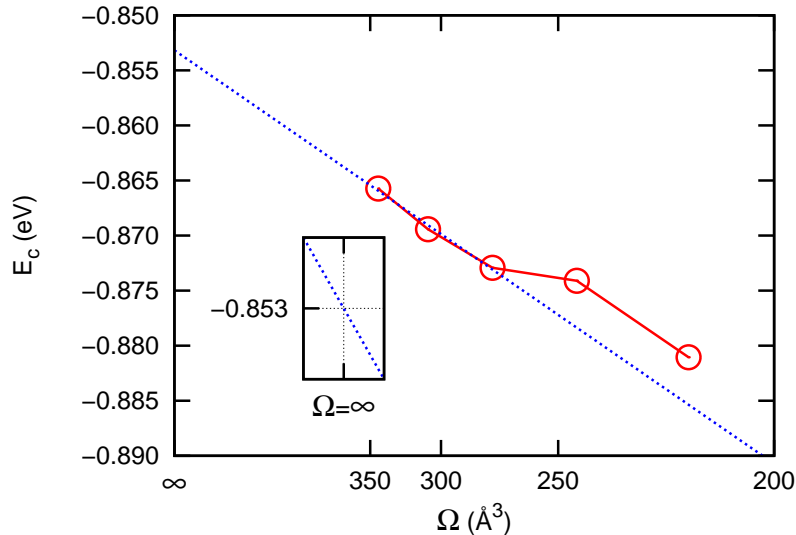


Figure 9.2: Dependence of the infinite basis set limit of the MP2 correlation energy of a Li atom, $E_c(E_\chi \rightarrow \infty)$, on Ω the volume of the supercell [$E_c(E_\chi \rightarrow \infty)$ vs. Ω^{-2}]. The extrapolation $\Omega \rightarrow \infty$ is indicated by the dotted (blue) line, and the inset shows $E_c(E_\chi \rightarrow \infty, \Omega \rightarrow \infty)$.

vs. $E_c(\text{GTO}) = -1.123$ eV despite the fact that both methods should in principle recover the all-electron result (the Li and H PAW potentials are both all-electron potentials). We believe this to be due to the fact that our MP2 calculations are not converged with respect to the basis set of additional local functions inside the PAW spheres (ϕ_ν and $\tilde{\phi}_\nu$). The one-center basis sets used in this work, however, are of sufficient quality to obtain well converged MP2 correlation energy differences. The HF calculations are less sensitive in this respect. With the PAW datasets used in this work even the absolute PAW and GTO HF total energies agree to within a few meV, e.g. for Li: $E_{\text{HF}}(\text{PAW}) = -202.258$ eV vs. $E_{\text{HF}}(\text{GTO}) = -202.255$ eV.

9.1.2 Bulk LiH

To calculate the MP2-correlation energy contribution to the atomization energy of bulk LiH we follow a similar strategy. The MP2 correlation energy

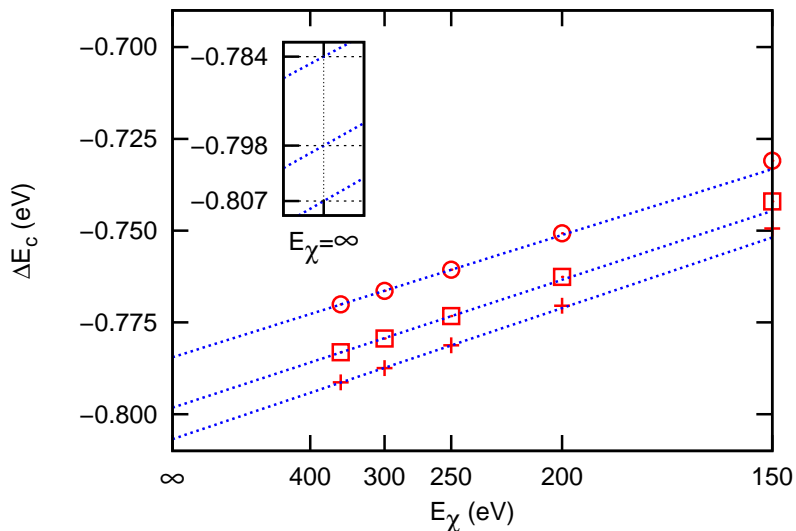


Figure 9.3: Dependence of the MP2-correlation contribution to the atomization energy of a LiH molecule, ΔE_c , on the kinetic energy cutoff E_χ that determines the size of the plane wave basis set expansion of the overlap densities (ΔE_c vs. $E_\chi^{-3/2}$), for three different cubic supercells of increasing size [$6 \times 6 \times 6 \text{ \AA}^3$ (circles), $6.5 \times 6.5 \times 6.5 \text{ \AA}^3$ (squares), and $7 \times 7 \times 7 \text{ \AA}^3$ (plusses)]. The extrapolation $E_\chi \rightarrow \infty$ is indicated by the dotted (blue) lines, and the inset shows $\Delta E_c(E_\chi \rightarrow \infty)$.

Table 9.1: The atomization energy \mathcal{D}_0 , and the HF and MP2-correlation contributions to \mathcal{D}_0 , ΔE_{HF} and ΔE_c , for a LiH molecule, from PAW and GTO calculations. All energies in eV.

	ΔE_{HF}	ΔE_c	\mathcal{D}_0
PAW	-1.084	-0.822	-1.906
GTO	-1.084	-0.819	-1.903

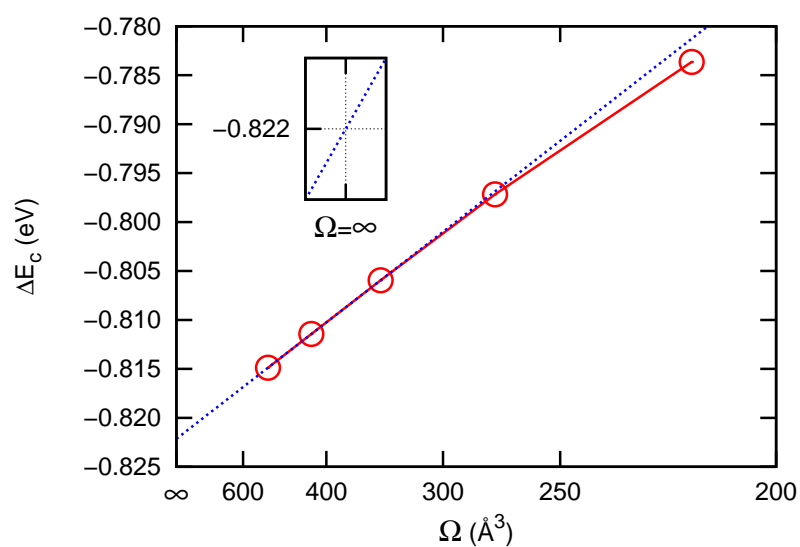


Figure 9.4: Dependence of the infinite basis set limit of the MP2-correlation contribution to the atomization energy of a LiH molecule, $\Delta E_c(E_\chi \rightarrow \infty)$, on Ω the volume of the supercell [$\Delta E_c(E_\chi \rightarrow \infty)$ vs. Ω^{-2}]. The extrapolation $\Omega \rightarrow \infty$ is indicated by the dotted (blue) line, and the inset shows $\Delta E_c(E_\chi \rightarrow \infty, \Omega \rightarrow \infty)$.

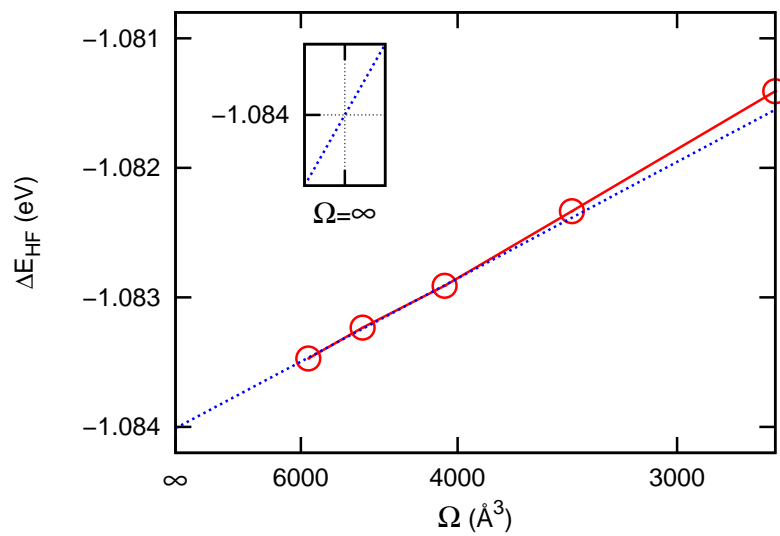


Figure 9.5: Dependence of the HF contribution to the atomization energy of a LiH molecule, ΔE_{HF} , on the volume, Ω , of the supercell (ΔE_{HF} vs. Ω^{-2}). The extrapolation $\Omega \rightarrow \infty$ is indicated by the dotted (blue) line, and the inset shows $\Delta E_{\text{HF}}(\Omega \rightarrow \infty)$.

Table 9.2: Convergence of the basis set extrapolated MP2 correlation energy of bulk LiH with respect to the sampling of the first Brillouin zone. The latter is specified by n , which is short for a $(n \times n \times n)$ Γ -centered mesh of k -points. In addition to the total MP2 correlation energy $E_c(E_\chi \rightarrow \infty)$ we list the “direct” (D) and “exchange”-like (X) contributions that make up the total MP2 correlation energy, as well as the ratio X/D . All energies are in eV.

n	D	X	X/D	$E_c(E_\chi \rightarrow \infty)$
2	-3.667	1.684	-0.459(3)	-1.983
3	-3.679	1.653	-0.449(2)	-2.027
4	-3.706	1.666	-0.449(5)	-2.040
5	-3.716	1.668	-0.449(0)	-2.048
6	-3.717			-2.048
8	-3.718			-2.049
10	-3.719			-2.049

of the bulk $E_c(E_\chi, n)$ is evaluated at the 0K experimental volume, $\Omega_{0K}^{\text{exp.}} = 17.03 \text{ \AA}^3$, for a series of increasingly dense $(n \times n \times n)$ Γ -centered meshes of k -points ($n = 2, 3, 4$, and 5), at several different cutoff energies $E_\chi = 150, 200, 250, 300$, and 350 eV. These energies are then extrapolated to $E_\chi \rightarrow \infty$ in the manner described in Sec. 9.1.1 (see for instance Fig. 9.2). The resulting basis set extrapolated MP2 correlation energies $E_c(E_\chi \rightarrow \infty, n)$ are listed in Tab. 9.2.

Unfortunately $E_c(E_\chi \rightarrow \infty, n)$ converges quite slowly with respect to n , a problem that is compounded by the fact that the computational effort scales as N_k^3 , where $N_k = n^3$ is the total number of k -points in the mesh. We note, however, that the ratio between the contributions to the MP2 correlation energy stemming from terms that involve $|V_{ij}^{ab}|^2$ and those that involve $V_{ij}^{ab}V_{ij}^{ba*}$ [see Eqs. (8.19), (5.33) and (5.34)], the so-called “direct” (D) and “exchange”-like (X) contributions, has converged to $X/D = -0.449$ already at $n = 3$ (see Tab. 9.2). This allows to exploit an alternative scheme to compute the direct contributions to the MP2 correlation energy scaling as N_k^2 (see Sec. 5.6). For bulk LiH we evaluate the basis set extrapolated MP2 correlation energy (and D , X , and X/D) in the manner of Sec. 5.1 for $n = 2, 3, 4$, and 5 ,

Table 9.3: The cohesive energy \mathcal{D}_0 , and the HF and MP2-correlation contributions to \mathcal{D}_0 , ΔE_{HF} and ΔE_c , of bulk LiH. All energies in eV.

	ΔE_{HF}	ΔE_c	\mathcal{D}_0
This work	-3.583	-1.197	-4.780
Manby <i>et al.</i>	-3.591 ^a	-1.186 ^b	-4.777
Casassa <i>et al.</i>			-4.738 ^c
Exp. (0K)			-4.762 ^d

^a Ref. [81], (at $\Omega_{\text{OK}}^{\text{exp.}} = 17.03 \text{ \AA}^3$).

^b Ref. [82], (*idem*).

^c Ref. [78], (at $\Omega_0 = 16.31 \text{ \AA}^3$).

^d Ref. [80]

whereas for $n = 6, 8$, and 10 , we calculate only the direct contributions to the MP2 correlation energy D , as outlined Sec. 5.6. The fact that X/D converges rapidly with respect to n is then used to infer the total MP2 correlation energy from the corresponding direct contribution, i.e.,

$$E_c(E_\chi \rightarrow \infty, n) = \left(1 + \frac{X}{D}\Big|_{n=5}\right) D(E_\chi \rightarrow \infty, n), \quad (9.3)$$

for $n = 6, 8$, and 10 (see Tab. 9.2). As can be seen from Tab. 9.2, the MP2 correlation energy of bulk LiH converges towards $E_c(E_\chi \rightarrow \infty, n = 10) = -2.049 \text{ eV}$ (essentially converged already for $n = 5$). Hence the MP2-correlation contribution to the cohesive energy of bulk LiH amounts to $\Delta E_c^{\text{LiH}} = E_c^{\text{LiH}}(E_\chi \rightarrow \infty, n = 10) - E_c^{\text{Li}}(E_\chi \rightarrow \infty, \Omega \rightarrow \infty) = -1.196(4) \text{ eV}$, which is in excellent agreement with the result Manby *et al.* [82] obtained by means of their hierarchical extrapolation scheme, $\Delta E_c = -1.186 \text{ eV}$. Alternatively we may also compute ΔE_c^{LiH} by extrapolating

$$\Delta E_c = \lim_{E_\chi \rightarrow \infty} E_c^{\text{LiH}}(E_\chi, n = 10) - E_c^{\text{Li}}(E_\chi, \Omega \rightarrow \infty). \quad (9.4)$$

This extrapolation is shown in Fig. 9.6, and yields $\Delta E_c^{\text{LiH}} = -1.196(6) \text{ eV}$, i.e., essentially the same result as before. Note that $\Delta E_c(E_\chi)$ behaves almost perfectly as $E_\chi^{-2/3}$ over the entire range of E_χ depicted in Fig. 9.6; if one uses only the two data points at $E_\chi = 150$ and 200 eV , the extrapolation yields $\Delta E_c = -1.197(9) \text{ eV}$.

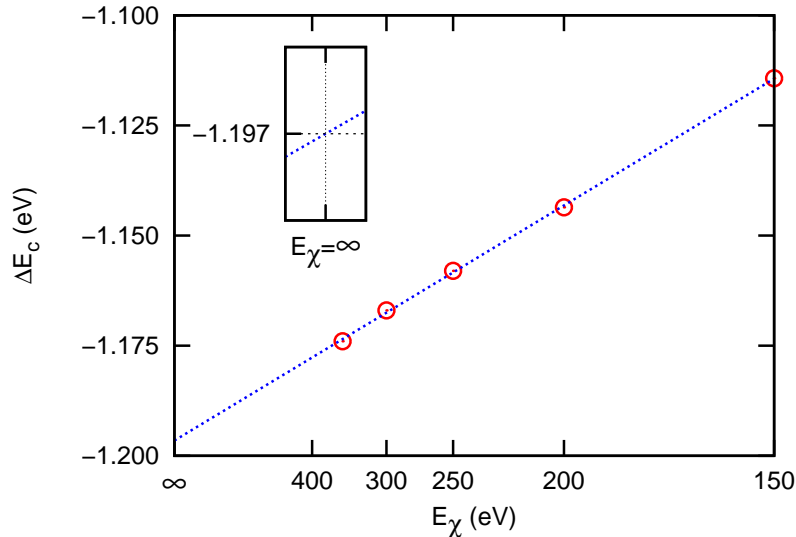


Figure 9.6: Dependence of the MP2-correlation energy contribution to the cohesive energy of bulk LiH, ΔE_c , on the energy cutoff E_χ that determines the size of the plane wave basis set expansion of the overlap densities (ΔE_c vs. $E_\chi^{-3/2}$). The extrapolation $E_\chi \rightarrow \infty$ is indicated by the dotted (blue) line, and the inset shows $\Delta E_c(E_\chi \rightarrow \infty)$.

Figure 9.7 shows the dependence of the Hartree-Fock contribution to the cohesive energy of bulk LiH, on the total number of k -points in the mesh N_k :

$$\Delta E_{\text{HF}}^{\text{LiH}}(N_k) = E_{\text{HF}}^{\text{LiH}}(N_k) - E_{\text{HF}}^{\text{Li}}(\Omega \rightarrow \infty) - E_{\text{HF}}^{\text{H}}(\Omega \rightarrow \infty), \quad (9.5)$$

where $E_{\text{HF}}^{\text{Li}}(\Omega \rightarrow \infty)$ and $E_{\text{HF}}^{\text{H}}(\Omega \rightarrow \infty)$ denote the Hartree-Fock energies of the spin polarized Li and H atoms (converged with respect to the size of the supercell). This contribution is seen to converge as N_k^{-1} towards $\Delta E_{\text{HF}}^{\text{LiH}}(N_k \rightarrow \infty) = -3.583$ eV, which is in good agreement with the work of Gillan *et al.* [81], $\Delta E_{\text{HF}}^{\text{LiH}} = -3.591$ eV. Beware that the convergence behaviour of HF calculations on periodic systems with respect to the k -point sampling depends critically on the treatment of the long-wavelength limit of the exchange interactions. As already emphasized, we have used the scheme of Massida *et al.* [85] here, although a more efficient scheme has been suggested recently.

From the above, the final PAW result for the cohesive energy of bulk LiH

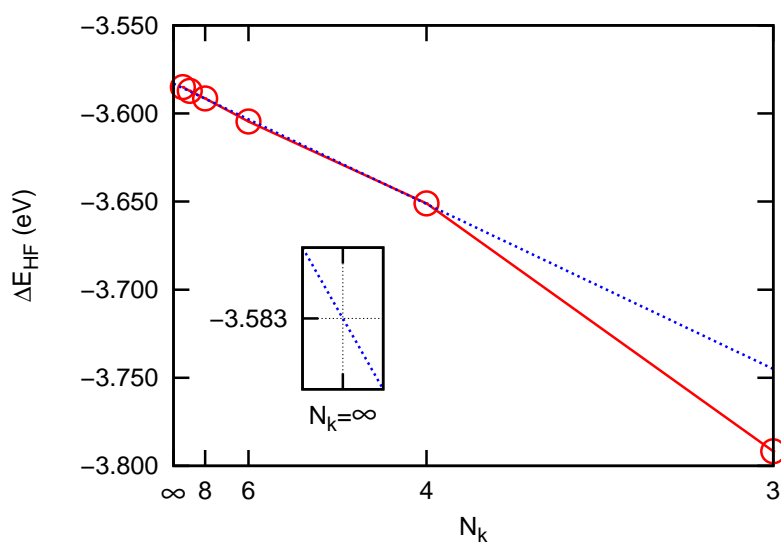


Figure 9.7: Convergence of the Hartree-Fock contribution to the cohesive energy of bulk LiH with respect to N_k , the total number of k -points (ΔE_{HF} vs. N_k^{-1}). The extrapolation $N_k \rightarrow \infty$ is indicated by the dotted (blue) line, and the inset shows $\Delta E_{\text{HF}}(N_k \rightarrow \infty)$.

reads, $\mathcal{D}_0(\text{bulk LiH}) = \Delta E_{\text{HF}}^{\text{LiH}} + \Delta E_c^{\text{LiH}} = -4.780$ eV. Table 9.3 summarizes our results and those of Refs. [78], [81], and [82]. The fact that our result for the total cohesive energy of LiH agrees with the work of Manby *et al.* [81, 82] to within a few meV (see Tab. 9.3) is a bit fortuitous; the discrepancies in the Hartree-Fock and MP2-correlation contributions to the cohesive energy partly cancel. The discrepancy between our result and the CRYSCOR LMP2 calculations of Casassa *et al.* [78] is a bit more substantial [$\mathcal{D}_0(\text{PAW}) = -4.780$ eV vs. $\mathcal{D}_0(\text{LMP2}) = -4.738$ eV]. This is further compounded by the fact that the latter were obtained at the HF+LMP2 theoretical equilibrium volume $\Omega_0 = 16.31$ Å³; the HF+LMP2 cohesive energy at the experimental volume would be in slightly worse agreement with the present work (see Fig. 2 of Ref. [78]). The most likely explanation for the difference between the PAW and LMP2 results is that the MP2-correlation contributions to the cohesive energy in the LMP2 calculations were not fully converged with respect to the basis set.

9.1.3 Conclusions and Summary

In this section, we have presented an implementation of the canonical formulation of second-order Møller-Plesset perturbation theory within the framework of the projector-augmented-wave formalism, under periodic boundary conditions using a plane wave basis set. To demonstrate the accuracy of our approach we have shown that the PAW result for the atomization energy of a LiH molecule at the HF+MP2 level of theory is in perfect agreement with well converged Gaussian-type-orbital calculations [$\mathcal{D}_0(\text{PAW}) = -1.906$ eV vs. $\mathcal{D}_0(\text{GTO}) = -1.903$ eV].

To establish the feasibility of employing MP2 perturbation theory in its canonical form to systems that are periodic in three dimensions, using the present approach, we calculated the cohesive energy of bulk LiH. The PAW HF+MP2 result for the cohesive energy of bulk LiH is in excellent agreement with the work of Manby *et al.* [$\mathcal{D}_0(\text{PAW}) = -4.780$ eV vs. $\mathcal{D}_0(\text{GTO}) = -4.777$ eV].

We have shown how the MP2 correlation energy (difference) can be extrapolated to the infinite basis set limit with respect to the kinetic energy cutoff E_χ that is imposed on the plane wave expansion of the overlap charge densities, which enter in the usual two-electron-four-orbital Coulomb repulsion integrals.

The PAW MP2 correlation energy is seen to converge as $E_\chi^{-3/2}$ at large E_χ . We have *not* tried to converge the absolute MP2 correlation energies with respect to the one-center basis set of additional local functions inside the PAW spheres. These one-center basis sets were, however, verified to be of sufficiently high quality to obtain well converged MP2 correlation energy differences, by comparison with Gaussian-type-orbital calculations.

As to be expected, in case of the supercell calculations on the Li atom and LiH molecule, the MP2 correlation energy is seen to fall off as Ω^{-2} at large volume Ω of the simulation cell (essentially the fingerprint of van der Waals interactions between the periodic images). This was used to establish the infinite volume limit of the MP2 correlation energies for finite systems.

For bulk LiH, the MP2 correlation energy had to be converged with respect to the k -point sampling density of the first Brillouin zone. Here we pointed at the possibility of exploiting the observation that the ratio X/D between the “direct” (D) and “exchange”-like (X) contributions to the MP2 correlation energy seems to converge much faster with respect to the k -point sampling than these contributions do individually. This allows one to infer the total MP2 correlation energy from a computation of the “direct” contribution only. The latter may be computed by means of an algorithm that scales as N_k^2 , where N_k is the total number of k -points in the mesh, instead of the N_k^3 scaling of the canonical MP2. Beware, however, that the rapid convergence of X/D with N_k is solely an observation from our “computer experiment” on LiH, and we have as yet no proof that this behaviour should be the norm, although preliminary results for a set of semiconductors and insulators suggest it to be.

Table 9.4: Matching radii r_c of the PAW potentials used in the present work. If the matching radii differ for specific quantum numbers, they are specified for each l -quantum number using subscripts.

	Valence	r_c [a.u.]		Valence	r_c [a.u.]
H	1s	1.0 _s 1.1 _{pd}	Mg	2p3s	2.0 _{sd} 1.6 _p
Li	1s2s	1.2 _s 1.5 _{pd}	Al	3s3p	1.9 _{spd} 2.0 _f
B	2s2p	1.5 _s 1.7 _{pd}	Si	3s3p	1.5 _s 1.9 _{pd}
C	2s2p	1.2 _s 1.5 _{pd}	P	3s3p	1.9 _{sp} 2.0 _{df}
N	2s2p	1.3 _s 1.5 _{pd}	S	3s3p	1.7 _{spdf}
O	2s2p	1.2 _s 1.5 _{pd}	Cl	3s3p	1.7 _s 1.9 _{pdf}
F	2s2p	1.1 _s 1.4 _{pd}	Ar	3s3p	1.5 _s 1.9 _{pdf}
Ne	2s2p	1.4 _s 1.8 _{pd}	Zn	3d4s	2.0 _{sd} 2.3 _{pf}
Na	3s	2.5 _{sdf} 3.0 _p	As	3d4s4p	2.1 _{spdf}

9.2 Structural and energetic properties

A systematic evaluation of MP2 in the complete basis set (CBS) limit in order to assess the accuracy of this method for a set of solids is still missing in the literature. This chapter aims at filling this gap and providing MP2 lattice constants, atomization energies as well as quasiparticle (QP) band gaps for a number of typical semiconductors and insulators paying particular attention to converge the results with respect to the employed basis set. This section is organized as follows, in Sec. 9.2.1 we present the computational details. In Sec. 9.2.2, 9.2.3 and 9.2.4 the MP2 structural and energetic properties, and QP band gaps are summarized, respectively. Section 9.2.5 discusses the divergence of the MP2 correlation energy for metallic systems. Finally, in Sec. 9.2.6, we draw preliminary conclusions.

9.2.1 Computational Details

The pseudopotentials employed in the calculations were specifically optimized to yield accurate scattering properties well above the vacuum level and the potentials and technical details are identical to Ref. [45] and references therein. The matching radii of the PAW potentials employed in the MP2 calculations

Table 9.5: Experimentally measured or extrapolated $T = 0\text{K}$ lattice constants, a^{exp} . E_{PW} and E_{χ} denote the energy cutoffs applied to the plane wave basis set expansion of the orbitals and overlap charge densities, respectively. E_{PW}^a , E_{χ}^a and E_{PW}^g , E_{χ}^g were employed for calculating the lattice constants (a) and band gaps (g), respectively. The corresponding structures are denoted using the Strukturbericht symbols in parenthesis in the first column (A1=fcc, A4=diamond, B1=rock-salt, B3=zinc-blende). All energies and lattice constants in eV and Å, respectively.

	a^{exp}	E_{PW}^a	E_{χ}^a	E_{PW}^g	E_{χ}^g
C (A4)	3.567 ^a	550	400	360	250
Si (A4)	5.430 ^a	450	300	300	150
SiC (B3)	4.358 ^a	550	400	414	250
BN (B3)	3.607 ^b	550	400	450	250
BP (B3)	4.538 ^b	450	350		
BAs (B3)	4.777 ^b	550	400		
AlN (B3)	4.380 ^c	550	400		
AlP (B3)	5.460 ^b	450	350		
AlAs (B3)	5.658 ^b	400	300		
LiH (B1)	4.084 ^a	600	450		
LiF (B1)	4.010 ^a	600	450	500	250
LiCl (B1)	5.106 ^a	600	450		
MgO (B1)	4.207 ^a	600	450	400	250
ZnS (B3)	5.420 ^d			360	250
ZnO (B3)	4.580 ^d			400	250
Ne (A1)	4.430 ^e			400	250
Ar (A1)	5.260 ^e			300	250
Na (A1 ^f)	5.317 ^f	80	50		

^aRef. [88], ^bRef. [89], ^cRef. [90], ^dRef. [91],

^eRef. [92], ^fRef. [93]

Table 9.6: Convergence of the HF+MP2 lattice constant, a_0 , bulk modul, B_0 , and total energy, E , with respect to the employed k -mesh used in the calculation of the HF, direct MP2 (dMP2) and SOX term for diamond.

HF	dMP2	SOX	a_0 [Å]	B_0 [GPa]	E [eV]
8×8×8	6×6×6	3×3×3	3.5529	449.6	-38.9619
8×8×8	8×8×8	3×3×3	3.5507	448.7	-38.9748
8×8×8	8×8×8	4×4×4	3.5527	453.3	-39.0018
10×10×10	6×6×6	3×3×3	3.5512	448.4	-38.9489
10×10×10	8×8×8	3×3×3	3.5509	448.5	-38.9617
10×10×10	8×8×8	4×4×4	3.5510	455.2	-38.9888

are listed in Tab. 10.1.

Table 9.5 summarizes the employed energy cutoffs, experimental lattice constants as well as structures. The superscripts a and g for the energy cutoffs E in Tab. 9.5 indicate that the corresponding cutoffs were employed in the calculation of the lattice constants and atomization energies (a), and QP band gaps (g), respectively. The energy cutoffs limit the size of the basis set to PW components satisfying

$$(\hbar^2/2m_e)|\mathbf{k} + \mathbf{G}|^2 < E. \quad (9.6)$$

E_{PW} denotes the cutoff energy for the plane wave basis set of the one-electron orbitals.

As outlined in Sec. 8.3 the construction of the 4-index integrals V_{ij}^{ab} in the PAW method requires the evaluation of intermediate overlap charge densities $n_{ia}(\mathbf{r}) = \psi_i^*(\mathbf{r})\psi_a(\mathbf{r})$ which are expanded into an auxiliary PW basis set, which is limited to PW components with a kinetic energy below E_χ .

As for LiH the CBS limit was obtained assuming that for large E_χ the correlation energy E_C behaves as,

$$E_C(E_\chi) = E_C(E_\chi \rightarrow \infty) + CE_\chi^{-3/2}, \quad (9.7)$$

and extrapolating our data with respect to E_χ using this functional form [45]. Table 9.5 lists the largest E_χ out of 4 points that are used in this extrapolation. The points are equally spaced with a spacing between 30 and 50 eV. For the MP2 QP band gaps we found it unnecessary to perform an extrapolation with

respect to E_χ .

For the calculations of the lattice constants and atomization energies the second-order exchange (SOX) contributions to the MP2 energy was calculated using $(3 \times 3 \times 3)$ k -points, whereas for the direct contributions $(6 \times 6 \times 6)$ k -points were employed. For the HF part $(8 \times 8 \times 8)$ k -points were used. Table 9.6 shows the convergence of the HF+MP2 lattice constant, bulk modulus and total energy of diamond with respect to the number of k -points used in the calculation of the HF, direct MP2 and SOX contribution. The changes in the lattice constant, bulk modulus and total energy from the coarsest to the densest k -mesh listed in Table 9.6 amount to less than 0.1%, 1.5% and 30 meV, respectively, which we consider to be sufficient for the present purpose.

The HF, and MP2 “direct”, and “exchange”-like contributions to the MP2 band gaps were calculated using $(10 \times 10 \times 10)$, $(8 \times 8 \times 8)$, and $(3 \times 3 \times 3)$ k -points, respectively. These settings ensure a convergence of the MP2 band gaps to within a few 10 meV. All k -point meshes were centered at the Gamma-point.

9.2.2 Structural properties

In order to establish the quality of the MP2 method for three dimensional extended systems we have calculated lattice constants and bulk moduli for selected solids. HF and MP2 lattice constants have been obtained from fitting a Murnaghan equation of state to the corresponding calculated energy versus volume curves. The curves were fitted in the range $\Omega/\Omega_{\text{eq}}=0.85 - 1.15$ with constant steps of 0.05, where Ω_{eq} is the non zero-point corrected experimental equilibrium volume.

Figure 9.8 illustrates the relative errors of the HF as well as MP2 lattice constants. As reference, the zero-point corrected experimental lattice constants from Ref. [97] have been used. For comparison we also show the relative errors of the PBE lattice constants, which have been taken from Ref. [98] (for C, Si, SiC, LiF and MgO), Ref. [99] (for BN, BP, BAs, and LiH), and Ref. [24] (for AlN, AlP, AlAs). The PBE results will not be discussed again. The relative errors of the RPA lattice constants were also added for comparison and have been taken from Ref. [24] (for C, Si, SiC, AlN, AlP, AlAs, LiF, LiCl, and MgO) and Ref. [100] (for BN, BP, BAs, and LiH).

The relative errors in the HF lattice constants in Fig. 9.8 show the well-known

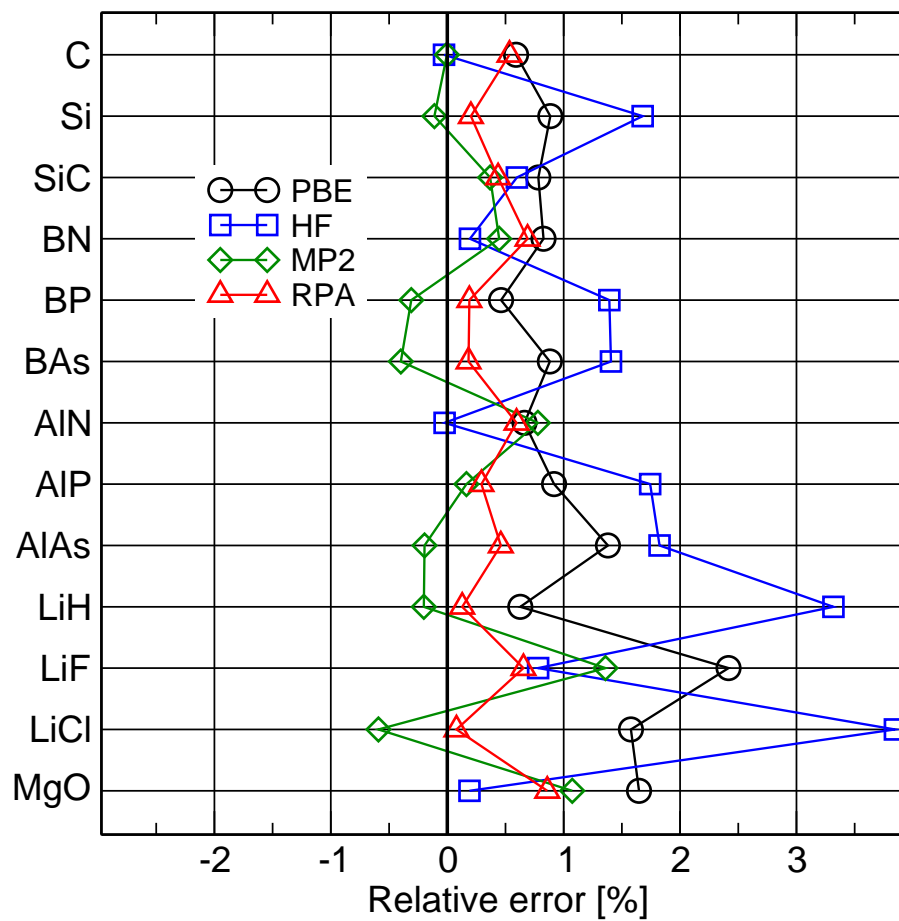


Figure 9.8: Relative errors of the calculated PBE, RPA, HF and MP2 lattice constants. As reference, zero-point corrected experimental lattice constants were used.

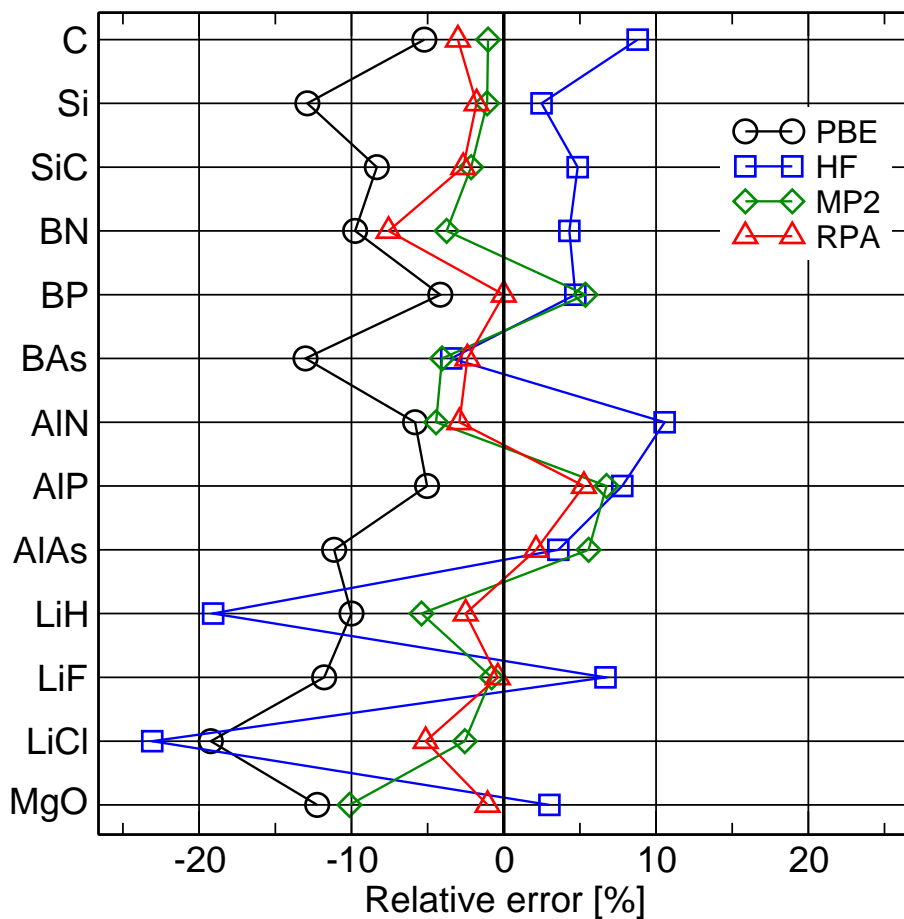


Figure 9.9: Relative errors of the calculated PBE, RPA, HF and MP2 bulk moduli. As reference, zero-point corrected experimental bulk moduli were used.

Table 9.7: Calculated HF and MP2 lattice constants as well as bulk moduli. For comparison the experimental lattice constants, a_0^{exp} , and bulk moduli, B_0^{exp} , measured at 0 K are listed as well. The experimental lattice constants and bulk moduli have been corrected for zero-point vibrational effects (lattice constants and bulk moduli in parentheses correspond to uncorrected experimental values). Lattice constants and bulk moduli are given in Å and GPa, respectively.

	a_0^{HF}	a_0^{MP2}	a_0^{exp}	B_0^{HF}	B_0^{MP2}	B_0^{exp}
C	3.552	3.553	3.553 (3.567)	495	450	455 (443)
Si	5.512	5.415	5.421 (5.430)	103	100	101 (99)
SiC	4.372	4.362	4.346 (4.358)	240	224	229 (225)
BN	3.599	3.608	3.592 (3.607)	428	395	410 (400)
BP	4.588	4.511	4.525 (4.538)	176	177	168 (165)
BAs	4.832	4.746	4.765 (4.777)	145	145	151 (149)
AlN	4.367	4.402	4.368 (4.380)	228	197	206 (202)
AlP	5.546	5.460	5.451 (5.460)	94	93	87 (86)
AlAs	5.752	5.638	5.649 (5.658)	78	80	75 (74)
LiH	4.111	3.971	3.979 (4.084)	32	38	38-43 (33-38)
LiF	4.003	4.026	3.972 (4.010)	81	76	76 (70)
LiCl	5.265	5.040	5.070 (5.106)	30	38	39 (35)
MgO	4.197	4.234	4.189 (4.207)	175	153	170 (165)
MARE	1.31%	0.46%		7.9%	4.1%	

trend of overestimation, except for C, which is negligibly underestimated. The mean absolute relative error (MARE) in the HF lattice constants is 1.31%. The overestimation ranges from only 0.2% in MgO to as much as 3.9% in LiCl. Moreover an increasing overestimation can be found for compounds with heavier constituents, $\Delta a_0^{\text{HF}}(\text{Si}) > \Delta a_0^{\text{HF}}(\text{SiC}) > \Delta a_0^{\text{HF}}(\text{C})$, $\Delta a_0^{\text{HF}}(\text{LiCl}) > \Delta a_0^{\text{HF}}(\text{LiF})$, $\Delta a_0^{\text{HF}}(\text{XAs}) > \Delta a_0^{\text{HF}}(\text{XP}) > \Delta a_0^{\text{HF}}(\text{XN})$ ($\text{X}=\text{B,Al}$), and $\Delta a_0^{\text{HF}}(\text{AlY}) > \Delta a_0^{\text{HF}}(\text{BY})$ ($\text{Y}=\text{N, P, As}$). This is usually explained by the neglect of dynamic correlation between the negatively charged cations which increases with increasing size and “softness” of the cation.

The relative errors of the MP2 lattice constants shown in Fig. 9.8 reveal that for most materials the addition of the MP2 correlation energy leads to an improvement in the description of the lattice constants compared to HF. The mean absolute relative error in MP2 is 0.46%. However, the improvements from HF to MP2 are on first sight not systematic, and in some cases the MP2 lattice constants are even worse than the HF ones, in particular, for the strongly ionic systems, MgO and LiF. Careful inspection reveals two trends: (i) with increasing polarizability of the constituents the MP2 lattice constants decrease, and (ii) MP2 lattice constants increase with increasing ionicity.

The first trend (i) is easy to understand. As a low order approximation, MP2 will overestimate the polarizability and correlation energy, if the constituents are “soft” and easily polarizable. Since the polarizability usually increases with increasing atomic size (and hence atomic number Z), one expects that MP2 becomes progressively worse with increasing atomic order number, in particular along a column of the periodic table (the atomic size decreases along a row). The effect is already visible in the absolute correlation energy of closed shell atoms. For instance, along the group He, Ne, Ar, the absolute correlation energy is underestimated for He, quite good for Ne, and overestimated for Ar [101]. Generally, for very light weakly polarizable elements HF+MP2 tends to underestimate the correlation energy, for elements with intermediate order number HF+MP2 obtains about the right results, for heavier elements it overestimates the correlation energy. This obviously relates to and explains the popularity of MP2 for main group chemistry involving first and second row elements. Our present calculations are in full accord with these rules. For MP2, the lattice constants decrease from BN, over BP to BAs, and from AlN, over AlP to AlAs, and from LiF to LiCl. This reverses the trend we have observed at the HF level: whereas for HF the lattice constants increase with

increasing atomic number of the constituents, MP2 lattice constants decrease with the atomic order number.

The second trend (ii) is more difficult to understand, but also clearly visible in our calculations. For both the series, C, BN, LiF, and Si, AlP, MgO the lattice constants increase with increasing ionicity (and band gap). It is likely that this is related to the observation that MP2 tends to give too small correlation energies for very weakly polarizable systems (LiF and MgO), gets it right for intermediate polarizabilities, and overestimates the correlation energy for strongly polarizable systems. We will come back to this issue in the conclusions.

Figure 9.9 depicts the relative errors in the calculated PBE, HF and MP2 bulk moduli. Zero-point corrected experimental bulk moduli serve as reference for the relative errors [97]. For comparison, the PBE and RPA bulk moduli have been taken from the same references as the lattice constants. An improvement in the description of the bulk moduli from HF to MP2 is observed for C, Si, SiC, BN, AlN, AlP, LiH, LiF, and LiCl whereas for BP, BAs, AlAs and MgO the correction from MP2 either overshoots or goes into the wrong direction (BP, BAs and AlAs). Nevertheless, the mean absolute relative error reduces from 7.9% in HF to 4.1% in MP2.

The agreement between the RPA results and the MP2 results for the lattice constants and bulk moduli is striking. On average the lattice constants agree to within 0.5 %. However, the RPA shows a clear tendency to overestimate the lattice constants, which we have shown to be related to the neglect of exchange-like terms in the direct RPA [101]. MP2 exhibits somewhat more scatter around experiment, with similar or larger lattice constants for light, weakly polarizable compounds, and smaller lattice constants for heavier, more polarizable elements. On average both methods, yield excellent results for the lattice constants. For the bulk moduli the behaviour is even more striking. For most systems, the errors for RPA and MP2 are similar. We believe that this is an indication that errors in *experimental bulk moduli* are responsible for the remaining discrepancy between many-body theory and experiment. Finally, Tab. 9.7 summarizes the HF, MP2 and experimental lattice constants and bulk moduli.

The final issue, we would like address is the dependence of the MP2 correlation energy on the unit cell volume. In fact, the volume dependence varies significantly from material to material. Figures 9.10 and 9.11 show the MP2

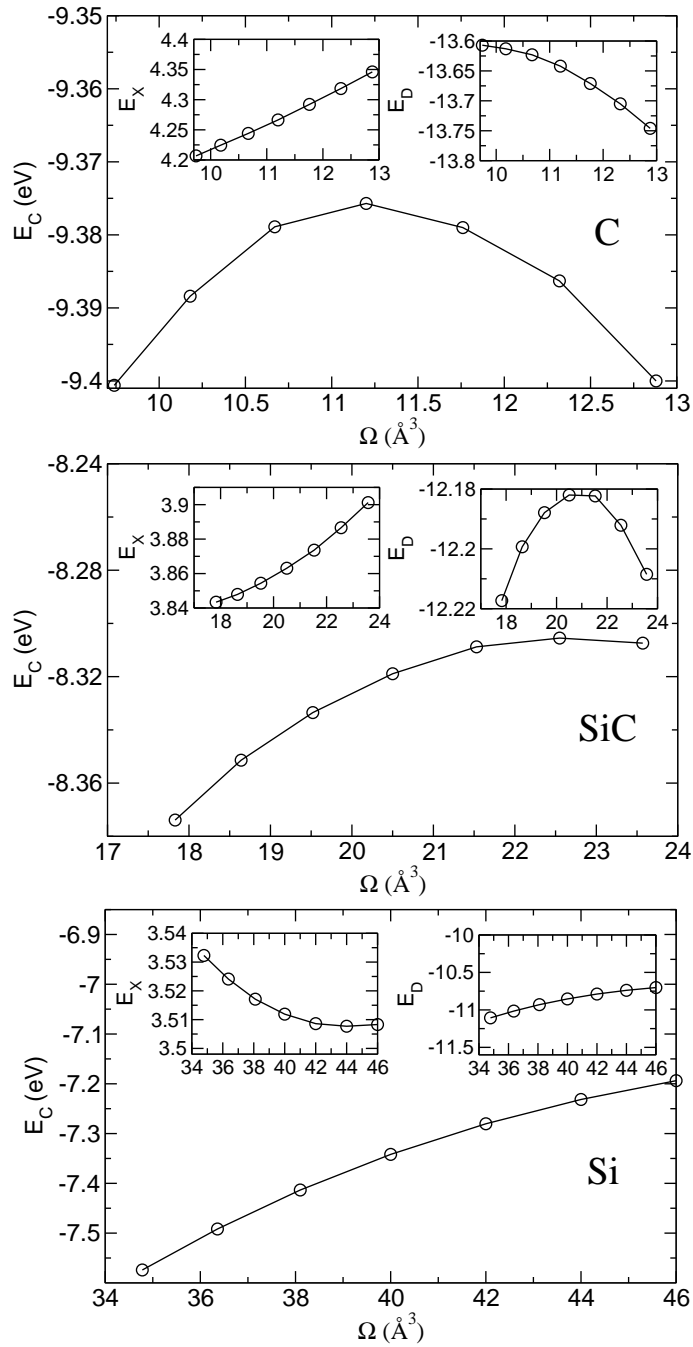


Figure 9.10: MP2 correlation energy E_C versus volume Ω for C (upper panel), SiC (middle panel) and Si (bottom panel). The insets show the contributions from the direct, E_D , and SOX, E_X , term, respectively. All energies are given in eV.

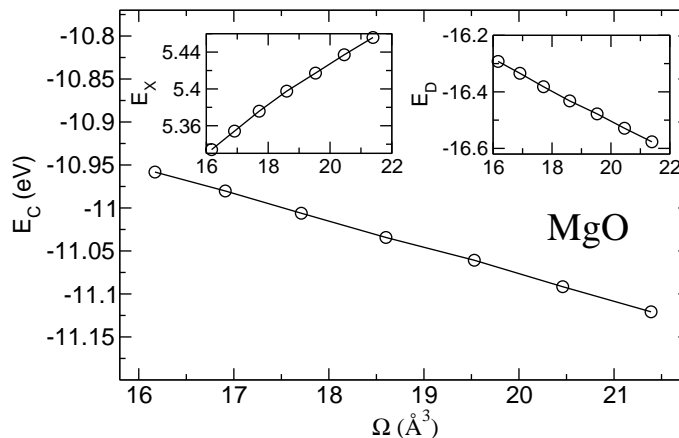


Figure 9.11: MP2 correlation energy E_C versus volume Ω for MgO. The insets show the contributions from the direct, E_D , and SOX, E_X , term, respectively. All energies are given in eV.

correlation energies, E_C , and the contributions from the direct, E_D , and SOX term, E_X , (see insets in Figs. 9.10 and 9.11) with respect to the unit cell volumes, for C, Si, SiC and MgO, respectively. The only common feature is that if the direct term is attractive, the SOX term is repulsive and *vice versa*. Apart from this, the behavior is rather different, varying from a parabolic shape for C, over weak attraction for SiC and Si to a repulsive linear behavior for MgO. A simple linear behavior is also observed for LiH [102], as well as LiF. This is important because if the volume dependence of the correlation energy is well approximated by a linear slope, it suffices to calculate the correlation energy for two volumes only. Generally, however, this is not the case, but instead the correlation energy exhibits a sizable curvature around the equilibrium volume, in particular for covalently bonded systems. Most likely there is no deeper physical principle underlying this observation, but the results highlight that the volume dependence of the correlation energy needs to be calculated carefully at several points around the equilibrium volume without *a priori* assumptions.

Table 9.8: PBE, HF and MP2 Atomization energies in eV/atom. Experimental values are corrected for zero-point vibrations [97]. DFT-PBE atomization energies have been taken from Ref.[24] unless stated otherwise.

E_{at}	PBE	HF	MP2	Exp.
C	7.72	5.28	7.97	7.55
Si	4.55	2.97	5.05	4.68
SiC	6.40	4.49	6.86	6.48
BN	6.94 ^a	4.74	7.12	6.68
BP	5.16 ^a	3.38	5.61	5.09
BAs	4.50 ^a	2.74	5.06	
AlN	5.72	3.86	6.07	5.85
AlP	4.09	2.46	4.32	4.32
AlAs	3.69	2.09	3.95	3.82
LiH	2.38 ^a	1.79	2.39	2.49
LiF	4.33	3.34	4.49	4.46
LiCl	3.37	2.70	3.64	3.59
MgO	4.98	3.59	5.35	5.20
MAE	0.16	1.59	0.23	

^afrom Ref. [99]

9.2.3 Atomization energies

Table 9.8 summarizes the calculated HF and MP2 atomization energies of C, Si, SiC, BN, BP, BAs, AlN, AlP, AlAs, LiH, LiF, LiCl and MgO. For comparison, we also list the PBE atomization energies. HF dramatically underestimates the atomization energies with a mean absolute error of 1.59 eV/atom and a maximum error of 2.27 eV/atom (for C).

The mean absolute error of the MP2 atomization energies given in Tab. 9.8 is 230 meV/atom, which is slightly worse than a MAE of 144 meV/atom that was obtained for a set of 17 small closed-shell molecules [103]. MP2 overestimates the atomization energies for the systems that we have studied in this work, with the single exception of LiH. The largest overestimation is observed for BP and amounts to 520 meV. A more detailed analysis is difficult since the errors are affected by both the description of the atom and the solid. Without accurate reference values for the solids (and atoms), it is difficult to make a final assessment. Tentatively, however, the overbinding is larger for covalently bonded systems and fairly small for ionic systems with a large band gap. The overbinding might well be related to the tendency of MP2 to overcorrelate more strongly polarizable systems.

9.2.4 Band gaps

Table 9.9 lists the HF, MP2 and experimental fundamental band gaps as well as exchange-like contributions to the MP2 band gap for Si, SiC, C, ZnS, BN, ZnO, MgO, LiF, Ar, and Ne. Note that in Tab. 9.9 the band gaps of C, SiC, Si and BN are indirect, whereas the band gaps of ZnO, ZnS, MgO, LiF, Ne and Ar are direct.

All HF band gaps are too large compared to experiment. Adding the QP correlation energy at the MP2 level to the HF eigenenergies results in a reduction of the band gaps; in simple words, correlation closes the band gap, since the HF exchange is screened by correlation effects (in particular by direct or Coulomb correlation). We find a dramatic underestimation of the MP2 band gaps for Si and SiC, resulting even in negative band gaps. In these systems, MP2 overestimates the effect of correlation on the band gap dramatically. For other systems, such as ZnO, ZnS, C and BN, MP2 is closer to the experimental value, but the results are still unsatisfactory. For the large gap systems Ar,

Table 9.9: Hartree-Fock (ϵ_g^{HF}), MP2 (ϵ_g^{MP2}) and experimental (ϵ_g^{exp}) band gaps, as well as exchange-like contributions to the MP2 band gap ϵ_g^{SOX} . The experimental band gaps have been taken from Ref. [104] (see also references therein). The different systems are ordered by their corresponding experimental static dielectric constant ϵ_0 . All band gaps in eV.

	ϵ_0^{exp}	ϵ_g^{HF}	ϵ_g^{MP2}	ϵ_g^{SOX}	ϵ_g^{exp}
Si	11.90	7.1	-1.2	-0.04	1.2
SiC	6.52	8.7	-0.8	0.04	2.4
C	5.70	13.1	1.9	-0.21	5.5
ZnS	5.13	10.1	2.0	0.21	3.9
BN	4.50	13.8	3.1	0.1	6.3
ZnO	3.74	11.1	2.1	0.52	3.4
MgO	3.00	15.5	7.1	0.43	7.8
LiF	1.90	21.8	14.2	0.67	14.2
Ar		18.1	13.7	0.24	14.2
Ne		25.3	20.3	0.76	21.7

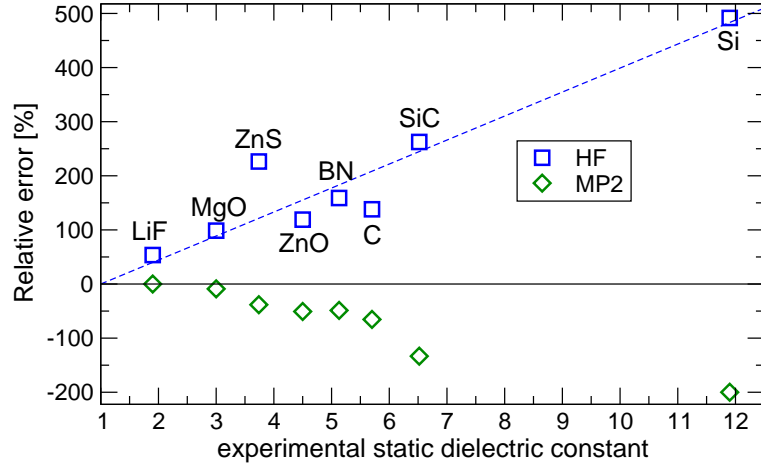


Figure 9.12: Relative errors of HF and MP2 QP band gaps with respect to the experimental static dielectric constant. Lines are guide to the eye.

Ne, LiF and MgO, however, the MP2 QP gaps are in satisfactory agreement with experiment.

The second-order exchange contribution to the MP2 band gap, ϵ_g^{SOX} , is always less than 16% of the contribution from the direct term and it opens the gap in all cases except for Si and C. The SOX term in the MP2 QP energy corrects for the self-screening and self-correlation error in the direct term [48], which includes an unphysical contribution: the particle or hole state is involved in the screening of its own charge density, and thus experiences its own correlation potential. We note in passing that self-screening and self-correlation are interchangeable terms in second-order theory.

As a result of self-correlation, the (N+1) electron energy is generally too low, and the (N-1) electron energy too high, which results in too small band gaps if the SOX term is neglected. Direct or Coulomb correlation reduces the gap, because it screens the HF exchange, and self-screening leads to an overscreening and overestimation of the correlation effect. The SOX term reduces this effect and therefore increases the band gap. Moreover we observe that $\frac{\partial \epsilon_n^{\text{MP2}}(\omega)}{\partial \omega} \approx \frac{\partial \epsilon_n^{\text{dMP2}}(\omega)}{\partial \omega}$, because $\frac{\partial \epsilon_n^{\text{SOX}}(\omega)}{\partial \omega} \approx 0$. This implies that the weight of the QP peak is almost entirely determined by the direct term, whereas the SOX term only shifts the position of the peak.

The errors in the HF and MP2 band gaps are correlated with the exper-

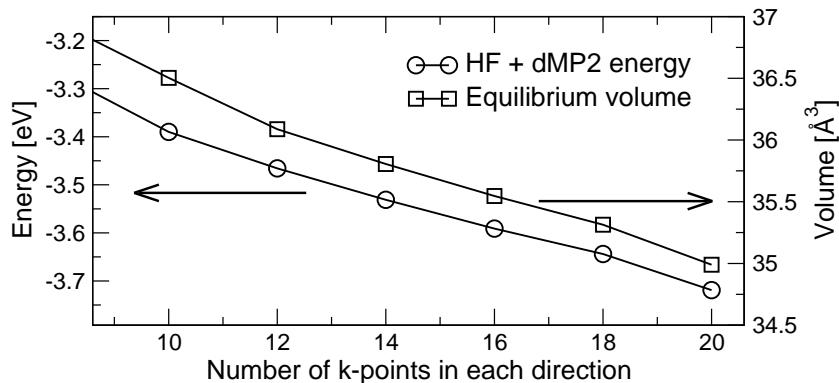


Figure 9.13: HF plus dMP2 energy as well as equilibrium volume of face-centered-cubic sodium with respect to the number of k -points in each direction.

imental static dielectric constant: Figure 9.12 shows the relative error of the HF and MP2 QP band gaps with respect to the experimental static dielectric constants. The HF band gap is a good approximation for the true QP band gap for systems with a dielectric constant around one [see Eq. (B.4)], but, due to the neglect of Coulomb correlation it can not describe the band gap for systems with a sizable polarizability. In MP2, however, a crude, low order truncation of the polarizability is used [Eq. (7.17)], which is a good approximation only if the polarizability is small. Both trends are confirmed in Fig. 9.12. The error in the HF gap increases roughly linearly with increasing experimental static dielectric constant. The error in the MP2 band gaps is small for weakly polarizable systems, but grows rapidly with increasing dielectric constant (compare also Table 9.9). As a result, bulk MP2 band gaps are only reliable if the static dielectric constant ϵ is smaller than 3.

9.2.5 Metallic sodium

The electronic correlation energy in second-order perturbation theory diverges for the 3-D free electron gas [105]. However, this does not necessarily imply that properties such as the equilibrium volume diverge as well. Moreover, one might hope that using Hartree-Fock as reference state lifts this divergence by virtue of its “only” logarithmically vanishing band gap. It is therefore worthwhile to investigate the behavior of the HF+MP2 energy and equilibrium volume of a simple metal such as sodium.

For the calculations of metallic sodium, the 3s state was treated as valence state and the equilibrium volume for a given k -point mesh was calculated in the same manner as outlined in Sec. 9.2.2. Only the direct contribution to the MP2 energy (dMP2) was calculated as this allows us to employ very dense k -point meshes (see Sec. 5.6). Figure 9.13 shows the dMP2 equilibrium volume as well as total energy of the face-centered-cubic sodium crystal with respect to the number of k -points used to sample the Brillouin zone in each direction. Our calculations show that the equilibrium volume as well as total energy diverge linearly with the number of k -points. It is not straightforward to explain the functional form of the divergence and we will leave its analytic derivation to future work. The numerical evidence, however, suggests that HF+MP2 diverges for atomization energies and lattice constants of metals as one would expect from the analytic results for the 3-D free electron gas.

9.2.6 Conclusions and Summary

In this section, we have presented results of canonical MP2 calculations for a set of typical semiconducting and insulating solid state systems. To investigate the accuracy of the MP2 method for bulk systems, lattice constants, atomization energies and band gaps were calculated and compared to experiment. For all three aspects, MP2 is an improvement over the HF method.

The errors in the calculated MP2 lattice constants are, with few exceptions, smaller than 0.5% and therefore smaller than for Hartree-Fock and commonly used density functionals. An important observation is that MP2 seems to overestimate the lattice constants of large band gap systems that are weakly polarizable, whereas for systems with a small band gap, which are strongly polarizable, MP2 tends to underestimate the lattice constants. The first error is most likely related to the neglect of particle-particle and hole-hole ladder diagrams, which are claimed to be relevant for weakly polarizable systems [22]. On the other hand, for strongly polarizable solids, higher order diagrams, specifically, the summation of all bubble diagrams included in the RPA, are important. These will reduce the polarizability and concomitantly the correlation energy [compare discussion following Eq.(7.17)]. At intermediate polarizabilities, MP2 works remarkably well and this seems to apply specifically to main group chemistry involving elements such as H, Li-F, and Na-Si.

For the MP2 atomization energies, a MAE of 230 meV/atom is found, which

constitutes a huge improvement over the corresponding HF mean absolute error of 1.59 eV/atom. The error is comparable to the error found for small molecules (MAE=144 meV/atom) [103]. A clear systematic trend in the error is lacking. Tentatively, however, we found that the error is smaller for ionic solids than for covalently bonded materials, but since atomization energies can be fortuitously good due to error cancellation between the atom and the solid, a more detailed analysis would require accurate reference values for the solids (and atoms). These are presently not available for solids. Nevertheless, the finding again suggests that MP2 tends to overcorrelate more strongly polarizable solids.

The MP2 QP band gaps improve (slightly) over the HF ones. Overall, the MP2 band gap results are somewhat disappointing, but in hindsight this is to be expected. The band gap is very sensitive to the long wavelength limit of the static polarizability [104], and the static polarizability is seriously overestimated for strongly polarizable solids, when second-order perturbation theory is used, as higher order bubble diagrams will decrease the polarizability. Overall, we indeed found that the error in the MP2 band gap is related to the (experimental) static dielectric constant. Results become unreliable if the static dielectric constant ϵ is larger than 3. For systems with ϵ larger than three, MP2 results in a pronounced overcorrection of the band gaps. This overcorrection is sometimes so strong that the MP2 band gaps become negative.

It might come as a surprise, that MP2 works so well for relative energies and lattice constants, despite failing for excitation energies. Certainly the method is rescued by the fact that total energies are integral quantities accounting for all excitations, whereas the band gap is very sensitive to low energy excitations (and the long wavelength limit), which are not accurately described for strongly polarizable solids applying second-order perturbation theory and HF orbitals.

Finally, we calculated the MP2 correlation energy as well as the equilibrium volume of metallic sodium. In agreement with previous reports [105] we find that the electronic correlation energy diverges in second-order perturbation theory. Like the correlation energy, the equilibrium volume exhibits a linear divergence with respect to the number of k -points in each direction, which makes MP2 useless for predicting properties of metals.

In summary, we find that MP2 is remarkably accurate for solid state systems involving main group elements. Overall, the accuracy seems to be comparable to the accuracy found for molecules. MP2 therefore is a viable alternative

to conventional density functional theory calculations, although, we emphasize that our present implementation is at least 2 to 3 *orders of magnitudes* more expensive than conventional density functional theory calculations. The present results, however, are sufficiently encouraging to attempt to improve the efficiency of the implementation and to evaluate more sophisticated many-electron techniques, such as coupled-cluster methods (specifically CCSD) for 3-D periodic solids. We expect that some deficiencies, such as the tendency to overcorrelate strongly polarizable solids and undercorrelate weakly polarizable solids, will be lifted by coupled-cluster methods.

Chapter 10

Second-order screened exchange

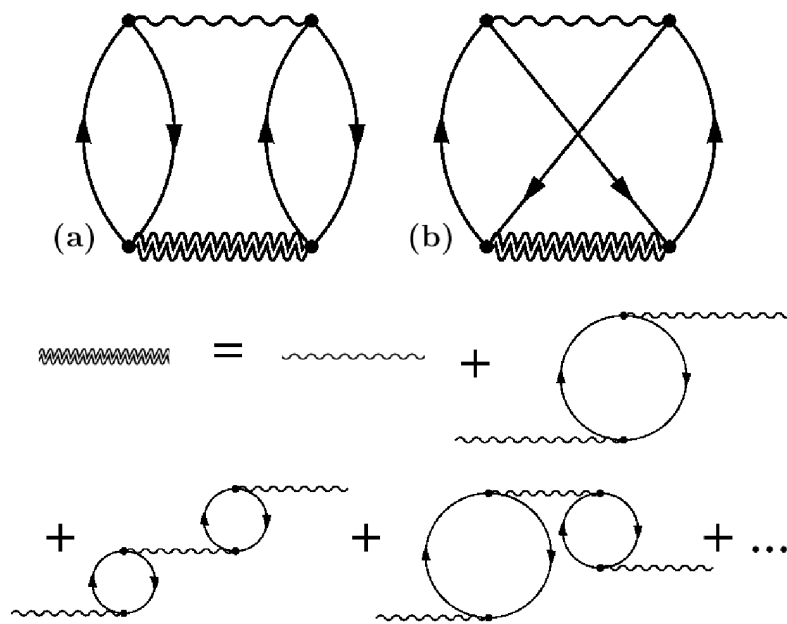


Figure 10.1: Diagrams corresponding to (a) direct-RPA correlation and (b) second-order screened exchange (SOSEX). The wiggly and double wiggly line represent the unscreened and screened Coulomb interaction, respectively.

In this chapter we include an exchange-like correlation term in the RPA [see Fig. 10.1(a)] that is fully compatible with the direct Coulomb correlation accounted for by the RPA, where compatibility here implies that for one-

Table 10.1: Core radii r_c for the PAW potentials used in the present work. If the core radii differ for specific quantum numbers, they are specified for each channel using subscripts.

	Valence	r_c [a.u.]	$E_{\text{cut}}^{\text{RPA+SOSEX}}$ [eV]
H	1s	1.0 _s 1.1 _{pd}	600
Li	1s2s	1.2 _s 1.5 _{pd}	600
C	2s2p	1.2 _s 1.5 _{pd}	460
N	2s2p	1.3 _s 1.5 _{pd}	1200
O	2s2p	1.2 _s 1.5 _{pd}	600
F	2s2p	1.1 _s 1.4 _{pd}	600
Ne	2s2p	1.4 _s 1.8 _{pd}	500
Na	2s2p3s	1.6 _s 2.0 _p 2.2 _d	360
Si	3s3p	1.5 _s 1.9 _{pd}	360

electron systems, the self-correlation error exactly vanishes. We call the term second-order *screened* exchange (SOSEX), since the corresponding diagram is reminiscent of the exchange-like diagram in second order perturbation theory, albeit with one Coulomb line replaced by a screened Coulomb interaction [see Fig. 10.1(b)]. We calculate absolute correlation energies of closed-shell atoms using Kohn-Sham orbitals and the RPA+SOSEX, CCSD and MP2 method. Moreover atomization energies of small molecules and solids will be calculated at the level of RPA+SOSEX.

10.1 Computational details

The pseudopotentials employed in the Vienna ab-initio simulation package (VASP) calculations were specifically optimized to yield accurate scattering properties well above the vacuum level and the potentials and technical details are identical to Ref. [46] and references therein. The core radii of the PAW potentials and the corresponding energy cutoffs employed in the RPA+SOSEX calculations are listed in Tab. 10.1. For the SOSEX calculations of solids a $3 \times 3 \times 3$ k -point mesh was used, whereas the slower converging RPA term was evaluated using an $8 \times 8 \times 8$ k -point mesh and the techniques explained

in Sec. 5.4.1 and Ref. [45]. All presented energy differences were carefully converged with respect to the energy cutoffs defining the basis set of the one-electron orbitals (parameter $E_{\text{cut}}^{\text{RPA}+\text{SOSEX}}$ in Tab. 10.1) as well as the auxiliary basis set used in the construction of the intermediate terms in Eqs. (D.2) and (D.3). Similar to the basis set for the one-electron orbitals, the size of the auxiliary basis set is determined by an energy cutoff E_χ , and all plane waves \mathbf{G} satisfying the equation

$$(\hbar^2/2m_e)|\mathbf{G}|^2 < E_\chi$$

are included in the basis set. To determine the infinite basis set limit, the correlation energy is determined at a set of different energy cutoffs E_χ and extrapolated to the infinite basis set limit, as already outlined in Sec. 9.1. To allow for an accurate extrapolation, we have chosen values for E_χ observing $E_\chi < 2/3E_{\text{cut}}^{\text{RPA}+\text{SOSEX}}$ (see Sec. 9.1 and Ref. [45]).

For molecules and atoms large cubic boxes were required in order to minimize the interaction between the periodic images. Eventually supercells with 9 Å length were employed for the calculation of the atoms and molecules.

For closed shell atoms, results were calculated using a modified version of the DALTON code [107]. The DALTON results were obtained by extrapolating to the infinite basis set limit using aug-cc-pCVXZ basis sets (X=D,T,Q,5,6). For the $1/X^3$ extrapolation procedure the corresponding two largest basis sets available at the EMSL Basis Set Library [108] were used (He: 5-6, Be: T-Q, Ne: Q-5, Ar: Q-5).

10.2 Closed-shell atoms

We restricted the study to closed shell atoms, since the DALTON coupled-cluster code only allows for the solution of the CCSD equation on top of a restricted open shell reference state (majority orbitals are equal to minority orbitals), whereas the restriction to doubles (CCD) and Kohn-Sham orbitals requires the use of an unrestricted open shell reference state for open shell systems. In Figures 10.2(a) and (b) we show the relative errors in the correlation energy evaluated using various approximations, with respect to the “exact” non-relativistic results [109]. Our CCSD values are close to the exact values, as one would expect. If only the direct terms are evaluated in the CCSD

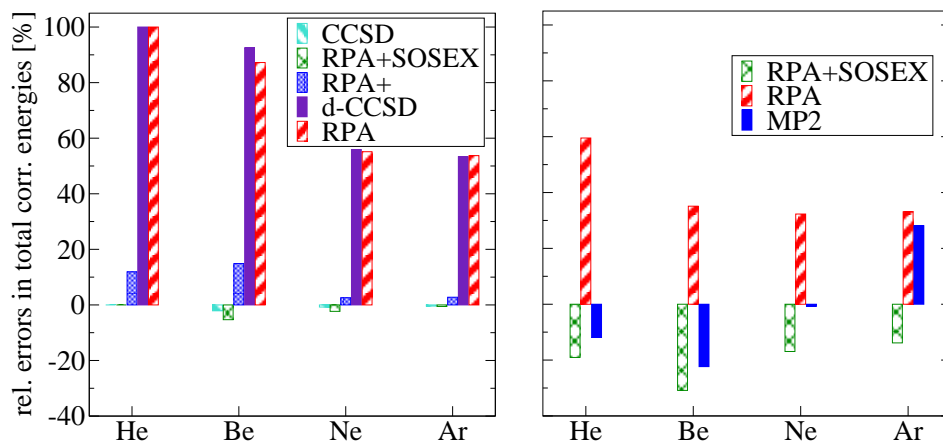


Figure 10.2: Relative errors of absolute correlation energies evaluated using various approximations with respect to “exact” non-relativistic results from Ref. [109]: CCSD, RPA+SOSEX, RPA+ (from Ref. [110]), CCSD using direct terms only (d-CCSD), and RPA. For CCSD, HF orbitals were used. On the left KS orbitals were used in the RPA calculations, whereas on the right HF orbitals were used for all calculations.

total energy expression (d-CCSD), the absolute correlation energy is overestimated by at least 50 %. The RPA using DFT orbitals yields correlation energies close to the d-CCSD, whereas inclusion of exchange (RPA+SOSEX) restores good agreement with the CCSD results albeit slightly underestimating the absolute correlation energy ($\Delta E \leq 250$ meV). Another simple means to correct the error of the RPA is to add a local DFT approximation for the lacking exchange-like correlation contribution (RPA+) [111], but clearly this approximation performs worse than an explicit evaluation of the SOSEX term.

The use of HF instead of Kohn-Sham orbitals reduces the RPA polarizabilities and therefore the correlation energies drastically, as shown in Fig. 10.2(b). The RPA and RPA+SOSEX now clearly underestimate the correlation energies obtained in d-CCSD and CCSD, respectively. This is related to the fact that HF orbitals yield too small polarizabilities and correlation energies, *if the particle-hole ladder diagrams are not included* (see Sec. 5.3). MP2 (and second-order Görling-Levy perturbation theory) can be regarded as a low order approximation to RPA+SOSEX, in which the amplitudes are determined by the first line in Eq. (5.127), or equivalently by replacing the

Table 10.2: Absolute correlation energies of the He, Be, Ne and Ar atom calculated using MP2, CCSD, d-CCSD, RPA and RPA+SOSEX. All units in milliHartree. Aug-cc-pCVXZ basis sets were used.

X(Basis set)	Reference	He 5	Be Q	Ne 5	Ar 5
MP2	HF	-36.53	-73.48	-375.93	-796.43
CCSD	HF	-41.57	-91.98	-375.93	-684.58
d-CCSD	HF	-83.15	-181.10	-590.46	-1045.69
RPA	HF	-65.49	-126.75	-495.15	-895.68
RPA+SOSEX	HF	-32.75	-64.56	-312.86	-585.60
RPA	DFT-PBE	-82.61	-175.76	-583.58	-1040.84
RPA+SOSEX	DFT-PBE	-41.30	-89.23	-369.23	-679.31

screened Coulomb interactions in Fig. 10.1 by a bare Coulomb interaction. MP2 works quite well using HF orbitals for 1st and 2nd row elements, first slightly underestimating the correlation energy, getting it right for Ne, but finally significantly overestimating the absolute correlation energy for Ar. This is related to the fact that heavier atoms are more polarizable, and any low order approximation, even evaluated using HF orbitals, tends to overestimate the correlation energy. Table 10.2 summarizes the non-extrapolated correlation energies of the closed-shell atoms.

10.3 Solids and molecules

At this point, our conclusion is that Kohn-Sham orbitals allow for a reasonably accurate evaluation of the total correlation energy of atoms using RPA+SOSEX (5 kcal/mol). Our second reference system is the jellium electron gas, for which results have been obtained by Freeman [33]. Freeman's calculations were based on free-electron orbitals and one-electron energies, which are exactly identical to Kohn-Sham orbitals and one-electron energies, and clearly his results agree exceedingly well with the Quantum-Monte Carlo (QMC) simulations obtained three years later by Ceperley and Alder [3] (see Fig. 10.3). As such, Freeman's data are the first reliable estimate of the jellium

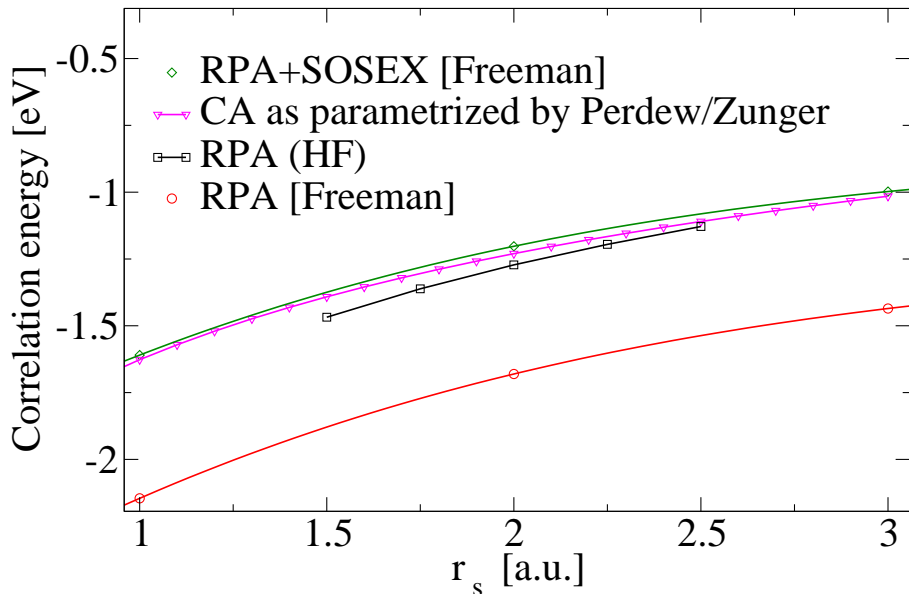


Figure 10.3: Correlation energy of jellium evaluated using various approximations: exact from quantum Monte-Carlo [Ref. [3]], RPA and RPA+SOSEX values are from Freeman [Ref. [33]] and were obtained using Kohn-Sham orbitals and one-electron energies, whereas the RPA(HF) values were calculated using HF orbitals and one-electron energies using VASP.

correlation energy, but seem to have been largely disregarded. In Fig. 10.3, we have included our numerical RPA values for Hartree-Fock orbitals. Compared to the Kohn-Sham reference state, Hartree-Fock introduces a logarithmic singularity at the Fermi-level and increases the band width of jellium significantly. This combined effect reduces the polarizability and concomitantly the correlation energy drastically to values that are close to the exact QMC values. This agreement, however, is fortuitous: (i) correlation effects from exchange-like terms are real and must be accounted for and (ii) we did not observe systematic error cancellation for atoms as exemplified in Fig. 10.2(b). In passing, we note that self-consistent *GW*-RPA calculations, disregarding any correlation effects from the exchange-like terms, yield good total correlation energies for the jellium as well [112]. This is related to the fact that self-consistent *GW* calculations increase the band-width in very much the same manner as a HF reference state [113] so that agreement with exact QMC correlation energies

Table 10.3: Lattice constants and atomization energies of C, Si, SiC, LiH and LiF evaluated using RPA, RPA+ (from Ref. [24]), RPA+SOSEX and experimental values. All experimental values have been corrected for zero point vibrations.

	$a_0(\text{\AA})$				$E_{\text{at}}(\text{eV/atom})$			
	RPA	RPA+	SOSEX	EXP	RPA	RPA+	SOSEX	EXP
C	3.572	3.578	3.552	3.553	7.01	6.94	7.43	7.55
Si	5.431	5.445	5.426	5.421	4.39	4.33	4.68	4.68
SiC	4.366	4.374	4.341	4.346	6.03	5.96	6.39	6.48
LiH	3.983	4.001	3.989	3.979	2.41	2.39	2.46	2.49
LiF	3.998	4.010	3.955	3.972	4.22	4.15	4.37	4.46

is obtained as well— certainly fortuitously (RPA[HF] \approx RPA[GW] \approx QMC, see also Ref. [30]).

As a last case, we have calculated the lattice constants and atomization energies of solids (C, Si, SiC, LiH and LiF [see Tab. 10.3]) as well as the atomization energies of the HF, H₂O, Na₂, Si₂, N₂ and Ne₂ molecules (see Tab. 10.4) using the RPA+SOSEX and VASP. For the atomization energies of the molecules the same structures as in Ref. [28] were employed and the Na₂ molecule was calculated at the experimental bond length of 3.079 Å. Compared to Ref. [46] we have corrected the experimental lattice constants of the solids for zero-point vibration effects, by evaluating the phonon dispersion relations in the harmonic approximation at each volume [118]. We now clearly see that the RPA tends to overestimate the lattice constants for C, Si, SiC and LiF. The inclusion of SOSEX usually decreases the lattice constants, which we interpret to result from a reduction of the Pauli repulsion. On the other hand, the RPA+, which attempts to model the effects of SOSEX by a local correlation energy functional, increases the lattice constants even further, worsening agreement with experiment [24].

At the RPA+SOSEX level, we are able to obtain spectacular agreement with experiment for the lattice constants (mean absolute relative error—MARE: 0.2 %). For the atomization energies of the solids the improvements are also significant after inclusion of SOSEX (MAE: 70 meV/atom). The atomization

Table 10.4: Atomization energies of the HF, H₂O, Na₂, Si₂, N₂ and Ne₂ molecules evaluated using RPA, RPA+SOSEX and experimental values. All experimental values have been corrected for zero point vibrations.

	E_{at} (eV/atom)		
	RPA	SOSEX	EXP
HF	2.88 ^a	3.01	3.06 ^b
H ₂ O	3.23 ^a	3.29	3.36 ^c
Na ₂	0.26	0.31	0.36 ^d
Si ₂	1.52 ^a	1.58	1.63 ^c
N ₂	4.84 ^a	4.65	4.94 ^c
Ne ₂	0.00022 ^a	0.00062	0.00173 ^e

^a Ref. [28], ^b Ref. [114], ^c Ref. [115], ^d Ref. [116], ^e Ref. [117]

energies of the molecules exhibit a similar accuracy when SOSEX is taken into account, except for the case of N₂, which we believe to result from the neglect of higher order effects such as triples in the coupled-cluster expansion. In fact, our RPA+SOSEX results are remarkably close to the CCSD results of Bak et. al for HF (3.02 eV/atom), H₂O (3.31 eV/atom) and N₂ (4.68 eV/atom) [119]. Although it is well known that CCSD does not allow to predict total energy differences with chemical accuracy, the important point is that a wave function based method (RPA+SOSEX) can yield an accuracy comparable to CCSD but at a significantly lower computational complexity and cost.

10.4 The G2-1 test set

After the results from the previous sections were published, Paier *et al.* calculated 55 atomization energies of small molecules of the G2-1 test set using RPA+SOSEX [120]. Figure 10.4 shows the error distribution of the 55 G2-1 atomization energies for the RPA and RPA+SOSEX. Clearly, RPA+SOSEX lifts the tendency of the RPA to underbind molecules. The MAE of the atomization energies compared to experiment of the G2-1 test set is reduced from 10 kcal/mol in the RPA to 5 kcal/mol in RPA+SOSEX.

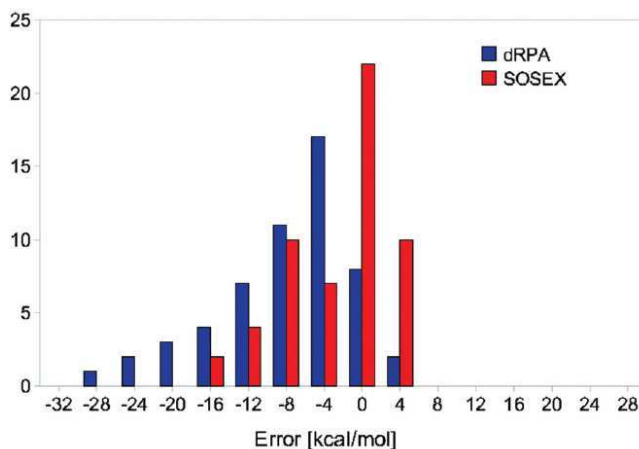


Figure 10.4: Error distribution of the 55 G2-1 atomization energies for RPA and SOSEX from Ref. [120].

10.5 Conclusions and Summary

RPA+SOSEX seems to be a promising approximation for absolute correlation energies and changes in the correlation energy in particular for solids. Our present implementation relies on Kohn-Sham PBE orbitals, although, for consistency, the orbitals should be determined within an optimized-effective-potential framework, ideally using RPA+SOSEX or at least the RPA. This, however, is left for future work. Since RPA+SOSEX is exactly self-correlation free for any one-electron system, it will describe any one-electron system exactly, if Hartree-Fock orbitals are used, and the problems described in Ref. [106] for H_2^+ dissociation are not present. Nevertheless, the use of PBE orbitals introduces a small error, since the PBE orbitals suffer from selfinteraction errors.

It is certainly puzzling that Kohn-Sham wave functions yield amplitudes that must in some way resemble the true CCSD amplitudes evaluated using HF orbitals, despite the neglect of all particle-hole, particle-particle and hole-hole ladder diagrams present in the conventional CCSD method. This brings us back to an observation we have made before [104]: the Kohn-Sham DFT band gaps are much smaller than the real quasiparticle band gaps, but this band gap error is to a large extent corrected for by the *neglect of diagrams*, that describe the electrostatic interaction between electrons and holes (see Sec. 5.3). For PBE orbitals, this cancellation effect must work remarkably well in the two

extremes we have considered here: jellium and atoms.

The present work also clarifies some important issues that are widely disregarded in the solid state community: correlation effects from the exchange-like terms are exceedingly important for the total energy, and modeling this term by a local DFT like term does not seem to be accurate (RPA+).

Chapter 11

Natural orbitals and CCSD

The scaling of the computational effort of our CCSD implementation with respect to the system size is very unfavorable [$\mathcal{O}(N^6)$]. In this chapter, we reduce the computational cost by introducing natural orbitals that allow for reducing the number of virtual orbitals without sacrificing accuracy. Natural orbitals (NOs) can be obtained by diagonalizing the virtual-virtual orbital block of a density matrix, calculated at the level of second-order Møller-Plesset perturbation theory (MP2) [see Sec. 6 and Eqs. (6.6) and (6.8)] [49, 123, 124, 50]. Eigenvectors and eigenvalues of this density matrix are called (approximate) MP2 natural orbitals and occupation numbers, respectively.

Natural orbitals allow to reduce the virtual orbital space of atoms and molecules by about half without significantly compromising accuracy if gaussian type orbitals (GTOs) are used [123, 124]. In general, however, the reduction is related to linear dependencies in the density matrix and much larger reductions are possible if an *inefficient* basis set is used to capture correlation effects.

Plane waves (PWs) constitute fairly efficient basis functions for solid state systems. They form a complete set, where the number of basis functions can be controlled by a single parameter, the PW energy cutoff. However, one major shortcoming is that the PW basis set is independent of the atomic species and its location. In calculations of open structures, where the electron density is localized around a few atomic sites, this feature of the PW basis set becomes unfavorable when compared to the use of GTOs. Even atoms or small molecules in a large box require several thousands of virtual canonical orbitals. A large part of this virtual orbital space is unnecessary because it describes

regions in the vacuum far away from the nucleus where the true many-electron wave function vanishes. In the following, it is shown that one can lift this problem by means of natural orbitals that are calculated at the level of MP2 or in an even more approximate fashion.

11.1 Computational details

The density matrix in Eq. (6.6) is calculated using the Vienna *ab-initio* simulation package (VASP) in the framework of the PAW method. For the evaluation of the two-electron-four-orbital integrals $\langle ij|ab\rangle$ two basis sets are used: (i) the basis set for the one-electron orbitals i, j, a and b , (ii) as well as the auxiliary basis set used in the construction of the overlap between two orbitals i and a (see Sec. 8.3 for details). These basis sets are determined by energy cutoffs E_{cut} and E_{χ} , respectively, and all PWs \mathbf{G} satisfying the equation

$$(\hbar^2/2m_e)|\mathbf{G}|^2 < E_{\chi/\text{cut}}$$

are used. For the evaluation of γ_{ab}^{MP2} [see Eq. (6.6)] we set E_{χ} close to E_{cut} because we find a fast convergence of the natural orbitals with respect to E_{χ} . The correlation energy in the complete basis set limit is extrapolated by systematically increasing E_{χ} as outlined in Sec. 9.1.

Natural orbitals with an occupation number close to zero are expected to contribute only little to the correlation energy [49]. Therefore we introduce a threshold, ξ , that defines a subspace of the natural orbitals by truncating them according to their occupation number. Only natural orbitals with an occupation number *larger than* ξ are included in this subspace.

Unlike HF orbitals, natural orbitals do not diagonalize the Fock matrix [see Eq. (4.10)]. Therefore non-canonical formulations of the employed correlated methods would be required. We work around the non-canonical implementations by carrying out the following procedure subsequent to the underlying Hartree-Fock (HF) calculation: (i) calculate the natural orbitals (NOs), (ii) order the natural orbitals according to their occupation numbers [eigenvalues of the density matrix defined in Eq. (6.6)], (iii) recalculate the Fock matrix [see Eq. (4.10)] in the basis of NOs, and (iv) diagonalize (“canonicalize”) in a subspace of this Fock matrix that is defined by the threshold ξ . These “canonicalized” orbitals diagonalize the subspace and can be used in a subsequent canonical wave function based correlated calculation. We stress that

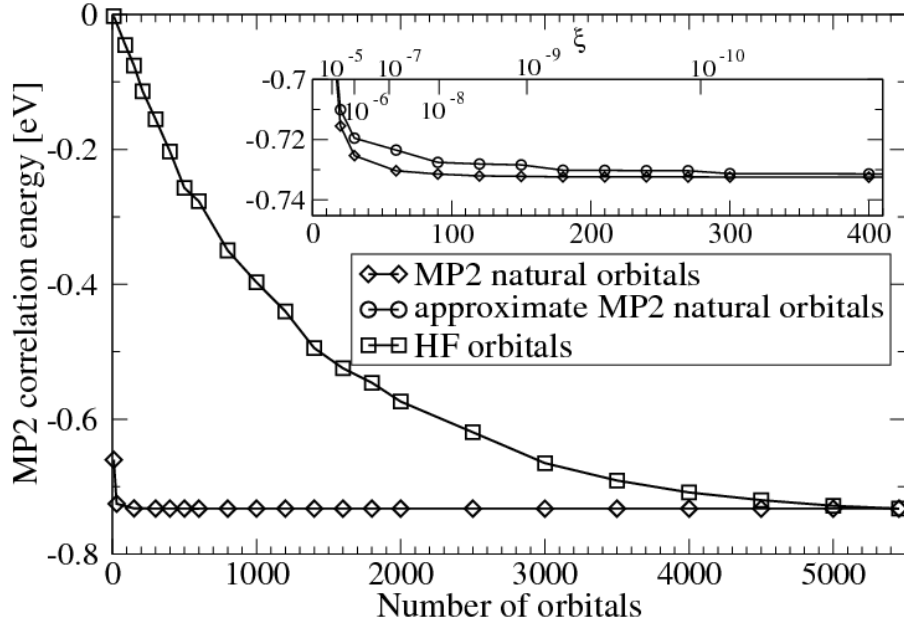


Figure 11.1: Convergence of the MP2 correlation energy of the Li atom in a $6 \times 6 \times 6 \text{ \AA}^3$ box with respect to the number of natural and HF orbitals per spin-channel. The inset shows the convergence on a different scale. The top x-axis in the inset shows the occupation number threshold, ξ , of the MP2 natural orbitals for the spin-up channel.

the correlation energy is not changed by the diagonalization in the subspace of NOs.

11.2 Li atom and LiH bulk using natural orbitals

As a first example, we study the convergence of the MP2 correlation energy of a Li atom in the spin polarized state in a $6 \times 6 \times 6 \text{ \AA}^3$ box. The correlation energy was not extrapolated to the complete basis set limit; a fixed kinetic energy cutoff $E_\chi = 400 \text{ eV}$ was used. The kinetic energy cutoff for the one-electron

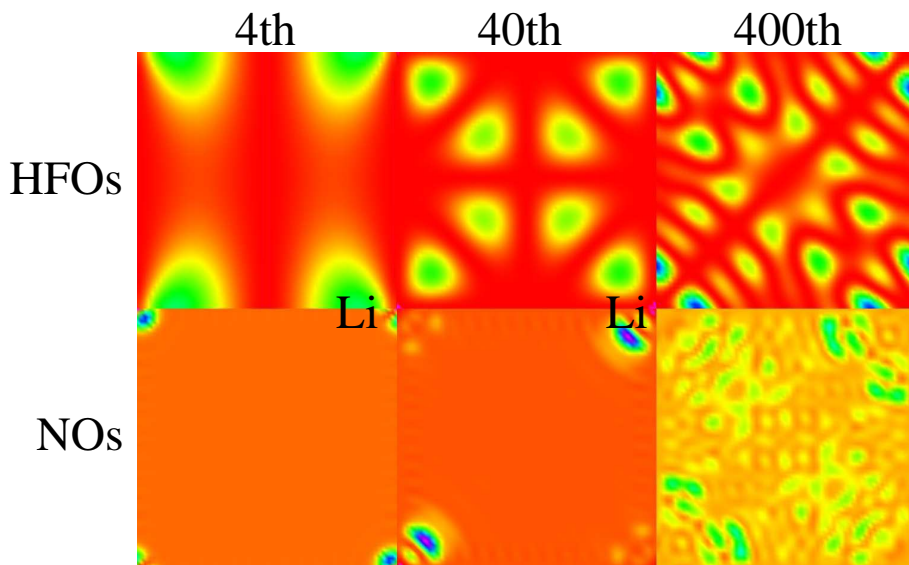


Figure 11.2: Charge densities of the Hartree-Fock orbitals (HFOs) in the top row and natural orbitals (NOs) in the bottom row of a Li atom in a $6\times 6\times 6$ \AA^3 box. The 4th, 40th and 400th orbitals are plotted.

orbitals was set to $E_{\text{cut}} = 500$ eV. Figure 11.1 shows the MP2 correlation energy of the Li atom with respect to the number of orbitals per spin channel. For the given cutoff E_{cut} and box size, 5450 orbitals span the complete space of one-electron Hartree-Fock orbitals. The convergence of the correlation energy with respect to the number of HFOs is extremely slow. Even 4000 HFOs yield an MP2 correlation energy that deviates by more than 10 meV from the correlation energy obtained using the full space (733 meV). In contrast, 30 natural orbitals (NOs) already suffice to obtain an agreement that lies within 10 meV of the converged value. The top axis of the inset in Fig. 11.1 shows the corresponding occupation number threshold, ξ , of the MP2 natural orbitals. We find that 30 natural orbitals correspond to an occupation number threshold of 10^{-6} . The occupation numbers quickly decay to zero, which illustrates the insignificance of the neglected natural orbitals and the “redundancy” present in the PW basis set in the description of many-electron properties. Approximate MP2 natural orbitals [eigenvectors of the approximate density matrix given by Eq. (6.8)] reduce the convergence rate only slightly (see inset of Fig. 11.1). In fact, both types of natural orbitals allow for reducing the number of virtuals

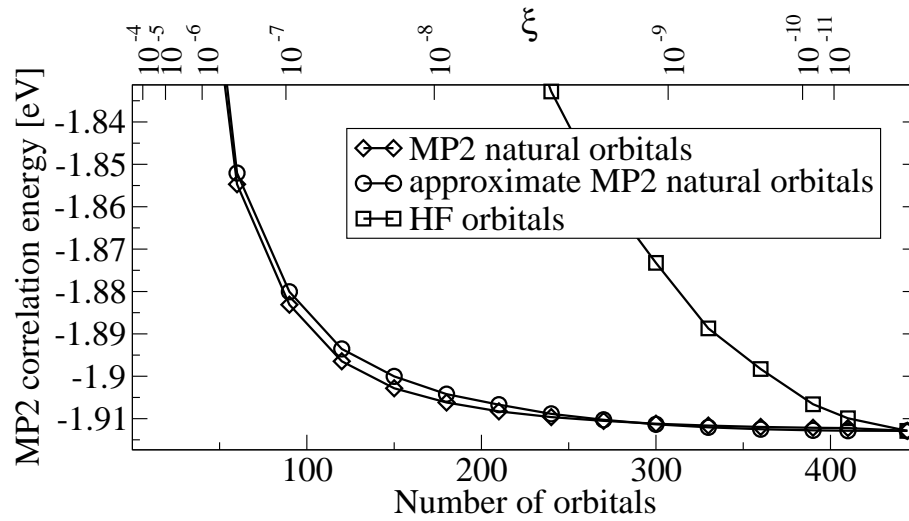


Figure 11.3: Convergence of the MP2 correlation energy of the LiH solid using a $4 \times 4 \times 4$ k -point mesh with respect to the number of natural and HF orbitals per k -point. The top x-axis shows the occupation number threshold, ξ , of the MP2 natural orbitals at the Γ -point.

compared to Hartree-Fock by at least an order of magnitude.

Figure 11.2 shows the charge densities of the 4th, 40th and 400th natural, and Hartree-Fock orbital of a Li atom in a $6 \times 6 \times 6 \text{ \AA}^3$ box. Hartree-Fock orbitals and natural orbitals are ordered by their increasing one-electron HF eigenvalues and decreasing occupation numbers respectively. The HF orbitals become essentially plane waves at higher energies and greater band indices, since the kinetic energy operator dominates at sufficiently high energies. The natural orbitals with large occupation numbers maximize the overlap with the occupied orbitals, whereas the natural orbitals with small occupation numbers exhibit only very little density at the Li atom, as can be clearly seen for the 400th NO.

Figure 11.3 shows the convergence of the MP2 correlation energy of the face-centered-cubic LiH crystal with a unit cell volume of 17.03 \AA^3 . The first Brillouin zone was sampled using a $4 \times 4 \times 4$ k -point mesh and the same cutoffs as for the Li atom were employed ($E_{\chi} = 400 \text{ eV}$, $E_{\text{cut}} = 500 \text{ eV}$). In the case of solids the reduction of the virtual orbital space using natural orbitals is less significant than for a single atom in a box. This is not unexpected because

Table 11.1: Atomization energy of the LiH molecule using natural and HF orbitals. Plane-waves (PWs) as well as aug-cc-pVXZ(X=T,Q) basis sets were used in the calculations.

	This work	Ref. [87]	GAMESS
Orbitals	NOs	HFOs	HFOs
Basis set type	PWs	PWs	aug-cc-pVXZ
ΔE^{HF}	1.084	1.084	1.085
ΔE_c^{MP2}	0.823	0.822	0.818
ΔE_c^{CCSD}	1.039		1.034

in contrast to an atom in a box, the electrons of the solid are delocalized over the entire unit cell and almost all degrees of freedom supplied by the plane wave basis set are required to describe the many-electron wave function. Nevertheless it is possible to remove about half of the HF virtual orbital space without introducing an error larger than 10 meV. The approximate and exact MP2 natural orbitals show a very similar convergence rate. The top axis in Fig. 11.3 shows the corresponding occupation number thresholds, ξ , for the MP2 natural orbitals. An error smaller than 10 meV in the correlation energy can be achieved by including all NOs with $\xi = 10^{-8}$.

11.3 The H₂ and LiH test using CCSD and natural orbitals

As a first test of our CCSD implementation with natural orbitals we calculate the dissociation energy of a H₂ molecule with a bond length of 0.75 Å, using 80 natural orbitals. We obtain a HF and CCSD contribution to the dissociation energy of 3.619 eV and 1.112 eV, respectively. The resulting dissociation energy of 4.731 eV agrees perfectly with the experimental value of 4.73 eV [114].

As a second test of our implementation we have calculated the dissociation energy of the LiH molecule at the level of MP2 as well as CCSD using NOs. The bond length was set to 2.042 Å. Table 11.1 summarizes the HF, MP2 as well as CCSD contributions to the atomization energies of the LiH molecule. The column on the right lists the results that have been obtained using the

Table 11.2: Contributions of the MP2 correlation energy to the atomization energy of the LiH crystal calculated according to Eq. (11.1).

n_{NOs}	n_3	n_4	ΔE_c^{MP2}
192	16	16	1.192
256	16	16	1.195
192	32	16	1.203
192	48	16	1.189
192	54	16	1.189
192	64	16	1.205
192	54	32	1.185
192	54	48	1.187

GAMESS code [94]. The middle column summarizes the HF and MP2 results that were calculated using VASP and Hartree-Fock orbitals in Sec. 9.1 and Ref. [87]. The column on the left summarizes the HF, MP2 as well as CCSD contributions obtained using VASP and NOs. VASP and GAMESS results agree to within a few meV. The discrepancy between the VASP MP2 results that were obtained using NOs and HFOs is 1 meV and originates from the truncation of the virtual orbital space. 200 and 58 NOs were used in the calculations of the molecule and atom, respectively. This corresponds to a ξ of approximately 10^{-7} . The agreement of the CCSD results calculated using VASP with the ones obtained using the GAMESS code is very good as well, and both results do not deviate by more than 5 meV. This is excellent considering that VASP employs pseudopotentials (more precisely the PAW method) and is not a conventional GTO all-electron code.

As a last application we calculate the atomization energy of the LiH solid at the level of MP2 as well as CCSD. Even with natural orbitals it would be impossible to perform a CCSD calculation of the LiH crystal with a k -point mesh denser than $2 \times 2 \times 2$, because of the large number of virtual orbitals and the unfavorable scaling of the computational effort of our CCSD implementation with respect to the system size. Therefore we calculate the correlation energy, \hat{E}_c , of a solid for a desired $(n_k \times n_k \times n_k)$ k -point mesh and n_{full} orbitals

Table 11.3: HF, MP2 and CCSD contributions to the atomization energy of the LiH crystal using different orbitals compared to quantum chemical calculations of LiH Clusters from Ref. [125]. The MP2 contribution to the atomization energy of the LiH crystal from Ref. [87] corresponds to a calculation using a $4 \times 4 \times 4$ k -point mesh.

	This work	Ref. [87]	Ref.[125]
Orbitals	NOs	HFOs	HFOs
ΔE^{HF}	3.583	3.583	3.589
ΔE_c^{MP2}	1.187	1.188	1.182
ΔE_c^{CCSD}	1.326		1.329

per k -point using the following approximation:

$$\hat{E}_c(n_k \times n_k \times n_k, n_{\text{full}}) = E_c(2 \times 2 \times 2, n_{\text{full}}) + \sum_{i=3}^{n_k} C_i. \quad (11.1)$$

$E_c(2 \times 2 \times 2, n_{\text{full}})$ is the calculated correlation energy using a $(2 \times 2 \times 2)$ k -point mesh and a converged basis set. C_i are correction terms that account for the difference between $(2 \times 2 \times 2)$ and denser k -point grids and are calculated as

$$C_i = E_c(i \times i \times i, n_i) - E_c((i-1) \times (i-1) \times (i-1), n_i). \quad (11.2)$$

Evidently Eq. (11.1) becomes exact for $n_i \rightarrow n_{\text{full}}$, but typically n_i is chosen smaller than n_{full} and decreases with an increasing number of k -points, i , in each direction. This approach is similar to the progressive downsampling technique of Ohnishi et al. in Ref. [126] and both techniques rely on the observation that the long range behavior of the polarizability depends mostly on the low-lying excitations. In practice, we find a fast convergence of the correlation energy with respect to n_i . Moreover we calculate $E_c(2 \times 2 \times 2, n_{\text{full}})$, using n_{NOs} natural orbitals at each k -point. Table 11.2 summarizes the convergence of the MP2 atomization energy with respect to n_{NOs} and n_i for all i . We find that the convergence with respect to n_i is fairly noisy. From the noise, we estimate an error bar of approximately 10 meV for the correlation energy given by Eq. (11.1). However, we find that it suffices to use $n_{\text{NOs}} = 192$, $n_3 = 54$ and $n_4 = 32$. These settings are then employed in a CCSD calculation. Table 11.3 summarizes the resulting HF, MP2 and CCSD contributions

to the atomization energy of the LiH crystal. The results are again compared to previous calculations obtained using HFOs and quantum chemical calculations using the incremental approach and LiH clusters [125]. The agreement between Ref. [87] and Ref. [125] was already discussed in Sec. 9.1. We find that Eq. (11.1) works reliably for calculating the MP2 contribution to the atomization energy of the LiH crystal. Our MP2 results deviate by less than 10 meV from Sec. 9.1 and Ref. [87]. Moreover our CCSD results are in very good agreement with Ref. [125] which gives us confidence of the correct implementation of the CCSD code for periodic boundary conditions.

11.4 Conclusions and Summary

In summary, we have shown that MP2 natural orbitals allow for a tremendous reduction of the virtual orbital space, compared to HF orbitals for calculations of single atoms or molecules in a box using a PW basis set. This allows for calculations of atoms and small molecules using highly accurate quantum-chemical methods such as CCSD in a PW basis set. In the case of solids, the virtual orbital space can be reduced approximately by half without compromising the accuracy significantly. Note that in CCSD calculations, a reduction of the virtual orbital space by half corresponds to a speed-up of an order of magnitude. Although the computational cost of evaluating natural orbitals scales as $\mathcal{O}(N^5)$, we can approximate the MP2 NOs by a simpler expression that scales only as $\mathcal{O}(N^4)$. The approximated NOs perform only slightly worse than the exact MP2 NOs. This even allows us to reduce the computational cost of MP2 calculations for large systems. Moreover natural orbitals will not only help in expanding the applicability of our MP2 or CCSD implementation; many other correlated methods that are implemented in a PW basis will benefit as well. It is straightforward to apply the presented procedures to other methods such as the Random phase approximation plus second-order screened exchange [101] or *GW*-BSE [127].

Chapter 12

Conclusions and Summary

This thesis is devoted to the implementation and evaluation of the following three wave function based methods to treat electron correlation in solid state systems under periodic boundary conditions:

1. second-order Møller-Plesset perturbation theory (MP2),
2. random phase approximation plus second-order screened exchange (RPA+SOSEX),
3. and coupled-cluster singles and doubles theory (CCSD).

In the first part (chapters 1-8), a brief theoretical review of these methods was given. The second part is split into three chapters that address MP2, RPA+SOSEX and CCSD results (chapters 9, 10 and 11, respectively).

Section 9.1 outlines important technical procedures that are required to obtain converged correlation energies with respect to the employed basis set and Brillouin zone sampling.

Section 9.2 summarizes structural and energetic properties that have been calculated using our MP2 implementation for a small test set of 13 solid state systems. It is shown that the mean absolute relative errors (MARE) of the MP2 lattice constants and bulk moduli are 0.46% and 4.1%, respectively. As such, MP2 clearly outperforms Hartree-Fock, which exhibits a MARE of 1.31% and 7.9% for the lattice constants and bulk moduli, respectively. For the MP2 atomization energies, a MAE of 230 meV/atom is found, which constitutes a huge improvement over the corresponding HF mean absolute error of 1.59 eV/atom as well. Compared to DFT-PBE, MP2 improves upon lattice constants and bulk moduli, but not upon atomization energies. We find that

the MP2 band gaps are only accurate for systems with a dielectric constant smaller than 3. In general MP2 tends to overcorrelate strongly screening materials and undercorrelate weakly screening materials. This trend is reflected in the errors of the MP2 band gaps, lattice constants and atomization energies for systems with a large dielectric constant. In addition we have presented numerical evidence that the MP2 energy diverges for metallic systems.

Chapter 10 summarizes results for total correlation energies of atoms and the homogeneous electron gas using RPA and RPA+SOSEX. Furthermore our RPA+SOSEX implementation was employed to calculate atomization energies of 5 solids and 6 molecules. SOSEX corrects for the “self-correlation” error in the RPA. As such, RPA+SOSEX reduces the error in the total RPA correlation energies by around 30% for atoms and the free electron gas. Moreover RPA+SOSEX yields highly accurate results for lattice constants and atomization energies. We are able to obtain spectacular agreement with experiment for the lattice constants (MARE: 0.2 %). For the atomization energies of the solids the accuracy is also excellent (MAE: 70 meV/atom). RPA+SOSEX clearly outperforms DFT-PBE, HF, MP2 and RPA in terms of accuracy for lattice constants and atomization energies. Although RPA+SOSEX is a new method that requires more testing, our preliminary results and those from Ref. [120] indicate that RPA+SOSEX might achieve the same accuracy as CCSD with a much smaller computational complexity and effort. The computational effort of our MP2 and RPA+SOSEX implementations scale as $\mathcal{O}(N^5)$, where N is a measure of the system size.

Chapter 11 addressed natural orbitals and first tests of our coupled-cluster singles and doubles code for solid state systems. We have shown that natural orbitals at the level of second-order Møller-Plesset perturbation theory allow to achieve a much faster convergence of the correlation energy with respect to the number of virtual orbitals. The virtual orbital space can be reduced by about half without losing significant accuracy. This enables us to perform the first calculations of three dimensional solids under periodic boundary conditions at the CCSD level. We have calculated the CCSD atomization energies of the LiH molecule and solid and shown that our implementation yields results that agree well with quantum chemical calculations.

Appendix A

Slater-Condon rules

Slater-Condon rules express the result of integrals over one- and two-body operators between identical or different Slater determinants constructed of orthonormal orbitals ψ_i in terms of the individual orbitals. In the following one- and two-body operators are denoted by $\mathcal{O}_1(\mathbf{r}_1)$ and $\mathcal{O}_2(\mathbf{r}_i, \mathbf{r}_j)$, respectively. We define the one- and two-body operators to be the one-body Hamiltonian and the two-electron Coulomb operator:

$$\mathcal{O}_1 = \sum_i^N h(\mathbf{r}_i),$$
$$\mathcal{O}_2 = e^2 \sum_i^N \sum_{i < j}^N \frac{1}{|\mathbf{r}_i - \mathbf{r}_j|}.$$

We suppose that the Slater determinants Ψ^I are constructed from a set of orthonormal orbitals $\{\psi_1, \dots, \psi_i, \dots, \psi_N\}$ according to

$$\Psi^I(\mathbf{r}_1, \dots, \mathbf{r}_N) = |\psi_1, \dots, \psi_i, \dots, \psi_N\rangle = \frac{1}{\sqrt{N!}} \left| \begin{pmatrix} \psi_1(\mathbf{r}_1) & \dots & \psi_N(\mathbf{r}_1) \\ \dots & \dots & \dots \\ \psi_1(\mathbf{r}_N) & \dots & \psi_N(\mathbf{r}_N) \end{pmatrix} \right|.$$

The Slater-Condon rules distinguish between following cases:

- Case 1: Both Determinants are identical

$$\Psi^I = \Psi^{\text{II}}$$
$$\langle \Psi^I | \mathcal{O}_1 | \Psi^{\text{II}} \rangle = \sum_m^N \langle \psi_m | h | \psi_m \rangle = \sum_m^N \int d\mathbf{r}_1 \psi_m^*(\mathbf{r}_1) h(\mathbf{r}_1) \psi_m(\mathbf{r}_1)$$

$$\langle \Psi^I | \mathcal{O}_2 | \Psi^II \rangle = \frac{1}{2} \sum_m^N \sum_n^N \langle \psi_m \psi_n | | \psi_m \psi_n \rangle$$

where

$$\langle \psi_l \psi_m | | \psi_n \psi_o \rangle = e^2 \int d\mathbf{r}_1 \int d\mathbf{r}_2 \left[\frac{\psi_l^*(\mathbf{r}_1) \psi_m^*(\mathbf{r}_2) \psi_n(\mathbf{r}_1) \psi_o(\mathbf{r}_2)}{|\mathbf{r}_1 - \mathbf{r}_2|} - \frac{\psi_l^*(\mathbf{r}_1) \psi_m^*(\mathbf{r}_2) \psi_o(\mathbf{r}_1) \psi_n(\mathbf{r}_2)}{|\mathbf{r}_1 - \mathbf{r}_2|} \right]$$

- Case 2: Both determinants differ by one orbital

$$\Psi^I = |\psi_1, \dots, \psi_m, \dots, \psi_N\rangle$$

$$\Psi^{II} = |\psi_1, \dots, \psi_p, \dots, \psi_N\rangle$$

$$\langle \Psi^I | \mathcal{O}_1 | \Psi^{II} \rangle = \langle \psi_m | h | \psi_p \rangle$$

$$\langle \Psi^I | \mathcal{O}_2 | \Psi^{II} \rangle = \sum_n^N \langle \psi_m \psi_n | | \psi_p \psi_n \rangle$$

- Case 3: Both determinants differ by two orbitals

$$\Psi^I = |\psi_1, \dots, \psi_m, \psi_n, \dots, \psi_N\rangle$$

$$\Psi^{II} = |\psi_1, \dots, \psi_p, \psi_q, \dots, \psi_N\rangle$$

$$\langle \Psi^I | \mathcal{O}_1 | \Psi^{II} \rangle = 0$$

$$\langle \Psi^I | \mathcal{O}_2 | \Psi^{II} \rangle = \langle \psi_m \psi_n | | \psi_p \psi_q \rangle$$

If the determinants differ by more than two orbitals, the integrals of the one- and two-body operator vanish.

Appendix B

Direct contributions to the MP2 QP energy

In this appendix we give a formal proof that starting from a truncated inverse Dyson-like equation in the GW formalism one obtains formally the expression for the “direct” contribution to the MP2 quasiparticle energies, $\epsilon_{\mathbf{n}}^{\text{dMP2}}$.

The exchange and correlation contribution to the GW QP energy $\epsilon_{n,k}^{GW}$ is obtained from Eq. (7.18):

$$\begin{aligned} \epsilon_{n,\mathbf{k}}^{GW}(\omega) &= \langle \psi_{n,\mathbf{k}} | \Sigma(\omega) | \psi_{n,\mathbf{k}} \rangle \\ &= \frac{1}{\Omega} \sum_{\mathbf{q}, \mathbf{G}, \mathbf{G}'} \sum_{n'} \frac{i}{2\pi} \int_{-\infty}^{\infty} d\omega' W_{\mathbf{q}}(\mathbf{G}, \mathbf{G}', \omega') \langle \psi_{n,\mathbf{k}} | e^{i(\mathbf{q}+\mathbf{G})\mathbf{r}} | \psi_{n',\mathbf{k}-\mathbf{q}} \rangle \\ &\quad \times \left\langle \psi_{n',\mathbf{k}-\mathbf{q}} | e^{-i(\mathbf{q}+\mathbf{G}')\mathbf{r}'} | \psi_{n,\mathbf{k}} \right\rangle \frac{1}{\omega - \omega' - \epsilon_{n',\mathbf{k}-\mathbf{q}} + i\eta \text{sgn}(\epsilon_{n',\mathbf{k}-\mathbf{q}} - \mu)}. \end{aligned} \quad (\text{B.1})$$

Here \mathbf{q} is the Bloch wave vector difference $\mathbf{q} = \mathbf{k} - \mathbf{k}'$. For the sake of brevity we will employ a shorthand for the Fourier-transformed overlap densities reading

$$\langle \psi_{n,\mathbf{k}} | e^{i(\mathbf{q}+\mathbf{G})\mathbf{r}} | \psi_{n',\mathbf{k}-\mathbf{q}} \rangle = \langle \mathbf{n} | \mathbf{G} | \mathbf{n}' \rangle, \quad (\text{B.2})$$

where \mathbf{n} is a shorthand for $\psi_{n,\mathbf{k}}$.

W is the dynamically screened Coulomb interaction given by [compare Eq. (7.13)]:

$$W_{\mathbf{q}}(\mathbf{G}, \mathbf{G}', \omega) = \frac{4\pi e^2}{|\mathbf{q} + \mathbf{G}| |\mathbf{q} + \mathbf{G}'|} \epsilon_{\mathbf{q}}^{-1}(\mathbf{G}, \mathbf{G}', \omega), \quad (\text{B.3})$$

where ϵ is the symmetric dielectric function, which is defined as

$$\epsilon_{\mathbf{q}}^{-1}(\mathbf{G}, \mathbf{G}', \omega) = \delta_{\mathbf{G}, \mathbf{G}'} + \frac{4\pi e^2}{|\mathbf{q} + \mathbf{G}| |\mathbf{q} + \mathbf{G}'|} \chi_{\mathbf{q}}(\mathbf{G}, \mathbf{G}', \omega). \quad (\text{B.4})$$

In the Random Phase Approximation (RPA), the fully interacting particle polarizability χ is given by the Dyson-like equation Eq. (7.14), and the independent particle polarizability χ_0 is defined as

$$\chi_0^{\mathbf{q}}(\mathbf{G}, \mathbf{G}', \omega') = \frac{1}{\Omega} \sum_{\mathbf{n}''}^{\text{unocc.}} \sum_{\mathbf{n}'''}^{\text{occ.}} \sum_{\mathbf{k}''} 2 \left[\frac{\langle \mathbf{n}''' | -\mathbf{G} | \mathbf{n}'' \rangle \langle \mathbf{n}'' | \mathbf{G}' | \mathbf{n}''' \rangle}{\omega' + \epsilon_{\mathbf{n}'''} - \epsilon_{\mathbf{n}''} + i\eta \text{sgn}(\epsilon_{\mathbf{n}''} - \epsilon_{\mathbf{n}'''})} - \frac{\langle \mathbf{n}'' | -\mathbf{G} | \mathbf{n}''' \rangle \langle \mathbf{n}''' | \mathbf{G}' | \mathbf{n}'' \rangle}{\omega' + \epsilon_{\mathbf{n}''} - \epsilon_{\mathbf{n}'''} + i\eta \text{sgn}(\epsilon_{\mathbf{n}'''} - \epsilon_{\mathbf{n}''})} \right], \quad (\text{B.5})$$

where \mathbf{k}''' and \mathbf{k}'' in Eq. (B.5) satisfy the condition $\mathbf{q} = \mathbf{k}'' - \mathbf{k}'''$.

Approximating the full polarizability by the independent particle polarizability $\chi = \chi_0$, the inverse dielectric matrix simplifies to

$$\epsilon_{\mathbf{q}}^{-1}(\mathbf{G}, \mathbf{G}', \omega) = 1 + \nu \chi_0. \quad (\text{B.6})$$

Putting Eq. (B.6) into Eq. (B.3) results in two terms:

$$W_{\mathbf{q}}(\mathbf{G}, \mathbf{G}', \omega') = \delta_{\mathbf{G}, \mathbf{G}'} \frac{4\pi e^2}{|\mathbf{q} + \mathbf{G}| |\mathbf{q} + \mathbf{G}'|} + \frac{4\pi e^2}{|\mathbf{q} + \mathbf{G}|^2} \chi_0^{\mathbf{q}}(\mathbf{G}, \mathbf{G}', \omega') \frac{4\pi e^2}{|\mathbf{q} + \mathbf{G}'|^2}.$$

Inserting the first term from the above equation into Eq. (B.1) yields the Fock exchange contribution to the one-electron energies, which is usually already included in the HF eigenvalues.

The second term in Eq. (B.7) decays like $\frac{1}{\omega'^2}$ for $\lim_{\omega' \rightarrow \infty}$ when inserted into Eq. (B.1). This term comprises the direct contribution to the MP2 QP energies, and we will concentrate on its evaluation in the following. Putting the second term from Eq. (B.7) into Eq. (B.1) gives

$$\epsilon_{\mathbf{n}}^{\text{dMP2}}(\omega) = \frac{1}{\Omega} \sum_{\mathbf{q}, \mathbf{G}, \mathbf{G}'} \sum_{\mathbf{n}'} \frac{i}{2\pi} \int_{-\infty}^{\infty} d\omega' \frac{\langle \mathbf{n}' | -\mathbf{G}' | \mathbf{n} \rangle}{|\mathbf{q} + \mathbf{G}'|^2} \chi_0^{\mathbf{q}}(\mathbf{G}, \mathbf{G}', \omega') \frac{\langle \mathbf{n} | \mathbf{G} | \mathbf{n}' \rangle}{|\mathbf{q} + \mathbf{G}|^2} \times \frac{16\pi^2 e^4}{\omega - \omega' - \epsilon_{\mathbf{n}'} + i\eta \text{sgn}(\epsilon_{\mathbf{n}'} - \mu)}. \quad (\text{B.7})$$

Using the definition for χ_0 from Eq. (B.5) yields

$$\begin{aligned} \epsilon_{\mathbf{n}}^{\text{dMP2}}(\omega) &= \frac{1}{\Omega^2} \sum_{\mathbf{q}, \mathbf{G}, \mathbf{G}'} \sum_{\mathbf{n}'} \frac{i}{2\pi} \int_{-\infty}^{\infty} d\omega' \frac{4\pi e^2}{|\mathbf{q} + \mathbf{G}|^2} \frac{4\pi e^2}{|\mathbf{q} + \mathbf{G}'|^2} \sum_{\mathbf{n}''}^{\text{unocc.}} \sum_{\mathbf{n}'''}^{\text{occ.}} \sum_{\mathbf{k}'} 2 \\ &\times \left[\frac{\langle \mathbf{n}''' | -\mathbf{G} | \mathbf{n}'' \rangle \langle \mathbf{n}'' | \mathbf{G}' | \mathbf{n}''' \rangle}{\omega' + \epsilon_{\mathbf{n}'''} - \epsilon_{\mathbf{n}''} + i\eta \text{sgn}(\epsilon_{\mathbf{n}''} - \epsilon_{\mathbf{n}'''})} - \frac{\langle \mathbf{n}'' | -\mathbf{G} | \mathbf{n}''' \rangle \langle \mathbf{n}''' | \mathbf{G}' | \mathbf{n}'' \rangle}{\omega' + \epsilon_{\mathbf{n}''} - \epsilon_{\mathbf{n}'''} + i\eta \text{sgn}(\epsilon_{\mathbf{n}'''} - \epsilon_{\mathbf{n}''})} \right] \\ &\times \frac{\langle \mathbf{n} | \mathbf{G} | \mathbf{n}' \rangle \langle \mathbf{n}' | \mathbf{G}' | \mathbf{n} \rangle}{\omega - \omega' - \epsilon_{\mathbf{n}'} + i\eta \text{sgn}(\epsilon_{\mathbf{n}'} - \mu)} \end{aligned}$$

Rearranging the terms and using

$$\langle ij | ab \rangle = \frac{4\pi e^2}{\Omega} \sum_{\mathbf{G}} \frac{\langle \psi_i | -\mathbf{G} | \psi_a \rangle \langle \psi_j | \mathbf{G} | \psi_b \rangle}{|\mathbf{G} + \mathbf{k}_i - \mathbf{k}_a|^2}, \quad (\text{B.8})$$

allows for introducing the two-electron four-orbital integrals.

$$\begin{aligned} \epsilon_{\mathbf{n}}^{\text{dMP2}}(\omega) &= - \sum_{\mathbf{n}'} \frac{i}{2\pi} \int_{-\infty}^{\infty} d\omega' \sum_{\mathbf{n}''}^{\text{unocc.}} \sum_{\mathbf{n}'''}^{\text{occ.}} 2w_{\mathbf{n}''} \left[\frac{\langle \mathbf{n}''' \mathbf{n} | \mathbf{n}'' \mathbf{n}' \rangle \times c.c.}{\omega' + \epsilon_{\mathbf{n}'''} - \epsilon_{\mathbf{n}''} + i\eta \text{sgn}(\epsilon_{\mathbf{n}''} - \epsilon_{\mathbf{n}'''})} \right. \\ &\quad \left. - \frac{\langle \mathbf{n}'' \mathbf{n} | \mathbf{n}''' \mathbf{n}' \rangle \times c.c.}{\omega' + \epsilon_{\mathbf{n}''} - \epsilon_{\mathbf{n}'''} + i\eta \text{sgn}(\epsilon_{\mathbf{n}'''} - \epsilon_{\mathbf{n}''})} \right] \times \frac{1}{\omega' - \omega + \epsilon_{\mathbf{n}'} - i\eta \text{sgn}(\epsilon_{\mathbf{n}'} - \mu)} \end{aligned} \quad (\text{B.9})$$

The integration over ω' can be performed analytically using the residue theorem to yield

$$\begin{aligned} \epsilon_{\mathbf{n}}^{\text{dMP2}}(\omega) &= \frac{-i}{2\pi} \sum_{\mathbf{n}''}^{\text{unocc.}} \sum_{\mathbf{n}'''}^{\text{occ.}} 2 \left[2\pi i \sum_{\mathbf{n}'}^{\text{occ.}} \frac{\langle \mathbf{n}'' \mathbf{n} | \mathbf{n}''' \mathbf{n}' \rangle \times c.c.}{\omega - \epsilon_{\mathbf{n}'} - \epsilon_{\mathbf{n}'''} + \epsilon_{\mathbf{n}''} - 2i\eta} \right. \\ &\quad \left. - 2\pi i \sum_{\mathbf{n}'}^{\text{unocc.}} \frac{\langle \mathbf{n}''' \mathbf{n} | \mathbf{n}'' \mathbf{n}' \rangle \times c.c.}{\epsilon_{\mathbf{n}''} - \epsilon_{\mathbf{n}'''} - \omega + \epsilon_{\mathbf{n}'} - 2i\eta} \right] \end{aligned} \quad (\text{B.10})$$

η is an infinitesimal shift required to distinguish between occupied and unoccupied states, but after the frequency integration it can be dropped. Moreover, we can rearrange the terms to obtain the final expression for the QP energy:

$$\epsilon_{\mathbf{n}}^{\text{dMP2}}(\omega) = \sum_{\mathbf{n}''}^{\text{unocc.}} \sum_{\mathbf{n}'''}^{\text{occ.}} 2 \left[\sum_{\mathbf{n}'}^{\text{unocc.}} \frac{\langle \mathbf{n}''' \mathbf{n} | \mathbf{n}'' \mathbf{n}' \rangle \times c.c.}{\epsilon_{\mathbf{n}'''} + \omega - \epsilon_{\mathbf{n}''} - \epsilon_{\mathbf{n}'}} - \sum_{\mathbf{n}'}^{\text{occ.}} \frac{\langle \mathbf{n}''' \mathbf{n}' | \mathbf{n}'' \mathbf{n} \rangle \times c.c.}{\epsilon_{\mathbf{n}'} + \epsilon_{\mathbf{n}'''} - \omega - \epsilon_{\mathbf{n}''}} \right] \quad (\text{B.11})$$

Clearly Eq. (B.11) is equivalent to the direct terms in Eqs. (7.3) and (7.4).

Appendix C

Implementation of MP2 in VASP

The MP2 correlation energy reads

$$E_C = \sum_{ij}^{\text{occ.}} \sum_{ab}^{\text{unocc.}} \frac{V_{ij}^{ab}(2V_{ij}^{ab} - V_{ij}^{ba})^*}{\epsilon_i + \epsilon_j - \epsilon_a - \epsilon_b}, \quad (\text{C.1})$$

where

$$V_{ij}^{ab} = \langle ij|ab \rangle. \quad (\text{C.2})$$

In the above equation i, j and a, b denote occupied and unoccupied spatial orbitals, respectively. ϵ_x denotes the eigenvalues of the Fock matrix defined in Eq. (4.10). The construction of V_{ij}^{ab} in the framework of the PAW method is outlined in Sec. 8.3. From Sec. 8.3 we find that the electron repulsion integral V_{ij}^{ab} can be written as

$$V_{ij}^{ab} = \sum_{\mathbf{o}} C_{ia}^1(\mathbf{o}) \hat{C}_{jb}^1(\mathbf{o}) + \sum_{\mathbf{G}} \tilde{C}_{ia}(\mathbf{G}) \hat{\tilde{C}}_{jb}(\mathbf{G}), \quad (\text{C.3})$$

where \mathbf{o} is understood to be a shorthand for the indices κ, λ, μ and ν (see Sec. 8.3). \mathbf{G} is a shorthand for the plane wave component \mathbf{G} , as defined in Sec. 8.3. The coefficients $C_{ia}^1, \hat{C}_{jb}^1, \tilde{C}_{ia}$ and $\hat{\tilde{C}}_{jb}$ are implicitly defined through Eqs. (8.31), (8.34), and (8.38).

Our MP2 implementation proceeds in two steps:

1. The coefficients $C_{ia}^1, \hat{C}_{jb}^1, \tilde{C}_{ia}$ and $\hat{\tilde{C}}_{jb}$, are evaluated and stored.

2. The electron repulsion integrals are calculated blockwise from the coefficients. Every block is defined by a combination of occupied orbital indices i and j . Therefore one block at a time needs to be stored in memory and is of the size $N^{\text{unocc.}} \times N^{\text{unocc.}}$. Knowing one block for a given i and j allows for performing the summation over a and b in Eq. (C.1). Subsequently a new block of electron repulsion integrals for the next combination of i and j is evaluated and the nested summation over a and b in Eq. (C.1) is carried out. This is repeated until all possible combinations of i and j are accounted for. Summing over all contributions from the different combinations of i and j yields the MP2 correlation energy.

The above steps are highly parallelizable. In step (1) all occupied orbitals i are distributed to all nodes. For a set of unoccupied orbitals $\{a\}$, which is different on every node, the coefficients $C_{i\{a\}}^1$, $\hat{C}_{i\{a\}}^1$, $\tilde{C}_{i\{a\}}$ and $\hat{\tilde{C}}_{i\{a\}}$ are evaluated and stored locally. From step (1) to step (2) a redistribution of the coefficients is carried out. The coefficients are brought into a block-cyclic matrix distribution that is well suited for highly efficient parallelized matrix-matrix multiplication routines. The columns of the distributed coefficient matrices correspond to the indices \mathbf{G} and \mathbf{o} , respectively. The rows of the distributed coefficient matrices corresponds to the index of the unoccupied orbitals a . In total there are $4N^{\text{occ.}}$ block-cyclically distributed coefficient matrices ($C_i^1(a, \mathbf{o})$, $\hat{C}_i^1(a, \mathbf{o})$, $\tilde{C}_i(a, \mathbf{G})$ and $\hat{\tilde{C}}_i(a, \mathbf{G})$). This allows for a blockwise construction of the electron repulsion integrals using highly efficient parallel matrix-matrix multiplication routines (*ScaLAPACK* libraries). Since the construction of the electron repulsion integrals scales as $\mathcal{O}(N^5)$, where N is a measure of the system size, this step is the computational bottle neck of our implementation.

Appendix D

Implementation of RPA+SOSEX in VASP

The coupled-cluster double amplitude equations in the random phase approximation read

$$0 = \langle ij|ab\rangle + t_{ij}^{ab}(\epsilon_a + \epsilon_b - \epsilon_i - \epsilon_j) \\ + \langle ic|ak\rangle t_{kj}^{cb} + t_{ik}^{ac} \langle cj|kb\rangle + t_{ik}^{ac} \langle cd|kl\rangle t_{lj}^{db}. \quad (\text{D.1})$$

The solution of the above equations is outlined in Sec. 5.7 and scales as $\mathcal{O}(N^6)$, where N is a measure of the system size. However, it is possible to reduce the computational effort for calculating the amplitudes and the RPA+SOSEX energy to scale as $\mathcal{O}(N^5)$ only. This is achieved by rearranging the nested summations in the construction of the electron repulsion integrals and the amplitude equations. For this purpose we define intermediate quantities that read as

$$\chi_{ia}^1(\mathbf{o}) = \sum_{kc} t_{ik}^{ac} C_{kc}^1(\mathbf{o}), \quad (\text{D.2})$$

$$\hat{\chi}_{ia}^1(\mathbf{o}) = \sum_{kc} t_{ik}^{ac} \hat{C}_{kc}^1(\mathbf{o}), \quad (\text{D.3})$$

$$\tilde{\chi}_{ia}(\mathbf{G}) = \sum_{kc} t_{ik}^{ac} \tilde{C}_{kc}(\mathbf{G}), \text{ and} \quad (\text{D.4})$$

$$\hat{\chi}_{ia}(\mathbf{G}) = \sum_{kc} t_{ik}^{ac} \hat{C}_{kc}(\mathbf{G}). \quad (\text{D.5})$$

$$(\text{D.6})$$

The coefficients C_{kc}^1 , \hat{C}_{kc}^1 , \tilde{C}_{kc} and $\hat{\tilde{C}}_{kc}$ have been introduced in Eq. (C.3). Employing the above definitions of the intermediate quantities allows for rewriting Eq. (D.1) into an equation that scales only as N^5 :

$$0 = t_{ij}^{ab}(\epsilon_a + \epsilon_b - \epsilon_i - \epsilon_j) + \sum_{\mathbf{o}} [C_{ia}^1(\mathbf{o}) + \chi_{ia}^1(\mathbf{o})] \left[(\hat{C}_{jb}^1(\mathbf{o}) + \hat{\chi}_{jb}^1(\mathbf{o})) \right] \\ + \sum_{\mathbf{G}} \left[\tilde{C}_{ia}(\mathbf{G}) + \tilde{\chi}_{ia}(\mathbf{G}) \right] \left[\hat{\tilde{C}}_{jb}(\mathbf{G}) + \hat{\tilde{\chi}}_{jb}(\mathbf{G}) \right] \quad (\text{D.7})$$

Because of the simplicity of Eq. (D.7) an important technical advantage arises. In contrast to a full CCSD algorithm, it suffices to store a single set of amplitudes, which greatly reduces the memory requirements.

The distribution of the coefficients C_{kc}^1 , \hat{C}_{kc}^1 , \tilde{C}_{kc} and $\hat{\tilde{C}}_{kc}$, as well as intermediate quantities $\chi_{ia}^1(\mathbf{o})$, $\hat{\chi}_{ia}^1(\mathbf{o})$, $\tilde{\chi}_{ia}(\mathbf{G})$, and $\hat{\tilde{\chi}}_{ia}(\mathbf{G})$ is done analogue to the the procedure outlined in Appendix C. Hence, the MP2 as well as RPA+SOSEX implementation are based on highly efficient matrix-matrix multiplication routines.

Bibliography

- [1] P. Hohenberg, and W. Kohn, Phys. Rev. **136**, B864 (1964).
- [2] W. Kohn, and L. J. Sham, Phys. Rev. **140**, A1133 (1965).
- [3] D. M. Ceperley, and B. J. Alder, Phys. Rev. Lett. **45**, 566 (1980).
- [4] J. P. Perdew, and W. Yue, Phys. Rev. B **33**, 8800 (1986).
- [5] J. P. Perdew, K. Burke, and M. Ernzerhof, Phys. Rev. Lett. **77**, 3865 (1996).
- [6] D. R. Hartree, Proc. Cambridge Philos. Soc. **24**, 89 (1928).
- [7] V. Fock, Z. Phys. **61**, 55 (1930).
- [8] J. C. Slater, Phys. Rev. **35**, 210 (1930).
- [9] A. Szabo, and N. S. Ostlund, Modern quantum chemistry, Dover, Mineola, New York (1996).
- [10] T. Kato, Comm. Pure Appl. Math. **10**, 151 (1957).
- [11] Chr. Møller, and M. S. Plesset, Phys. Rev. **46**, 618 (1934).
- [12] R. D. Mattuck, A Guide to Feynman Diagrams in the Many-Body Problem, Dover, Mineola, New York (1992).
- [13] F. Coester, Nucl. Phys. **1**, 421 (1958).
- [14] F. Coester and H. Kümmel, Nucl. Phys. **17**, 477 (1960).
- [15] J. Čížek, J. Phys. Chem. **45**, 4256 (1966).
- [16] R. J. Bartlett and M. Musial, Rev. Mod. Phys. **79**, 291 (2007).

-
- [17] G. D. Purvis and R. J. Bartlett, *J. Chem. Phys.* **76**, 1910 (1982).
- [18] S. Hirata, I. Grabowski, M. Tobita, and R. J. Bartlett, *Chem. Phys. Lett.* **345**, 475 (2001).
- [19] S. Hirata, R. Podeszwa, M. Tobita, and R. J. Bartlett, *J. Chem. Phys.* **120**, 2581 (2004).
- [20] S. Hirata, *J. Phys. Chem. A* **107**, 9887 (2003).
- [21] P. Piecuch, S. A. Kucharski, K. Kowalski, and M. Musial, *Comp. Phys. Comm.* **149**, 71 (2002).
- [22] D. L. Freeman, *J. Phys. C: Solid State Phys.* **16**, 711 (1983).
- [23] P. Nozières, and D. Pines, *Phys. Rev.* **111**, 442 (1958).
- [24] J. Harl, L. Schimka and G. Kresse, *Phys. Rev. B* **81**, 115126 (2010).
- [25] L. Hedin, *Phys. Rev.* **139**, A796 (1965).
- [26] M. S. Hybertsen, and S. G. Louie, *Phys. Rev. B* **34**, 5390 (1986).
- [27] M. van Schilfgaarde, T. Kotani, and S. Faleev, *Phys. Rev. Lett.* **96**, 226402 (2006).
- [28] F. Furche, *Phys. Rev. B* **64**, 195120 (2001).
- [29] Y. M. Niquet, M. Fuchs, and X. Gonze, *Phys. Rev. A* **68**, 032507 (2003).
- [30] N. E. Dahlen, R. van Leeuwen, and U. von Barth, *Phys. Rev. A* **73**, 012511 (2006).
- [31] O. Gunnarsson, and B. I. Lundqvist, *Phys. Rev. B* **13**, 4274 (1976).
- [32] D. C. Langreth, and J. C. Perdew, *Phys. Rev. B* **15**, 2884 (1977).
- [33] D. L. Freeman, *Phys. Rev. B* **15**, 5512 (1977).
- [34] G. E. Scuseria, T. M. Henderson, and D. C. Sorensen, *J. Chem. Phys.* **129**, 231101 (2008).
- [35] J. Cizek, *Adv. Chem. Phys.* **14**, 35 (1969).

-
- [36] J. Harl, The linear response function in density functional theory: Optical spectra and improved description of the electron correlation, PhD thesis, Universität Wien, Austria (2008).
- [37] Huy-Viet Nguyen, Efficient calculation of RPA correlation energy in the Adiabatic Connection Fluctuation-Dissipation Theory, PhD Thesis, International School for Advanced Studies (SISSA), Trieste, Italy (2008).
- [38] H. B. Callen, and T. A. Welton, *Phys. Rev.* **83**, 34 (1951).
- [39] D. C. Langreth, and J. C. Perdew, *Solid State Commun.* **17**, 1425 (1975).
- [40] E. K. Gross, and W. Kohn, *Phys. Rev. Lett.* **55**, 2850 (1985).
- [41] M. Shishkin and G. Kresse, *Phys. Rev. B* **74**, 035101 (2006).
- [42] F. Furche, *J. Chem. Phys.* **114**, 5982 (2001).
- [43] M. E. Casida, Time-dependent density functional response theory of molecular systems: Theory, computational methods, and functionals, , in *Recent Developments and Application of Modern Density Functional Theory*, edited by J. M. Seminario, pp. 391-439, Amsterdam (1996).
- [44] F. Furche, *J. Chem. Phys.* **129**, 114105 (2008).
- [45] J. Harl, and G. Kresse, *Phys. Rev. B* **77**, 045136 (2008).
- [46] J. Harl, and G. Kresse, *Phys. Rev. Lett.* **103**, 056401 (2009).
- [47] H. J. Monkhorst, and J. Oddershede, *Phys. Rev. Lett.* **30**, 797 (1973).
- [48] P. Romaniello, S. Guyot, and L. Reining, *J. Chem. Phys.* **131**, 154111 (2009).
- [49] P.-O. Löwdin, *Phys. Rev.* **97**, 1474 (1955).
- [50] F. Aquilante, T. K. Todorova, L. Gagliardi, T. B. Pedersen, and B. O. Roos, *J. Chem. Phys.* **131**, 034113 (2009).
- [51] C. Friedrich, and A. Schindlmayr, *Many-Body Perturbation Theory: The GW Approximation*, published in *Computational Nanoscience: Do*

- It Yourself!, J. Grotendorst, S. Blügel, D. Marx (Eds.), John von Neumann Institute for Computing, Jülich, NIC Series, Vol. 31, pp. 335-355 (2006).
- [52] S. Suhai, Phys. Rev. B **27**, 3506 (1983).
- [53] M. S. Hybertsen, and S. G. Louie, Phys. Rev. B **34**, 5390 (1986).
- [54] J. Schirmer, L. S. Cederbaum, and O. Walter, Phys. Rev. A **28**, 1237 (1982).
- [55] P. E. Blöchl, Phys. Rev. B **50**, 17953 (1994).
- [56] D. Vanderbilt, Phys. Rev. B **41**, 7892 (1990).
- [57] G. Kresse, and D. Joubert, Phys. Rev. B **59**, 1758 (1999).
- [58] J. Paier, R. Hirschl, M. Marsman, and G. Kresse, J. Chem. Phys. **122**, 234102 (2005).
- [59] M. Gajdoš, K. Hummer, G. Kresse, J. Furthmüller, and F. Bechstedt, Phys. Rev. B **73**, 045112 (2006).
- [60] J. D. Watts, J. Gauss, and R. J. Bartlett, J. Chem. Phys. **98**, 8718 (1995).
- [61] P. Pulay, and S. Saebø, Theoret. Chim. Acta **69**, 357 (1986).
- [62] S. Saebø and P. Pulay, Annu. Rev. Phys. Chem. **44**, 213 (1993).
- [63] M. Schütz, G. Hetzer, and H.-J. Werner, J. Chem. Phys. **111**, 5691 (1999).
- [64] J. Subotnik, and M. Head-Gordon, J. Chem. Phys. **123**, 064108 (2005).
- [65] G. Stollhoff, and P. Fulde, Z. Phys. B **26**, 251 (1977).
- [66] G. Stollhof, and P. Fulde, J. Chem. Phys. **73**, 4548 (1980).
- [67] G. Stollhof, J. Chem. Phys. **105**, 227 (1996).
- [68] H. Stoll, Phys. Rev. B **46**, 6700 (1992).

- [69] H. Stoll, Chem. Phys. Lett. **191**, 548 (1992).
- [70] H. Stoll, J. Chem. Phys. **97**, 8449 (1992).
- [71] P. Y. Ayala, and G. E. Scuseria, J. Chem. Phys. **110**, 3660 (1999).
- [72] G. E. Scuseria, and P. Y. Ayala, J. Chem. Phys. **111**, 8330 (1999).
- [73] M. Schütz, and H.-J. Werner, Chem. Phys. Lett. **318**, 370 (2000).
- [74] F. Claeysens, J. N. Harvey, F. R. Manby, R. A. Mata, A. J. Mulholland, K. E. Ranaghan, M. Schütz, S. Thiel, W. Thiel, and H.-J. Werner, Angew. Chem. **118**, 7010 (2006).
- [75] B. Paulus, Phys. Rep. **428**, 1 (2006).
- [76] C. Pisani, M. Busso, G. Capecchi, S. Casassa, R. Dovesi, L. Maschio, C. Zicovich-Wilson, and M. Schütz, J. Chem. Phys. **122**, 094113 (2005).
- [77] C. Pisani, L. Maschio, S. Casassa, M. Halo, M. Schütz, and D. Usvyat, J. Comput. Chem. **29**, 2113 (2008).
- [78] S. Casassa, M. Halo, L. Maschio, C. Roetti, and C. Pisani, Theor. Chem. Acc. **117**, 781 (2007).
- [79] P. Y. Ayala, K. N. Kudin, and G. E. Scuseria, J. Chem. Phys. **115**, 9698 (2001).
- [80] F. R. Manby, D. Alfè, and M. J. Gillan, Phys. Chem. Chem. Phys. **8**, 5178 (2006).
- [81] M. J. Gillan, D. Alfè, S. de Gironcoli, and F. R. Manby, J. Comput. Chem. **29**, 2098 (2008).
- [82] F. R. Manby (Private communication).
- [83] J.-Q. Sun, and R. J. Bartlett, J. Chem. Phys. **104**, 8553 (1996).
- [84] M. J. Frisch, G. W. Trucks, H. B. Schlegel, *et al.*, GAUSSIAN 03, Revision B.02, Gaussian, Inc., Wallingford, CT (2004).
- [85] S. Massida, M. Posternak, and A. Baldereschi, Phys. Rev. B **48**, 5058 (1993).

- [86] J. Spencer, and A. Alavi, *Phys. Rev. B* **77**, 193110 (2008).
- [87] M. Marsman, A. Grüneis, J. Paier, and G. Kresse, *J. Chem. Phys.* **130**, 184103 (2009).
- [88] V. N. Staroverov, G. E. Scuseria, J. Tao, and J. P. Perdew, *Phys. Rev. B* **69**, 075102 (2004).
- [89] O. Madelung, *Semiconductors: Data Handbook*, 3rd ed. Springer, Berlin (2004).
- [90] A. Trampert, O. Brandt, K. H. Ploog, in *Crystal Structure of Group III Nitrides*, edited by J.I. Pankove and T.D. Moustakas, *Semiconductors and Semimetals Vol. 50*, San Diego (1998).
- [91] S. M. Sze, *Physics of Semiconductor Devices* Wiley Interscience, New York (1981).
- [92] R. W. G. Wyckoff, *Crystal Structures* Interscience New York (1963).
- [93] The experimental crystal structure of sodium is body-centered-cubic (bcc). However, for the present purpose we have employed the face-centered-cubic structure, because it is more densely packed and it does not affect the divergence of MP2 for metallic systems. The lattice constant of the face-centered-cubic sodium was chosen such that the volume agrees with the volume of the bcc crystal.
- [94] <http://www.msg.chem.iastate.edu/GAMESS/GAMESS.html>
- [95] M. W. Schmidt, K. K. Baldrige, J. A. Boatz, S. T. Elbert, M. S. Gordon, J. H. Jensen, S. Koseki, N. Matsunaga, K. A. Nguyen, S. J. Su, T. L. Windus, M. Dupuis, J. A. Montgomery, *J. Comput. Chem.* **14**, 1347 (1993).
- [96] M. S. Gordon, M. W. Schmidt, Chapter 41, pp 1167-1189, in “Theory and Applications of Computational Chemistry, the first forty years” (2005).
- [97] L. Schimka, J. Harl, and G. Kresse, to be published.

- [98] J. Paier, M. Marsman, K. Hummer, G. Kresse, I. C. Gerber, and J. G. Ángyán, *J. Chem. Phys.* **124**, 154709 (2006).
- [99] PBE calculations for BN, BP, BAs, and LiH have been carried out using VASP with the same cutoffs and settings as for the HF calculations.
- [100] RPA calculations for BN, BP, BAs, and LiH have been carried out using VASP with the same cutoffs and settings as for the MP2 calculations.
- [101] A. Grüneis, M. Marsman, J. Harl, L. Schimka, and G. Kresse, *J. Chem. Phys.* **131**, 154115 (2009).
- [102] A. Shukla, M. Dolg, P. Fulde, and H. Stoll, *Phys. Rev. B* **60**, 5211 (1999).
- [103] T. Helgaker, T. A. Ruden, P. Jørgensen, J. Olsen, and W. Klopper, *J. Phys. Org. Chem.* **17**, 913, (2004).
- [104] M. Shishkin, and G. Kresse, *Phys. Rev. B* **75**, 235102 (2007).
- [105] M. Gell-Mann, and K. A. Brueckner, *Phys. Rev.* **106**, 364 (1957).
- [106] P. Mori-Sánchez, A. Cohen, and W. Yang, submitted.
- [107] DALTON, a molecular electronic structure program, Release 2.0 (2005), see <http://daltonprogram.org/>
- [108] D. Feller, *J. Comp. Chem.* **17**, 1571 (1996).
- [109] S. J. Chakravorty, S. R. Gwaltney, E. R. Davidsion, F. A. Parpia, and C. Froese Fischer, *Phys. Rev. A* **47**, 3649 (1993).
- [110] H. Jiang, and E. Engel, *J. Chem. Phys.* **127**, 184108 (2007).
- [111] S. Kurth, and J. P. Perdew, *Phys. Rev. B* **59**, 10461 (1999).
- [112] P. García-González, and R.W. Godby, *Phys. Rev. B* **63**, 075112 (2001).
- [113] B. Holm, and U. von Barth, *Phys. Rev. B* **57**, 2108 (1998).
- [114] K. P. Huber, and G. Herzberg, *Constants of Diatomic Molecules, Vol. IV of Molecular Spectra and Molecular Structure* Van Nostrand Reinhold, New York (1979).

-
- [115] C. Adamo, M. Ernzerhof, and G. E. Scuseria, *J. Chem. Phys.* **112**, 2643 (2000).
- [116] L. A. Curtiss, K. Raghavachari, and J. A. Pople, *J. Chem. Phys.* **98**, 1293 (1993).
- [117] J. F. Oglivie and F. Y. H. Wang, *J. Mol. Struct.* **273**, 277 (1992).
- [118] L. Schimka, J. Harl and G. Kresse, to be published.
- [119] K. L. Bak, P. Jorgensen, J. Olsen, T. Helgaker, J. Gauss, *Chem. Phys. Lett.* **317**, 116 (2000).
- [120] J. Paier, B. G. Janesko, T. M. Henderson, G. E. Scuseria, A. Grüneis and G. Kresse, *J. Chem. Phys.* **133**, 179902 (2010).
- [121] T. Shiozaki and S. Hirata, *J. Chem. Phys.* **132**, 151101 (2010).
- [122] P. Neogrady, M. Pitonak, and M. Urban, *Molecular Physics* **103**, 2141 (2005).
- [123] A. G. Taube and R. J. Bartlett, *Collection of Czechoslovak Chemical Communications* **70**, 837 (2005).
- [124] A. G. Taube and R. J. Bartlett, *J. Chem. Phys.* **128**, 164101 (2008).
- [125] S. J. Nolan, M. J. Gillan, D. Alfe, N. L. Allan, and F. R. Manby *Phys. Rev. B* **80**, 165109 (2009).
- [126] Y.-y. Ohnishi and S. Hirata, *J. Chem. Phys.* **133**, 034106 (2010).
- [127] S. Albrecht, and L. Reining, and R. Del Sole, and G. Onida, *Phys. Rev. Lett.* **80**, 4510 (1998).

Curriculum vitae

Mag.rer.nat. Andreas Grüneis
Faculty of Physics
University of Vienna
Sensengasse 8/12
A-1090 Wien

Phone: +43 1 4277 51410
EMail: a0255939@unet.univie.ac.at

Date and place of birth: 11.09.1983, Wels
Citizenship: Austria

Education

- **University of Vienna** Vienna, Austria
PhD student Sept. 2007 - Jan. 2011
– Thesis: “Diagrammatic techniques for extended systems: MP2 and CCSD”
Advisor: Prof. Georg Kresse
- **University of Vienna** Vienna, Austria
Mag.rer.nat. (graduation with distinction) Sept. 2002 - Jul. 2007
– Thesis: “Ab-initio studies of lead chalcogenides”
Advisor: Prof. Georg Kresse

Scholarships and Awards

- **PCCP graduate student poster award**
50th Sanibel Symposium February 2010
- **Erasmus Scholarship** Universitat Autònoma de Barcelona, Spain
European Union Feb. 2006 - Jun. 2006

Publications List

1. Joachim Paier, Benjamin G. Janesko, Thomas M. Henderson, Gustavo E. Scuseria, Andreas Grüneis, and Georg Kresse
“Erratum: Hybrid functionals including random phase approximation correlation and second-order screened exchange”
J. Chem. Phys. **132**, 094103 (2010).
2. Laurids Schimka, Judith Harl, Alessandro Stroppa, Andreas Grüneis, Martijn Marsman, Florian Mittendorfer, and Georg Kresse
“Accurate surface and adsorption energies from many-body perturbation theory”
Nature Materials **9**, 741 (2010).
3. Andreas Grüneis, Martijn Marsman, and Georg Kresse
“Second-order Møller-Plesset perturbation theory applied to extended systems. II. Structural and energetic properties”
J. Chem. Phys. **133**, 074107 (2010).
4. Joachim Paier, Benjamin G. Janesko, Thomas M. Henderson, Gustavo E. Scuseria, Andreas Grüneis, and Georg Kresse
“Hybrid functionals including random phase approximation correlation and second-order screened exchange”
J. Chem. Phys. **132**, 094103 (2010).
5. Andreas Grüneis, Martijn Marsman, Judith Harl, Laurids Schimka, and Georg Kresse
“Making the random phase approximation to electronic correlation accurate”
J. Chem. Phys. **131**, 154115 (2009).
6. Martijn Marsman, Andreas Grüneis, Joachim Paier, and Georg Kresse
“Second-order Møller-Plesset perturbation theory applied to extended

- systems. I. Within the projector-augmented-wave formalism using a plane wave basis set”
J. Chem. Phys. **130**, 184103 (2009).
7. Andreas Grüneis, Kerstin Hummer, Martijn Marsman, and Georg Kresse
“Nonlinear behavior of the band gap of $\text{Pb}_{1-x}\text{Eu}_x\text{Se}$ ($0 < x < 1$) from first principles”
Phys. Rev. B **78**, 165103 (2008).
 8. Kerstin Hummer, Andreas Grüneis, and Georg Kresse
“Structural and electronic properties of lead chalcogenides from first principles”
Phys. Rev. B **75**, 195211 (2007).
 9. Andreas Grüneis, Maria J. Esplandiu, Daniel Garcia-Sanchez, and Adrian Bachtold
“Detecting individual electrons using a carbon nanotube field-effect transistor”
Nano Letters **7**, 3766 (2007).

Talks

1. **ViCoM Workshop** Stadtschlaining, Austria
28-29 October 2010
 - MP2 and CCSD applied to extended systems
2. **Ψ_k Conference 2010** Berlin, Germany
12-16 September 2010
 - 2nd-order Møller-Plesset perturbation theory and coupled-cluster singles doubles applied to extended systems
3. **Multidisciplinary Workshop on RPA** Paris, France
25-29 January 2010
 - Wave function based correlation in solids: RPA and beyond
4. **CESTC** Dobogókő, Hungary
25-28 September 2009
 - Random phase approximation plus second-order screened exchange applied to extended systems.

Posters

1. **50th Sanibel Symposium** St. Simons Island, GA, USA
24 February - 2 March, 2010
 - Improving upon the random phase approximation
2. **13th ICQC** Helsinki, Finland
22-27 June, 2009
 - Random phase approximation plus second-order screened exchange
3. **DPG Spring meeting** Dresden, Germany
22-27 March, 2009
 - 2nd-order Møller-Plesset perturbation theory applied to extended system.
4. **CECAM Workshop** Lyon, France
26-29 May, 2008
 - 2nd-order Møller-Plesset perturbation theory applied to extended system.